The Pennsylvania State University
The Graduate School

MODELING, REAL-TIME DEGRADATION IDENTIFICATION, AND REMEDIATION OF PB-ACID BATTERIES

A Dissertation in
Mechanical and Nuclear Engineering
by
Ying Shi

Submitted in Partial Fulfillment
of the Requirements
for the Degree of

Doctor of Philosophy

December 2013

The dissertation of Ying Shi was reviewed and approved* by the following:

Christopher D. Rahn
Professor of Mechanical Engineering
Dissertation Advisor, Chair of Committee

Chao-Yang Wang
William E. Diefenderfer Chair of Mechanical Engineering

Hosam K. Fathy
Assistant Professor of Mechanical Engineering

Jeffrey S. Mayer
Associate Professor of Electrical Engineering

Karen A. Thole
Department Head of Mechanical and Nuclear Engineering
Professor of Mechanical Engineering

*Signatures are on file in the Graduate School.

Abstract

Valve Regulated Lead-Acid (VRLA) batteries are cheap and mature technology, favorable candidates for micro-hybrid vehicles and stationary applications. Large-scale battery packs, instead of individual cells, are implemented in those applications; therefore sophisticated battery management system (BMS) becomes necessary and crucial to ensure the longevity and efficient utilization of battery packs. Such a BMS must have several key elements: a simple but accurate system model that captures battery performance and aging processes, sensor measurements that gather information to help the controller monitor battery health and identify major aging mechanisms, and an advanced controller that estimates state of charge (SOC) and state of health (SOH) of cells and optimizes their usage accordingly.

This research first reviews six modeling techniques that are suitable for developing electrochemistry-based system models of batteries. Fundamental battery models, consisting of nonlinear coupled partial differential equations, are often difficult to discretize and reduce in order so that they can be used by systems engineers for design, estimation, prediction, and management. In this work, six methods are used to discretize a benchmark electrolyte diffusion problem and their time and frequency response accuracy is determined as a function of discretization order. The Analytical Method (AM), Integral Method Approximation (IMA), Padé Approximation Method (PAM), Finite Element Method (FEM), Finite Difference Method (FDM) and Ritz Method (RM) are formulated for the benchmark problem and convergence speed and accuracy calculated. The PAM is the most efficient, producing 99.5% accurate results with only a 3rd order approximation. IMA, Ritz, AM, FEM, and FDM required 4, 6, 9, 14, and 27th order approximations, respectively, to achieve the same error. If both modeling complexity and efficiency are considered, Ritz method is the best candidate.

Secondly, this research presents a nondestructive experiment method to perform real-time aging diagnosis of lead-acid batteries. VTLA batteries can degrade due to a variety of mechanisms, including corrosion, hard sulfation, water loss, shedding, and

active mass degradation. VRLA batteries are designed to minimize these effects as much as possible but the operating environment, cell-to-cell and battery-to-battery manufacturing variations, and use can cause different degradation mechanisms to dominate capacity loss and/or impedance rise. With accurate State of Health monitoring, cell usage can be adjusted by the battery management system (BMS) to optimize the performance and life of the energy storage system. The BMS must be able to determine in real time the predominant degradation mechanism for each cell and adjust use accordingly. In this work, new and dead VRLA batteries are tested with constant, sinusoidal, and pulse charge/discharge current inputs while measuring the cell voltage and pressure to determine the cause of death of the cells. As expected, the new cells have fairly uniform performance with limited signs of degradation. The cells in the dead battery, however, have widely ranging performance, especially at the end of discharge and charge. Analysis of the charge/discharge data indicate that three cells died of water loss and a fourth cell died of sulfation. The remaining two cells were fairly healthy but will accompany their dead companions to the recycling center nonetheless. While the full charge/discharge data provided useful forensic pathology data, EIS and pulse charge/discharge data varied with aging mechanisms and only provided supplementary pathology information.

Following the real-time diagnosis work, a charging control scheme is proposed that removes hard sulfation in lead-acid cells without introducing excessive gassing. In a battery string, the cell with the lowest capacity dominants that of the entire string. If that cell's capacity can be recovered, the capacity of the whole string will increase. However, not all aging mechanisms in lead-acid batteries are reversible but hard sulfation is. Often, removal of one degradation mechanism might worsen another. In this study, it appears that one cell of a 6-cell string died from sulfation and another three from dehydration. The battery capacity is mainly dictated by the sulfated cell. A desulfation charging control scheme with pressure feedback is designed to break up hard sulfate and recover capacity while minimizing water loss by using low current charging. The capacity of the cell is recovered by 41% with minimal water loss, demonstrating the effectiveness of the desulfation charge controller.

The experiments reveal the great potential of charge strategies with pressure control. To make this health-cautious charge more cost-effective and easy to implement, a nonlinear system model is developed, aiming to eliminate the pressure transducers by covering gassing side reactions in the model. The system model is fifth-order with parameters and states that are based on the electrochemical processes and battery properties. It preserves the majority of the underlying complex mathematical model but enjoys the beauty of state space form, which eases future controllers and estimators design. The model is validated with testing data and shows good match in battery voltage and pressure responses. It also returns the internal states such as acid concentration, solid-phase potentials, and transfer current densities. Those states can be used for control in the future.

Powered by the nonlinear system model a health-cautious charge strategy, constant-current constant-overpotential (CC-Cη), is presented. In a lead-acid cell, the overpotentials directly control the oxygen and hydrogen generation. Compare to conventional constant-current constant-voltage charge protocols, CC-Cη charge protocols produce less gas and increase the charge efficiency. Controlling η on the positive electrode directly suppresses the oxygen generation and also affects η on the negative electrode, slowing down hydrogen production, vice versa. It has also been shown that a SOC estimator based on the internal acid concentration level has better performance than one that is based on current counting in the overcharge stage, where SOC curve is high nonlinear and part of the input current goes to side reactions.

Table of Contents

List of Figures

List of Tables

List of Symbols

Variables

η	overpotential	V
ϕ_e	electrolyte phase potential	V
ϕ_s	solid phase potential	V
c	acid concentration	mol/cm^3
c_e	gas concentration in electrolyte phase	mol/cm^3
c_g	gas concentration in gas phase	mol/cm^3
EUC	electrode utilization coefficient	-
I	applied current	A
i_e	transfer current density of reactions	A/cm^3
Δp	pressure increase	psi
p	pressure	psi
Q	heat generated from the cell	J
SOC	state of charge	-
ΔT	temperature increase	K
T	temperature	K
t	time	s

V_{cell}	cell voltage	V

Parameters

ε_e	porosity of electrolyte phase	-
ε_g	porosity of gas	-
κ_{eff}^D	effective diffusional conductivity	S/cm
κ_{eff}	ionic conductivity of electrolyte	S/cm
ρ	lumped volume fraction	cm
σ_{eff}	conductivity of solid active material	S/cm
A	cross-section area	cm^2
a_e	specific surface area of reactions	cm^2/cm^3
a_{dl}	specific surface area of double layer effect	cm^2/cm^3
C_v	volumetric heat capacity of air	$J/(mol\ K)$
C_{dl}	specific capacity of double layer effect	F/cm^2
$D_{e,eff}$	diffusion coefficient of electrolyte phase	cm^2/S
$D_{g,eff}$	diffusion coefficient of gas phase	cm^2/S
E^o	standard electrode potential	V
F	Faraday's constant	C/mol
H'	Henry constant	-
J_{eg}	source term for gas concentration	$mol/(cm^3\ s)$
k	interfacial mass transfer coefficient at the electrolyte/gas interface	cm/s
L	length of electrodes and separator	cm
R	universal gas constant	$J/(mol\ K)$
R_c	contact resistant	Ω
S_e	source term for acid concentration	$mol/(cm^3\ s)$

S_{es}	source term for electrolyte/solid phase potential	$mol/(cm^3\ s)$
t_+^0	transfer number	-
U_j	equilibrium potentials of reactions	V
v	cell volume	cm^3

Superscripts

H	proton
H_2	hydrogen
O_2	oxygen

Acknowledgments

I would like to thank my adviser, Dr. Christopher Rahn, for his support, guidance, and encouragement throughout these years. He is the best adviser I could ever dream. He is always patient and positive, never telling you the work is worse than "good job"; and he is also brilliant and inspiring, returning ten possible solutions when I ran into bottlenecks. I also want to thank my committees, Dr. Fathy, Dr. Wang, and Dr. Mayer for their insightful discussions and suggestions.

Besides the best adviser, I have enjoyed working with a group of awesome people. I would not have finished my dissertation without them. Thank you, Chris Ferone, for making the battery test station from scratch. It was such an elegant piece that generated those nice data for our papers (it can even call my name and tell me the test is done!). Also, thank you for "living" in the lab to have the test run and for revising my draft and helping me improve my writing. Outside the work, I enjoyed our discussions on cultures, religions, politics, food, and, of course, shopping styles. I miss watching you and Nick teasing each other. Chris Melville, it was a great pleasure to work with you and you amazed me by getting on speed so quickly. I will also remember your fauxhawk hairstyle. Jun Gou and Yancheng Zhang, thank you for your excellent patience to teach me and help me understand the basics of electrochemistry and batteries. Lei, thank you for all the help and discussions on the testing. Lloyd Scarborough, thank you for everything you have done to help me and Chris set up the experiments and to keep the lab running in a clean and productive environment. You are the most organized person I have ever seen. Also, I'd like thank all of my fellow labmates for the 5-yr joyful memories they have given me: Deepak Trivedi, Amir Lofti, Hareesh Kommepalli, Kiron Mateti, Zheqian Zhang, Thomas Levard, Paul Diglio, Githin Parsad, Bin Zhu, Zheng Shen, Nick Kurczewski, Michael Robinson, Chinmay Rao, Varma Gottimukkala, Rory Byrne-Dugan, Kentaro Miura, Dan Aglione, and Xiaokun Ma.

The 5-yr at Penn State is a long journey for me. Being more than 7,300 miles away from home, I would have collapsed and given up in the halfway if not my friends in State College, in the United States and back in China: Miaoyin Wang, Keqin Cao, Dongmei Yan, Qinlin Shen, Yi Zhang, Wenjiao Zhao, Tingting Lu, Jue Li, Jun Yao, Xue Bai, Kai

He, Guixi Zhou, Yin Guo, Yan Ji, Wei Zhao, Yicheng Wen, Ying Zhang, Chao Feng, Jing Zhou, and Wei Lu. I cannot thank you enough for supporting me on this journey. Thank you for helping me settle down when I first arrived here, for introducing me to the new community when I am a stranger, for comforting me and cheering me up when I was upset and low, for surprising me with a birthday greeting, for accompanying me to explore the country, for lighting up the sky for me and making the journey more fun if not less bumpy.

Finally, I would like to thank my parents, who always believe in me and support my every decision, and who sacrifice daughter's company to let me chase my dream. You have not enjoyed the benefit of having a child that a lot of people of their generation are enjoying, being taken care of when they need and having new grandchildren to cradle. Thank you for your unconditional and unselfish love. And Xin, for what you are, for your love and support in every step. You are the light of my life.

Dedication

To my beloved grandparents, especially my grandpas. I hope both of you would be proud of me.

Chapter 1

Introduction

Large-scale battery packs are a crucial and costly component in the blooming "green" technologies, especially in hybrid vehicles/locomotives and renewable energy applications. The state-of-art designs of battery packs are often greatly oversized and underutilized for safety and reliability reasons, which is partially responsible for packs' high cost. Downsizing battery packs calls for more sophisticated battery management systems (BMS) that can push the cells to operate in a wider SOC range and under higher rate load without the risk of premature degradation or thermal runaway. With an advanced BMS, manufacturers and users can also save cost in maintenance and warranty.

For system/control engineers, an intelligent battery management system (BMS) design will have a very accurate yet computationally cheap baseline model, as fewer as possible sensors, and sophisticated controllers. The controllers use the model and the sensor measurements (e.g., current, voltage, temperature, etc.) to calculate/estimate the other states (e.g., state of charge, state of health), predict the future performance based on the external power demand (e.g., how much power and how long the pack can provide it, how much life will be left and when maintenance will be needed) so that the BMS can adjust the cells use, protect the cells from thermal runaway and other safety issues, balance the cells according to not only state of charge (SOC) but also state of health (SOH), maintain their service lives, and optimize the overall pack performance.

There are several challenges in front. First, to have accurate estimation of SOC/SOH requires an underlying model including the predominant aging mechanisms but usually such a comprehensive model is complicated and computationally so expensive that it cannot be handled by a small on-board microprocessor. Second, more sensors make it

easier for system engineers to design high performance controllers. Given the limited space within the pack and the large number of cells, it is typically not practical to have the detailed measurements that can be made in a laboratory setting. Third, in industrial applications, many manufacturing parameters such as acid concentration, saturation, and grid composition, needed for controllers design are not available due to IP agreements or contracts which drives engineers to add extra on-board sensing or use estimators based models.

The work proposed aims to tackle these problems from both software and hardware. To develop low-order, control-oriented, and electrochemistry-based model for BMS, discretization modeling approaches are investigated and compared according to their efficiency and accuracy. To enhance BMS' ability of SOC/SOH estimation, a nondestructive aging diagnosis tool and a battery testing station are designed and built. The testing station is capable of performing multiple tests like cycling and electrochemistry impedance spectroscopy (EIS). In contrast, it usually takes couple separate machines in a laboratory to conduct these tests. Besides, the testing station also provides an environment with real-time feedback to implement control algorithms. The nondestructive aging diagnosis tool utilizes the testing station to load cells with different current profiles and find unique signatures of degradation mechanisms. It is able to identify water loss and hard sulfation in aged cells. Further, a desulfation charge control is proposed to recover capacity in the sulfated cell. The desulfation charge control also uses the same experiment setup as aging diagnosis. The controller aims to remove hard sulfation crystal by overcharging the cell while monitoring pressure increase to suppress excessive gas generation, another aging mechanism that is likely to occur during overcharge and causes capacity fade. Last, the modeling and experiment techniques are integrated to motivate the development of a charge control that reduces/delays aging in cells and optimizes the service life of battery packs, a cell balancing scheme that narrows the distribution of cell SOHs instead of just cell voltages, a safety control that dynamically adjusts the operation constraints of each cell. The ultimate goal is to increase the utilization of batter packs, reduce their sizes and costs, improve their operation performance and safety, and prolong their service life.

1.1 Background and Previous Work

1.1.1 Lead-Acid Batteries and Their Aging Mechanisms

Lead-acid is the most widely used chemistry for batteries in stationary and hybrid applications, with the majority consisting of a valve-regulated lead-acid (VRLA) design. A VRLA cell consists of two electrodes and a layer of separator in between. When being discharged, the cell generates energy by having lead, lead dioxide, and sulfuric acid react with each other to produce lead sulfate and water. When being charged, it absorbs energy to decompose lead sulfate back into lead, lead dioxide, and sulfuric acid. The chemical equations for the primary reactions are

$$\text{(Positive electrode)}\ \ \mathrm{PbSO_4 + 2H_2O} \underset{discharge}{\overset{charge}{\rightleftharpoons}} \mathrm{PbO_2^- + 3H^+ + 2e^-}, \tag{1.1}$$

$$\text{(Negative electrode)}\ \ \mathrm{PbSO_4 + H^+ + 2e^-} \underset{discharge}{\overset{charge}{\rightleftharpoons}} \mathrm{Pb + HSO_4^-}. \tag{1.2}$$

The overall cell potential is

$$E^o_{cell} = 1.931, \tag{1.3}$$

but the actual cell potential E_{cell} depends on acid concentration, as described by the Nernst Equation [1],

$$E_{cell} = E^o_{cell} + \frac{RT}{nF} ln\left(\frac{c_{H^+} \cdot c_{HSO_4^-}}{c_{H_2O}}\right), \tag{1.4}$$

where $R = 8.314 J/(K\,mol)$ is the universal gas constant, $F = 9.64810^{-4} C/mol$ is Faraday's constant, T is the temperature in kelvins K, n is the number of moles of electrons transferred, and a_{H_2O}, a_{H^+}, and $a_{HSO_4^-}$ are the reactant concentrations. Therefore, the cell potential is always increasing when being charged because the acid is produced.

When the cell is overcharged, side reactions, water electrolysis, may occur. Oxygen evolves and hydrogen recombines at the anode and at the cathode, oxygen is oxidized and hydrogen is generated. The chemical equations for the side reactions are

$$\text{(Positive electrode)}\ \ \mathrm{2H_2O \rightarrow O_2 + 4H^+ + 4e^-}, \tag{1.5}$$

$$\mathrm{H_2 \rightarrow 2H^+ + 2e^-}, \tag{1.6}$$

$$\text{(Negative electrode)}\quad O_2 + 4H^+ + 4e^- \rightarrow 2H_2O, \tag{1.7}$$

$$2H^+ + 2e^- \rightarrow H_2. \tag{1.8}$$

The most common aging mechanisms for a VRLA battery include [2, 3, 4, 5, 6, 7, 8, 9, 10]:

- Positive electrode corrosion
- Irreversible hard sulfation
- Water loss/dry-out
- Positive electrode softening and shedding
- Electrolyte stratification
- Internal short-circuit
- Mechanical damage (current connector failure, case damage, *etc.*)
- Others (passive lead oxide film, thermal runaway, *etc.*)

They are often not independent from each other and multiple mechanisms can occur in one cell. VRLA batteries are designed to minimize these effects as much as possible but the operating environment, cell-to-cell and battery-to-battery manufacturing variations, and use can cause different degradation mechanisms to dominate capacity loss and/or impedance rise.

1.1.2 Discretization Modeling Methods

Accurate mathematical models are crucial for optimal energy storage system design and real-time estimation, prediction, and control, especially in hybrid applications which demand sophisticated design and control to provide high energy/power density and long cycle life. Fundamental models have been developed for lead-acid batteries [11, 12, 13], NiCd/NiMH batteries [14, 15, 16], lithium-ion batteries [17, 18, 19] and fuel cells [20, 21]. These models can accurately predict the system performance once the nonlinear and coupled partial differential differential equations (PDEs) that comprise the model are solved numerically using, for example, the control-volume method [15].

Other researchers propose equivalent circuit models [22, 23] but the model parameters lack physical meaning and connection to the underlying the electrochemical processes. Compared to complex electrochemistry models and empirical equivalent circuit models, control engineers seek a compromise in between which keeps the physical links in model variables and parameters but still can be simulated by BMS in a manageable time frame. One approach is to spatially discretize the electrochemical model. A wide variety of discretization methods are available to obtain models that are low-order while preserving the connection with the fundamental electrochemical governing equations. These discretization methods will have distinct pros and cons when modeling battery systems with different chemistries, goals and requirements.

1.1.3 Nondestructive Experiment Methods

In VRLA batteries, the operating environment, cell-to-cell and battery-to-battery manufacturing variations, and use can cause different degradation mechanisms to dominate capacity loss and/or impedance rise. With accurate State of Health (SOH) monitoring, cell usage can be adjusted by BMS to optimize the performance and life of the energy storage system. The BMS must be able to determine in real-time the predominant degradation mechanism for each cell and adjust use accordingly.

To perform real-time aging diagnosis in vehicles/locomotives, nondestructive techniques with as few sensors as possible are favored because switching out an aged cell from a pack and examining it using laboratory tools/methods costs a lot of labor and system downtime and can only be performed at very low frequency. Many studies that investigate aging in VRLAs use destructive techniques to identify degradation mechanisms. Studying a dissected battery using a scanning electron microscope and chemical analysis provides a physical understanding of aging processes, such as hard lead sulfate formation [24, 25, 26] or corrosion layer growth [27, 28]. Although these invasive techniques provide detailed information about the SOH of the battery, they can only be used posthumously. With nondestructive monitoring techniques, on the other hand, the BMS can diagnosis aging and implement unique charging strategies to extend service life.

Nondestructive techniques are also essential for accurate SOH estimation in real time. Most nondestructive techniques for on-line SOC/SOH estimation are model-based [29, 30, 31, 32] and require accurate model fitting. The techniques developed

so far, however, do not specify the degradation mechanisms that cause battery aging or use models which requires **a priori** knowledge of major degradation. Trying to include every possible failure mode in the model can result in computationally-expensive models that on-board BMS cannot handle. Analyzing data from nondestructive tests may offer an alternative to a model-based approach for SOH estimation. Nondestructive tests that require only current and voltage data include: full change/discharge cycling, pulse train, and Electrochemical Impedance Spectroscopy (EIS). In particular, EIS is influenced by SOC [33] and the shape of the impedance curve is often related to degradation mechanisms, such as gassing at a single electrode [34].

1.1.4 Sulfation Identification and Remediation

Batteries in a pack may age due to variations in manufacturing, operation environment and usage. With the ability to determine in real time the predominant degradation for each cell, battery management system (BMS) can predict the cell SOH accurately, adjust cell use accordingly and balance cells with respect to their health conditions so as to extend service life of the battery pack. The ability to not only identify degraded cells within a VRLA battery but also to restore their capacity could dramatically prolong battery life. Typical VRLA batteries have multiple cells connected in series. As the battery ages, the cell capacities diverge and the cell with the lowest capacity limits the overall battery capacity. A BMS that identifies sulfated cells and has the ability to desulfate those cells could increase the overall capacity of an aged battery.

Negative plate sulfation is one of the most prominent aging mechanisms for VRLA batteries and is especially common in hybrid vehicle applications [35, 36]. Lead dioxide and lead are discharged in sulfuric acid to form lead sulfate and water. The reaction reverses during charge, lead sulfate being decomposed to produce lead dioxide and lead. Both reactions take place via dissolution-precipitation processes. During discharge, electrons are transferred to form lead ions then dissolved into the solution and supersaturation of Pb^{2+} may be achieved. After the nuclei are formed, $PbSO_4$ precipitates and the size of the $PbSO_4$ crystals depends on the concentration of sulfuric acid and the current density. During charge, lead sulfate dissolves into Pb^{2+} and SO_4^{2-}. Then electron transfer occurs on the electrode grid and the ions are oxidized/reduced to PbO_2 and Pb. This process is greatly affected by the current density, the diffusion rate, the

crystal size and the solubility of $PbSO_4$. In addition, the reaction area changes by several orders of magnitude during the reactions. The lead sulfate crystals formed through electrochemical process have rough surfaces with high porosity and activity. Therefore, the lead ions may dissolve from the crystals and re-crystallize back, a process known as Ostwald ripening. Crystals formed in recrystallization have finer surfaces with higher density and lower activity. Hence, these lead sulfate crystals have less reaction area and are much more difficult to be converted back during charge. Gibson *et al.* [24], Yamaguchi *et al.* [25], and Takehara [26] have thoroughly studied and developed an understanding of the structure and recrystallization of hard crystalline lead sulfate in greater details. To reduce or remove of irreversible hard sulfation is basically to keep charging/overcharging a cell until all the lead sulfate crystals decompose back into lead, lead dioxide and acid.

Electrolyte stratification is another common failure mode for lead-acid batteries. It is considered to be most severe in flooded batteries, much less prominent in AGM batteries and not significant at all in gelled batteries due to the immobilized electrolyte [37, 38, 39]. Electrolyte stratification causes a vertical distribution of acid and promotes the formation of irreversible lead sulfate in the lower parts of the electrodes [40, 41]. Electrolyte stratification can be also mitigated by overcharging and gassing [10, 39, 40, 42]. Therefore, electrolyte stratification can be considered as a cause of hard sulfation and classified into the same category of aging.

Approaches to reducing sulfation include, from manufacturers' perspectives, adding carbon additives [43, 44] and expander components [9, 45, 46], replacing the negative electrode with carbon [35, 47, 48], and from users' perspectives, using high-frequency pulse charge [49, 50]. Control engineers focus more on the latter. Lam *et al.* found pulsed charging to be a promising approach towards enhancing the cycle life of Pb-Sb and Pb-Ca-Sn cells [51]. Keyser *et al.* proposed to use high finishing currents and current-interrupt charging algorithm to minimize sulfation and gassing during cycling [52]. However, it is also a drawback of desulfation that it has to be performed at high SOC at which hydrogen and oxygen production associated with the electrolysis of water molecules can lead to water loss, another aging mechanism that decreases cell capacity. Hence, desulfation techniques must minimize water loss to effectively recover lost capacity.

1.1.5 System Modeling of Charge and Overcharge

For systems/control engineers, an intelligent battery management system (BMS) design should be based on a very accurate yet computationally efficient model, as few sensors as possible, and high performance controllers. The controllers use the model and sensor measurements (e.g., current, voltage, temperature, etc.) to calculate/estimate the other states (e.g., state of charge, state of health), predict the future performance based on the external power demand (e.g., how much power and how long the pack can provide it or how much life is left and when maintenance is needed), protect the cells from thermal runaway and other safety issues, balance the cells according to not only state of charge (SOC) but also state of health (SOH), and optimize the overall pack performance. To design such an advanced BMS, models with high fidelity and low computational costs are needed.

For lead-acid batteries, comprehensive multiphase, electrochemical and thermally coupled 3D models have been developed [53, 54, 55, 12, 56]. These models involved nonlinear coupled partial differential algebraic equations and are solved numerically using a computationally intensive approach. Pb-acid battery packs used in hybrid applications often operate at high SOC during overcharge when highly nonlinear behavior resulting from side reactions (e.g., electrolysis or gassing) are likely to occur. In the literature, gassing has been thoroughly investigated [57, 58, 59, 60, 61, 1, 62] and modeled both explicitly and empirically [63, 64, 34, 65]. These electrochemical models are mathematically complex and difficult to use for system engineering. Empirical models [66, 67, 68, 69, 6, 22] are computationally simple but suffer from linearization and often approximations and are divorced from the fundamental processes that govern cell dynamics. Even though there are a lot of study on the overcharge process, there are few system models that covers lead-acid cell overcharge behavior.

1.1.6 Charge Strategies for Lead-acid batteries

Charge strategy plays an important role in cycle life because in a lead-acid cell, side reactions may occur during charge and overcharge, such as gassing and corrosion. Charging algorithms are often specified by particular applications, e.g., standby, engine start, traction, etc, to guarantee performance and service life. For hybrid/electric vehicles, people aim to charge VRLAs in a short time without hurting the battery life.

A lot of researchers have shown the effect of different charge strategies on the cell life. It has been found that the charge current profile, charge time, initial charge current and depth of discharge can all effect the cycle life of lead-acid batteries [70]. Charge strategy in high SOC regime and its termination criteria can effect battery cycle life, too [71]. Using more micro steps of constant current charge can be beneficial, improving life and charge efficiency [72, 73]. Generic algorithm can also be applied to optimize the charge current [74]. When close to full charge or overcharge, pulse charge has been shown to improve charge efficiency and prolong service life [52, 75, 76]. Also, suppressing side reactions by carefully regulating charge current will definitely help protect batteries [77, 78].

1.2 Contribution and Organization of Thesis

Chapter 2 examines six discretization methods that can assist control engineers to develop accurate low-order electrochemistry-based system models of batteries. The six methods are Analytical Method (AM), Integral Method Approximation (IMA), Padé Approximation Method (PAM), Ritz Methods (RM), Finite Element Method (FEM), and Finite Difference Method (FDM). A two-domain electrolyte diffusion problem is proposed as benchmark. The six methods are investigated and compared based on both their accuracy and efficiency which are quantitatively measured using L_2 and L_∞ error metrics and their implementation difficulties which are qualitatively analyzed according to the amount of symbolic analysis involved, the flexibility of the resulting model, etc. System order is the critical factor for fast computation and real-time implementation so the convergence and accuracy of the different techniques as a function of the number of integrators in the model is studied.

Chapter 3 proposes a nondestructive forensic pathology to perform online aging diagnosis of lead-acid cells using only current, voltage and pressure measurements of cells. A battery testing station has been designed and built, consisting of Matlab/Simulink as the model and controller, ControlDesk/dSPACE as the user interface and data acquisition, a linear amplifier as the power source/sink, and sensors. It can conduct conventional electrochemical test such as cycling, pulse train, and electrochemical impedance spectroscopy (EIS) and control algorithms requiring real-time feedback as well. Two VRLA batteries of the same make, one fresh new and one aged, are tested

side by side. Water loss and hard sulfation are diagnosed to be responsible for the death of the cells in the aged battery.

Continuing on the work in Chapter 3, Chapter 4 presents a desulfation charge control which utilizes the pressure measurement as feedback. For a lead-acid cell, removal of hard sulfation requires overcharge at the risk of introducing excessive gassing which can also cause capacity loss. Besides, limiting gassing during overcharge often leads to tiny trickle charge current as a result of control law which greatly prolongs the charge time and reduces the efficiency. The proposed algorithm adjusts the input current according to the pressure change in the cell. In this way, it manages to input charge at maximum possible current so as to remove hard sulfation crystals and restore the cell capacity while suppressing the gassing introduced during charge/overcharge to the minimum.

Cooperating a gassing-included performance model with the desulfation charge control can eliminate the use of the pressure measurements. That motivates the work presented in Chapter 5, a nonlinear 5th-order state space model including degradation. It preserves the electrochemical processes and parameters of the underlying PDE model. It was validated with testing data and showed good accuracy in capturing the voltage and the pressure responses during charge and overcharge. The model also captured the potentials, reaction current densities, and gassing responses observed in the fundamental model, making it well suited for model-based analysis, simulation, estimation, and BMS design.

With the system model developed in Chapter 5, Chapter 6 proposes a health-cautious charge strategy, constant-current constant-overpotential (CC-Cη). One can choose to control η either on the positive electrode or the negative electrode. The former one controls oxygen generation directly but also affects the η on the negative electrode, and vice versa. Both strategies were compared with the conventional constant-current constant-voltage (CC-CV) charge protocols. CC-Cη were shown to have better control of gas generation during overcharge and improve charging efficiency. But the trade-off is longer charge time if the same ending current is achieved. If the same charge time, less gassing was seen under CC-Cηcharge protocols. Besides, a SOC estimation based on internal acid concentration is adopted. A current-counting-based SOC estimator has rising error in high SOC region due to that the side reactions kick in and share part of the income energy. The SOC estimator based on the internal acid concentration overcomes that, which is more suitable for overcharge.

Chapter 2

Discretization Methods for Battery Systems Modeling

2.1 Introduction

Low-order electrochemistry-based model is a key element in a sophisticated battery management system (BMS). Most electrochemical battery models are presented in highly nonlinear and complicated partial differential equations. This chapter reviews six discretization methods (Analytical Method, Integral Method Approximation, Padé Approximation Method, Ritz Method, Finite Element Method, Finite Difference Method) which can transfer the complex electrochemical models into simple but accurate system models.

To compare the various discretization techniques, a benchmark problem shown in Fig. 2.1 is proposed and used throughout the work. The electrolyte phase diffusion problem for a battery cell with uniform reaction current distribution and two coupled domains includes many of the key features of battery cell models, including diffusion dynamics and spatially varying inputs and parameters. The two domains correspond to a porous negative electrode ($0 < x < L/2$) and a porous positive electrode ($L/2 < x < L$). For simplicity, the two electrodes are assumed to be the same length ($L/2$) and that the diffusion coefficients and electrode phase volume fractions are different for (but constant within) the two electrodes. The current density $j(t) = 2I(t)/(AL)$ for the negative electrode and $j(t) = -2I(t)/(AL)$ for the positive electrode where A is the

electrode plate area and $I(t)$ is the total current flowing through the cell. Thus, the coupled domains model consists of the two field equations

$$\begin{aligned} \varepsilon_m \frac{\partial c}{\partial t} &= D_m \frac{\partial^2 c}{\partial x^2} + b\, I \quad \text{for } x \in (0, L/2), \\ \varepsilon_p \frac{\partial c}{\partial t} &= D_p \frac{\partial^2 c}{\partial x^2} - b\, I \quad \text{for } x \in (L/2, L), \end{aligned} \tag{2.1}$$

where $c(x,t)$ is the ion concentration and ε_m and ε_p and D_m and D_p are the electrode phase volume fractions and diffusion coefficients for the negative and positive electrode, respectively. The diffusion coefficients depend on a reference diffusion coefficient D^{ref} and the phase volume fractions as follows:

$$D_m = D^{ref} \varepsilon_m^{1.5} \text{ and } D_p = D^{ref} \varepsilon_p^{1.5},$$

The input constant

$$b = \frac{2(1-t_0)}{F A L}, \tag{2.2}$$

where t_0 is the transference number and F is Faraday's constant. Ions do not flux through the boundaries so the boundary conditions

$$\left.\frac{\partial c}{\partial x}\right|_{x=0} = \left.\frac{\partial c}{\partial x}\right|_{x=L} = 0, \tag{2.3}$$

$$\begin{aligned} D_m \left.\frac{\partial c}{\partial x}\right|_{x=(L/2)_-} &= D_p \left.\frac{\partial c}{\partial x}\right|_{x=(L/2)_+}, \\ c\left(\frac{L}{2}_-, t\right) &= c\left(\frac{L}{2}_+, t\right), \end{aligned} \tag{2.4}$$

At the interface between the two domains, the boundary conditions Eq. (2.4) couple the two domains by ensuring continuity of concentration and flux through the boundary at $x = L/2$. In this problem, the output is taken to be $y(t) = c(L,t) - c(0,t)$ because the output voltage for a cell typically depends on the concentration difference between the two electrodes.

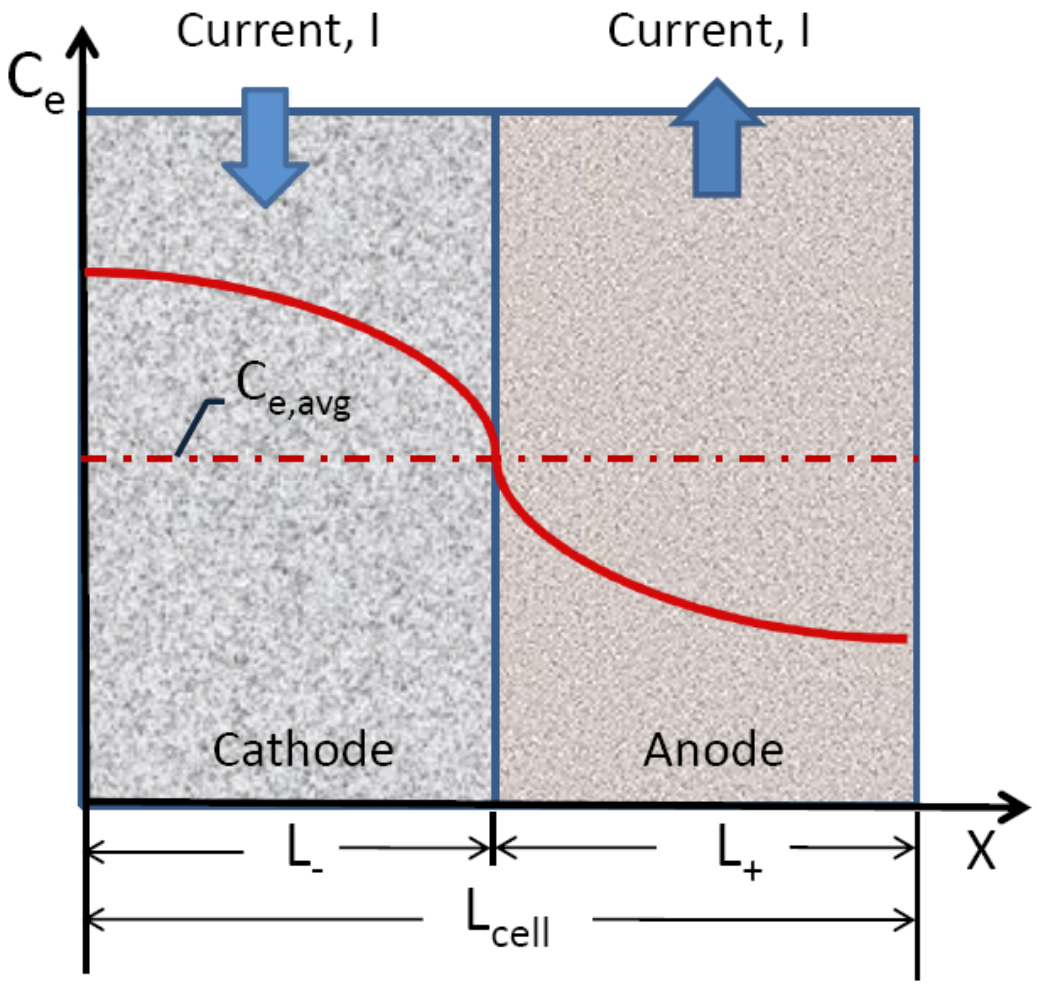

Figure 2.1. Schematic diagram of the benchmark electrolyte diffusion problem

2.2 Discretization Methods

2.2.1 Analytical Method (AM)

Most of the PDEs that are encountered in battery systems are approximately linear with constant coefficients so we can often find an exact or analytical solution. In this section, we exactly solve the benchmark electrolyte diffusion problems. More information on analytical methods can be found in [79, 80, 81, 82].

Two approaches are used to analytically/exactly solve the benchmark problem. First, we use the separation of variables to generate an eigenvalue problem that is then solved. The spatially distributed response is calculated from a eigenfunction series expansion.

If the eigenfunction expansion is truncated then the resulting model can be put in state variable form, allowing time and frequency response calculations. Second, we use the Laplace transform to eliminate time derivatives and solve the resulting ordinary differential equations for a transcendental transfer function. This allows calculation of the exact frequency response without truncation of the eigenfunction series but the transcendental transfer function cannot be directly used for time simulation.

Eigenfunction Expansion: The eigenvalue problem is derived by substituting $c(x,t) = C(x)e^{\lambda t}$ into Eqs. (2.1) with $I(t) = 0$ to produce

$$\begin{aligned} \varepsilon_m \lambda C_m - D_m C_m'' = 0 \quad \text{for } x \in (0, L/2), \\ \varepsilon_p \lambda C_p - D_p C_p'' = 0 \quad \text{for } x \in (L/2, L). \end{aligned} \tag{2.5}$$

The solutions of Eqs. (2.5) are

$$\begin{aligned} C_m(x) = C_{1m} e^{\beta_m x} + C_{2m} e^{-\beta_m x}, \\ C_p(x) = C_{1p} e^{\beta_p x} + C_{2p} e^{-\beta_p x}. \end{aligned} \tag{2.6}$$

Substitution of Eqs. (2.6) into Eqs. (2.5) produces

$$\lambda = \frac{D_m \beta_m^2}{\varepsilon_m} = \frac{D_p \beta_p^2}{\varepsilon_p} \tag{2.7}$$

or

$$\beta_m = \alpha \beta_p, \; \varepsilon_m = \zeta \varepsilon_p, \text{ and } D_m = \frac{\zeta D_p}{\alpha^2} \tag{2.8}$$

where

$$\alpha = \sqrt{\frac{D_p \varepsilon_m}{D_m \varepsilon_p}} \text{ and } \zeta = \frac{\varepsilon_m}{\varepsilon_p} \tag{2.9}$$

Substitution of Eq. (2.7) into the solutions Eqs. (2.6) and then into the boundary conditions Eqs. (2.3) and (2.4) produces the matrix equation

$$\mathbf{Mc} = \mathbf{0}, \tag{2.10}$$

where $\mathbf{c} = [C_{1m}, C_{2m}, C_{1p}, C_{2p}]^T$ and

$$\mathbf{M} = \begin{bmatrix} \alpha\beta_p & -\alpha\beta_p & 0 & 0 \\ \alpha\zeta\beta_p \mathrm{e}^{\frac{1}{2}\alpha\beta_p L} & -\alpha\zeta\beta_p \mathrm{e}^{-\frac{1}{2}\alpha\beta_p L} & -\alpha^2\beta_p \mathrm{e}^{\frac{1}{2}\beta_p L} & \alpha^2\beta_p \mathrm{e}^{-\frac{1}{2}\beta_p L} \\ \mathrm{e}^{\frac{1}{2}\alpha\beta_p L} & \mathrm{e}^{-\frac{1}{2}\alpha\beta_p L} & -\mathrm{e}^{\frac{1}{2}\beta_p L} & -\mathrm{e}^{-\frac{1}{2}\beta_p L} \\ 0 & 0 & \beta_p \mathrm{e}^{\beta_p L} & -\beta_p \mathrm{e}^{-\beta_p L} \end{bmatrix}. \tag{2.11}$$

Eq. (2.11) has nonzero solutions if the determination of $\mathbf{M}$ satisfies

$$\begin{aligned} |\mathbf{M}| = &-\alpha^2\beta_p^3 \Big[(\zeta - \alpha) \left(\mathrm{e}^{-\beta_p \gamma_1} - \mathrm{e}^{\beta_p \gamma_1} \right) \\ &+ (\zeta + \alpha) \left(\mathrm{e}^{-\beta_p \gamma_2} - \mathrm{e}^{\beta_p \gamma_2} \right) \Big] = 0 \end{aligned} \tag{2.12}$$

where $\gamma_1 = L(\alpha - 1)/2$ and $\gamma_2 = L(\alpha + 1)/2$. Note that the eigenvalue problem in Eq. (2.12) reduces to

$$e^{\beta L} - e^{-\beta L} = 0, \tag{2.13}$$

if $\alpha = 1$ and $\zeta = 1$ because this is corresponds to the single domain problem with $D_p = D_m$ and $\varepsilon_p = \varepsilon_m$. Eq. (2.12) can also be written using hyperbolic functions as

$$\beta_p{}^3 \left[(\zeta - \alpha) \sinh(\beta_p \gamma_1) + (\zeta + \alpha) \sinh(\beta_p \gamma_2) \right] = 0 \tag{2.14}$$

Eq. (2.12) has only imaginary roots $\beta_p = \sqrt{\varepsilon_p \lambda / D_p}$ corresponding to real and negative eigenvalues $\lambda < 0$. These roots are found numerically and substituted into Eq. (2.11), making $\mathbf{M}$ singular. The eigenvector corresponding to the zero eigenvalue provides the eigenfunction coefficients $C_{1m}, \ldots, C_{2p}$. These eigenfunctions are orthogonal. The elements of the $\mathbf{B}$ vector are

$$b_n = \int_0^{L/2} b\, C_n(x)\, dx - \int_{L/2}^{L} b\, Cn(x)\, dx. \tag{2.15}$$

The output is expressed as an eigenfunction series evaluated at $x = L$ minus $x = 0$.

Transfer Function: Laplace transform of Eqs. (2.1) produces

$$\begin{aligned} s\varepsilon_m C_m - D_m C_m'' - b\, I = 0 \quad &\text{for } x \in (0, L/2), \\ s\varepsilon_p C_p - D_p C_p'' + b\, I = 0 \quad &\text{for } x \in (L/2, L). \end{aligned} \tag{2.16}$$

The solutions of Eqs. (2.16) are

$$\begin{aligned} C_m(x) &= C_{1m}e^{\beta_m x} + C_{2m}e^{-\beta_m x} + \frac{b\,I}{\varepsilon_m s}, \\ C_p(x) &= C_{1p}e^{\beta_p x} + C_{2p}e^{-\beta_p x} - \frac{b\,I}{\varepsilon_p s}. \end{aligned} \tag{2.17}$$

Substitution of Eqs. (2.17) into Eqs. (2.16) produces

$$s = \frac{D_m\beta_m^2}{\varepsilon_m} = \frac{D_p\beta_p^2}{\varepsilon_p} \tag{2.18}$$

and the same relationships in Eq. (2.8) and (2.9). Substitution of Eq. (2.18) into the solutions (2.17) and then into the boundary conditions Eqs. (2.3) and (2.4) produces four linear equations in four unknowns $C_{1m},\ldots,C_{2p}$. The transfer function

$$\frac{D_p\,Y(s)}{b\,\varepsilon_p\,I(s)} = \frac{\begin{array}{c} 4\,\alpha\,\sinh\left(\frac{1}{2}\beta_p L\right) - 2\,(\zeta-\alpha)\sinh(\beta_p\,\gamma_1) \\ +\,4\,\zeta\,\sinh\left(\frac{1}{2}\alpha\,\beta_p L\right) - 2\,(\zeta+\alpha)\sinh(\beta_p\,\gamma_2) \end{array}}{{\beta_p}^2\left[(\zeta-\alpha)\sinh(\beta_p\,\gamma_1) + (\zeta+\alpha)\sinh(\beta_p\,\gamma_2)\right]} \tag{2.19}$$

results from substituting these solutions into $Y(s) = C(L,s) - C(0,s)$. The characteristic equation corresponding to the denominator of Eq. (2.19) matches that calculated from the eigenvalue approach in Eq. (2.14).

2.2.2 Integral Method Approximation (IMA)

Another way to convert the governing PDEs of a battery model to ODEs is to assume a distribution across the cell for the distributed variable of interest and integrate the governing equations to convert the PDE to a single ODE. In this section, the Integral Method Approximation (IMA) is applied to the benchmark problem. More information on the IMA can be found in [81, 83, 84, 85].

For the electrolyte diffusion problem with coupled domains described in Section 2.1, the IMA assumes that the concentration has parabolic distributions in each domain

$$c(x,t) = \begin{cases} c_{0m}(t) + c_{1m}(t)x + c_{2m}(t)x^2 & \text{for } x \le L/2, \\ c_{0p}(t) + c_{1p}(t)x + c_{2p}(t)x^2 & \text{for } x \ge L/2. \end{cases} \tag{2.20}$$

The six coefficients in Eq. (2.20) can be solved from the two field equations ($x < L/2$ and $x > L/2$) and the four boundary conditions (2.3) and (2.4). Substitution ofb Eq. (2.20) into the Laplace Transform of Eq. (2.1) and integration yields

$$\begin{aligned}
&\int_0^{L/2} \left(s\varepsilon_m C - D_m C'' - bI\right) dx \\
&= \frac{\varepsilon_m L}{2} sC_{0m} + \frac{\varepsilon_m L^2}{8} sC_{1m} + \left(\frac{\varepsilon_m L^3 s}{24} - LD_m\right) C_{2m} - \frac{bL}{2} I \\
&= 0
\end{aligned} \tag{2.21}$$

$$\begin{aligned}
&\int_{L/2}^{L} \left(s\varepsilon_p C - D_p C'' + bI\right) dx \\
&= \frac{\varepsilon_p L}{2} sC_{0p} + \frac{3\varepsilon_p L^2}{8} sC_{1p} + \left(\frac{7\varepsilon_p L^3}{24} s - LD_p\right) C_{2p} + \frac{bL}{2} I \\
&= 0.
\end{aligned} \tag{2.22}$$

Eqs. (2.3) give

$$C_{1m} = 0 \ \text{ and } \ C_{1p} + 2LC_{2p} = 0. \tag{2.23}$$

Substitution of Eqs. (2.20) and (2.23) into the boundary conditions (2.4) yield

$$\begin{aligned}
D_m C_{2m} + D_p C_{2p} &= 0, \\
C_{0m} + \frac{L^2}{4} C_{2m} - C_{0p} + \frac{3L^2}{4} C_{2p} &= 0.
\end{aligned} \tag{2.24}$$

Solution of Eqs. (2.21) through (2.24) and substitution into the output equation

$$Y(s) = C(L,s) - C(0,s) = C_{0p} + C_{1p}L + C_{2p}L^2 - C_{0m} \tag{2.25}$$

gives the transfer function

$$\frac{Y(s)}{I(s)} = \frac{-3bL^2(\varepsilon_m + \varepsilon_p)(D_m + D_p)}{2\varepsilon_m \varepsilon_p L^2 (D_m + D_p) s + 24 D_m D_p (\varepsilon_m + \varepsilon_p)}. \tag{2.26}$$

The IMA can be extended to higher order approximations by evaluating the field equation at specific points in the domain. For each additional term in the approximation, an additional equation is added. In the coupled domain problem, for example, we can

add $c_{3m}x^3$ to the approximation in Eq. (2.20) and solve the additional equation

$$\begin{aligned}
&\varepsilon_m \frac{\partial c}{\partial t}\bigg|_{x^*} - D_m \frac{\partial^2 c}{\partial x^2}\bigg|_{x^*} - bI \\
&= \varepsilon_m \left(\dot{c}_{0m} + \dot{c}_{2m}x^{*2} + \dot{c}_{3m}x^{*3}\right) - D_m \left(2c_{2m} + 3c_{3m}x^*\right) - bI \\
&= 0
\end{aligned} \tag{2.27}$$

where $x^* \in [0, L/2]$. Eq (2.27) is a first order differential equation, increasing the order of the approximation by one. Additional terms can be added to the approximation in Eq. (2.20) with additional equations from Eq. (2.27) evaluated at different x^*.

2.2.3 Padé Approximation Method (PAM)

The analytical solutions for battery cell related models can often be expressed in terms of transcendental transfer functions like Eq. (2.19). These transfer functions often involve hyperbolic functions that can also be written in terms of exponentials. The Padé Approximation works well for these infinitely differentiable functions that can be expanded in a power series at the origin [86, 87, 88, 89]. The N^{th} order Padé approximation of a transfer function $G(s)$ is a ratio of two polynomials in s where the denominator is of order N. For a proper transfer function, the numerator is of order N or less. The Padé Approximation Method can produce transfer functions with numerators of order 1 to N. The numerator order can be adjusted to obtain the best fit or the numerator order that provides the desired phase at high frequency can be used. The computational speed of the model depends strongly on the number of integrators in the model or the order of the denominator, and, to a lesser extent, the multiplications and additions associated with the numerator. In this study, we focus only on model order as the computational cost metric so a high order numerator will probably provide the most accurate results.

We assume that the transfer function can be expanded in a power series at the origin as follows

$$G(s) = \sum_{k=0}^{2(N+1)} c_k \, s^k \tag{2.28}$$

where the coefficients c_k are calculated by repeated differentiation and evaluation of

$G(s)$ at $s = 0$,

$$c_k = \left. \frac{d^k\, G(s)}{ds^k} \right|_{s=0}. \tag{2.29}$$

If $G(s)$ has a pole at the origin then we apply the power series expansion to $G^*(s) = s\, G(s)$ and substitute $G = P/s$ where P is the Padé approximation of G^*. The N^{th} order Padé approximation transfer function

$$P(s) = \frac{\sum_{m=0}^{N} b_m\, s^m}{1 + \sum_{n=1}^{N} a_n\, s^n} = \frac{num(s)}{den(s)}, \tag{2.30}$$

where we assume that the denominator and numerator both have order N. To determine $P(s)$ we must calculate the $N+1$ b_m and N a_m coefficients. The zeroth order term in the denominator is assumed to have a unity coefficient to normalize the solutions. The $2N+1$ linear equations that can be solved for the coefficients are determined from the polynomial equation

$$den(s) \sum_{k=0}^{2(N+1)} c_k s^k - num(s) = 0 \tag{2.31}$$

where the coefficients c_k are known from the power series expansion. Equation (2.31) produces a polynomial of order $2N(N+1)$ in s. The right hand side equals zero for all s so the coefficients of s must be zero. The first $N+1$ coefficients of s depend on both the unknown a_n and b_n coefficients. The remaining coefficients depend only on a_n. Thus, we set the coefficients of s^{N+2} to s^{2N+1} equal to zero to solve for $a_1, \ldots, a_N$. Then we substitute these solutions $a_1, \ldots, a_N$ into the coefficients of s^0 to s^N and set them equal to zero to solve for $b_0, \ldots, b_N$.

2.2.4 Ritz Method (RM)

The Ritz Method maintains the inherent symmetry of the operators in the governing PDEs. In battery systems, diffusion equations are symmetric, producing real eigenvalues and exponentially decaying response. The discretized **A** matrices generated by the Ritz method are also symmetric, ensuring real eigenvalues. The convergence properties of Ritz expansions have also been thoroughly studied. The eigenvalues converge monotonically from below, starting with negative eigenvalues that are smaller (larger in magnitude) and increase as the number of terms in the series increases. A Ritz approxi-

mation will never overpredict an eigenvalue.

The response is approximated by admissible functions that are continuous across the domain $0 \leq x \leq L$. A Fourier series solution is used with functions that satisfy the zero flux boundary conditions at $x = 0, L$. Starting with a weak form of the governing equation (2.1) that incorporates the natural (flux) boundary conditions. The requirement for continuous concentration at the interface of the two domains will be automatically satisfied by the continuity of the sinusoidal functions.

The field Eq. (2.1) is converted to a weak form by premultiplying by an admissible function $C_n(x)$ and integrating,

$$\begin{aligned} &\int_0^L \varepsilon(x)\, C_n \dot{c}\, dx \\ &= \int_0^L C_n \left[D(x)c'' + b(x)I \right] dx \\ &= -\int_0^L DC_n' c'\, dx + b\left(\int_0^{L/2} C_n\, dx - \int_{L/2}^L C_n\, dx \right) I \end{aligned} \tag{2.32}$$

using integration by parts and the boundary conditions. The integral on the right hand side of Eq. (2.32) can also be broken into two integrations from $x = 0$ to $x = L/2$ and from $x = L/2$ to $x = L$ as was done for the integral on the right hand side. Substitution of the Ritz expansion

$$c(x,t) = \sum_{m=0}^{N-1} C_m(x) c_m(t) \tag{2.33}$$

into Eq. (2.32) produces

$$\begin{aligned} &\int_0^L C_n \sum_{m=0}^{N-1} C_m \varepsilon\, \dot{c}_m\, dx + \int_0^L DC_n' \sum_{m=0}^{N-1} C_m' c_m\, dx - \left(\int_0^L bC_n\, dx \right) I \\ &= \sum_{m=0}^{N-1} \left\{ \left[\int_0^L \varepsilon\, C_n C_m\, dx \right] \dot{c}_m + \left[\int_0^L DC_n' C_m'\, dx \right] c_m \right\} \\ &\quad - b\left[\int_0^{L/2} C_n\, dx - \int_{L/2}^L C_n\, dx \right] I \\ &= 0 \end{aligned} \tag{2.34}$$

or

$$\mathbf{M}_1 \dot{\mathbf{x}} = \mathbf{M}_2 \mathbf{x} + \mathbf{M}_3 I, \tag{2.35}$$

where $\mathbf{x}(t) = [c_0(t), \ldots, c_{N-1}(t)]^T$ and

$$\begin{aligned}
\mathbf{M}_1(k,l) &= \varepsilon_m \int_0^{L/2} C_n C_m \, dx + \varepsilon_p \int_{L/2}^{L} C_n C_m \, dx = \mathbf{M}_1(l,k) \\
\mathbf{M}_2(k,l) &= -D_m \int_0^{L/2} C_n' C_m' \, dx - D_p \int_{L/2}^{L} C_n' C_m' \, dx = \mathbf{M}_2(l,k) \\
\mathbf{M}_3(k) &= b \left(\int_0^{L/2} C_n \, dx - \int_{L/2}^{L} C_n \, dx \right)
\end{aligned} \tag{2.36}$$

The discretized differential equations in Eq. (2.35) can then be written in state space form

$$\begin{aligned}
\dot{x} &= \mathbf{A}x + \mathbf{B}u \\
y &= \mathbf{C}x + \mathbf{D}u
\end{aligned} \tag{2.37}$$

with

$$\begin{aligned}
&\mathbf{A} = \mathbf{M}_1^{-1}\mathbf{M}_2, \qquad \mathbf{B} = \mathbf{M}_1^{-1}\mathbf{M}_3 \\
&\mathbf{C} = [C_0(L) - C_0(0), \ldots, C_{N-1}(L) - C_{N-1}(0)] \\
&\mathbf{D} = 0
\end{aligned} \tag{2.38}$$

Again, we obtain symmetric $\mathbf{M}_1$ and $\mathbf{M}_2$ matrices so the eigenvalues are real.

In a Fourier Series approximate solution the admissible functions are sinusoidal with $C_n(x) = \cos(n\pi x/L)$. Substituting the Fourier Series solution into Eqs. (2.38) produces

$$\begin{aligned}
\mathbf{M}_1(1,1) &= \frac{L}{2}(\varepsilon_m + \varepsilon_p), \\
\mathbf{M}_1(k,k) &= \frac{L}{4}(\varepsilon_m + \varepsilon_p), \\
\mathbf{M}_1(k,l) &= 0 \quad \text{if } n+m = \text{even and } n \neq m, \\
\mathbf{M}_1(k,l) &= \frac{nL(\varepsilon_m - \varepsilon_p)(-1)^{\frac{n+m-1}{2}}}{\pi(n^2 - m^2)} \quad \text{if } n+m = \text{odd} \\
\mathbf{M}_2(k,k) &= -\frac{n^2\pi^2(D_m + D_p)}{4L}, \\
\mathbf{M}_2(k,l) &= 0 \ \text{ if } n+m = \text{even and } n \neq m, \\
\mathbf{M}_2(k,l) &= \frac{\pi n m^2 (D_m - D_p)(-1)^{\frac{n+m-1}{2}}}{L(m^2 - n^2)} \ \text{ if } n+m = \text{odd}
\end{aligned} \tag{2.39}$$

$$\mathbf{M}_3(k) = 0 \quad \text{if } n \text{ is even,}$$
$$\mathbf{M}_3(k) = \frac{2bL(-1)^{\frac{n-1}{2}}}{n\pi} \quad \text{if } n \text{ is odd}$$

here, $k = n+1$ and $l = m+1$ The output matrix $\mathbf{C} = [0,-2,0,-2,\ldots]$, indicating that the even modes are not directly observable in the output. From Eq. (2.39) the even modes are also not directly controllable from the input. The odd modes are coupled to the even modes through the non-diagonal terms in $\mathbf{M}_2$ and $\mathbf{M}_1$ so they influence the system response. A different output (*e.g.* $c(L/2,t) - c(0,t)$) would directly sense the even modes.

2.2.5 Finite Element Method (FEM)

The Finite Element Method (FEM) is based on a weak form of the governing equation as was used in the Ritz Method. Rather than choosing functions that exist over the entire domain, however, FEM discretizes the domain $x \in [0,L]$ into $N-1$ subdomains or elements

$$\Omega_m = [(m-1)h, mh], \quad m = 1,2,\ldots,N \tag{2.40}$$

In general, the length of each element can be varied to improve the accuracy in high flux regions and reduce the number of elements in regions with low gradients. For simplicity, we assume that the grid is uniform with each element having length h so $L = h(N-1)$. The concentrations at the endpoints of the domains are referred to as nodes $c_m(t) = c((m-1)h,t)$ for $m = 1,\ldots,N$. The N^{th} order FEM approximation has N nodes. FEM generates equations for the nodal dynamics that can be realized in state variable or transfer function forms. For more information and details on the FEM method, readers are referred to [80, 90].

2.2.6 Finite Difference Method (FDM)

The Finite Difference Method (FDM) is the simplest and most commonly used approach to the solution of the diffusion equations found in battery models. As with the finite element method, it easily handles spatially varying inputs and parameters. FDM can also be used on nonlinear problems. The method does not always maintain the symmetry of the underlying problem, however, and lacks the convergence guarantees of variational

(FEM and Ritz) methods. Further information on this method can be found in [80, 81, 91].

2.3 Model Response

The response of a battery cell to step changes in charge/discharge current reveals how the concentration, potential, current density, and terminal voltage change with time under constant current loading. The parameters for the benchmark problem are shown in Table. 2.1.

Table 2.1. Electrolyte Diffusion Model Parameters

Parameter	Value
L	$100\ \mu m$
t_0	0.363
A	$10,452\ cm^2$
D^{ref}	$2.6 \times 10^{-6}\ cm^2/s$
ε_m	0.332
ε_p	0.28

All the 6 methods have similar time and frequency responses. In this section, only the analytical methods will be discussed as an example. The time and frequency responses of the other methods are detailed in Appendix.A.

2.3.1 Time Response

The eigenvalues or poles of the analytical transfer function start at 0.14 rad/s, corresponding to a time constant of 7.1 seconds. The residues start at -1.05 and decrease with increasing frequency. The 26th residue is almost zero and the odd residues (1, 3, etc.) are generally several orders of magnitude smaller than the even residues.

The analytical discharge step response is shown in Fig. 2.2 for different truncation orders. The output is the difference in concentration across the cell $c(L,t) - c(0,t)$. The initial concentration is zero and current fluxes into the anode and fluxes out of the cathode, creating a negative change in relative concentration. The time response settles out in approximately five time constants (approximately 35 seconds) to the steady state

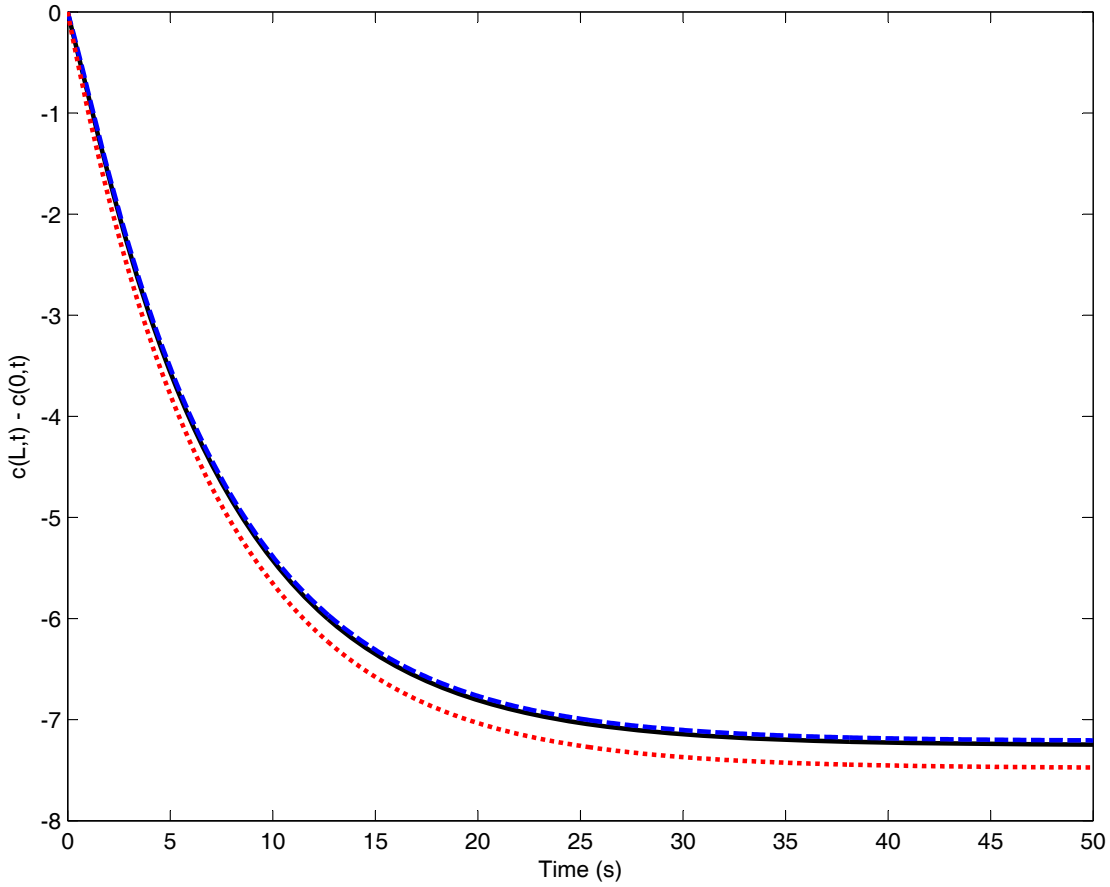

Figure 2.2. Discharge step response for analytical solution with 26 (solid - black), 4 (dashed - blue) and 2 (dotted - red) term approximations: Output concentration ($c(L,t) - c(0,t)$)

value. As the model order increases from 2 to 4 to 26 modes, the response converges. Figure 2.3 shows the evolution of the concentration distribution with time. The concentration is initially zero across the cell. As time moves on the concentration in then anode increases and the cathode decreases. The results are plotted as differences in concentration relative to $c(0,t)$ so the distribution is always negative. It is clear that the zero flux boundary conditions are enforced at $x = 0$ and $x = L$. At the junction between the two domains ($x = L/2$), the concentration and flux are continuous. The slope of the concentration distribution has a slight kink at $x = L/2$ associated with the change in diffusion coefficient.

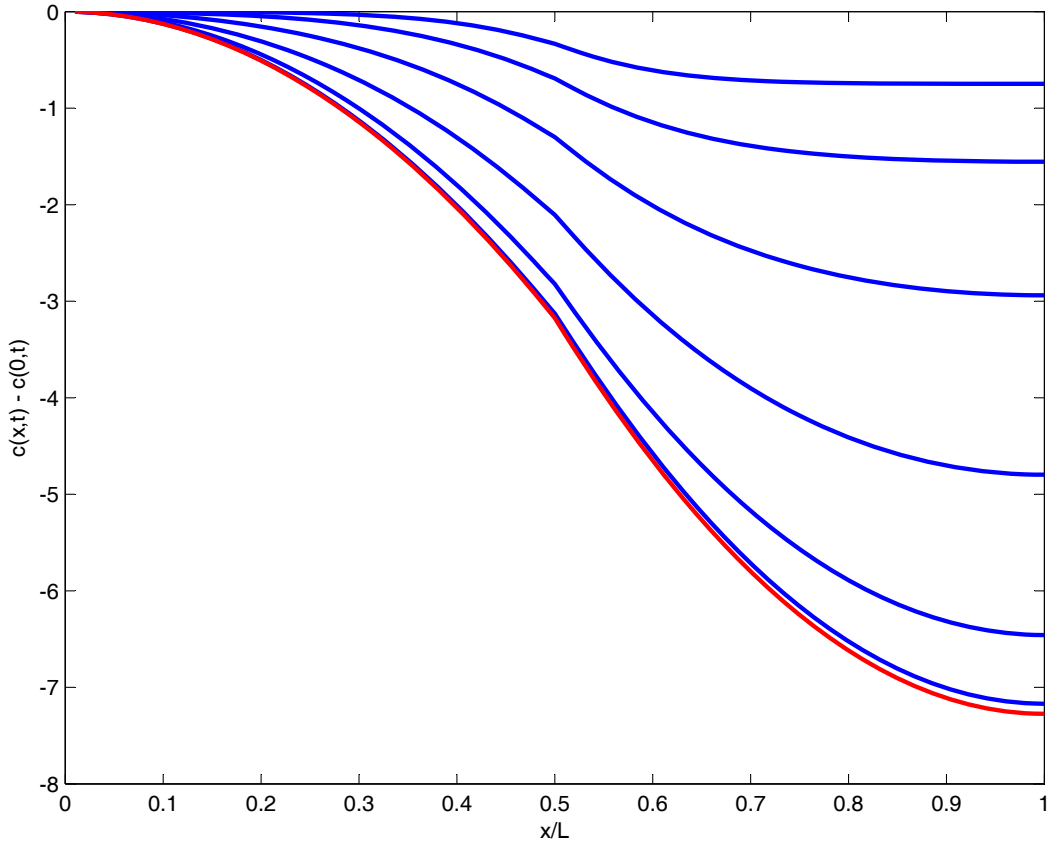

Figure 2.3. Discharge step response for analytical solution with 26 term approximation: Concentration distribution $c(x,t) - c(0,t)$ (blue) at t = 1, 2, 4, 8, 16, 32 seconds and the steady state response (red).

2.3.2 Frequency Response

Figure 2.4 shows the analytical frequency response of the electrolyte diffusion model is calculated by substituting $s = i\omega$ into the transcendental transfer function Eq. (2.19) and calculating the associated gain and phase. The overall shape of the concentration frequency response is that of a low pass filter. The concentration has a steady state response at low frequency and rolls off at high frequency. The corner frequency is around 3×10^{-2} Hz. The exact solution is hidden behind the analytical solution truncated to 26 modes. The analytical solution converges as the number of terms in the truncated series increases from 2 to 4 to 26. Again, only a few modes are required to accurately capture the frequency response across the bandwidth of interest.

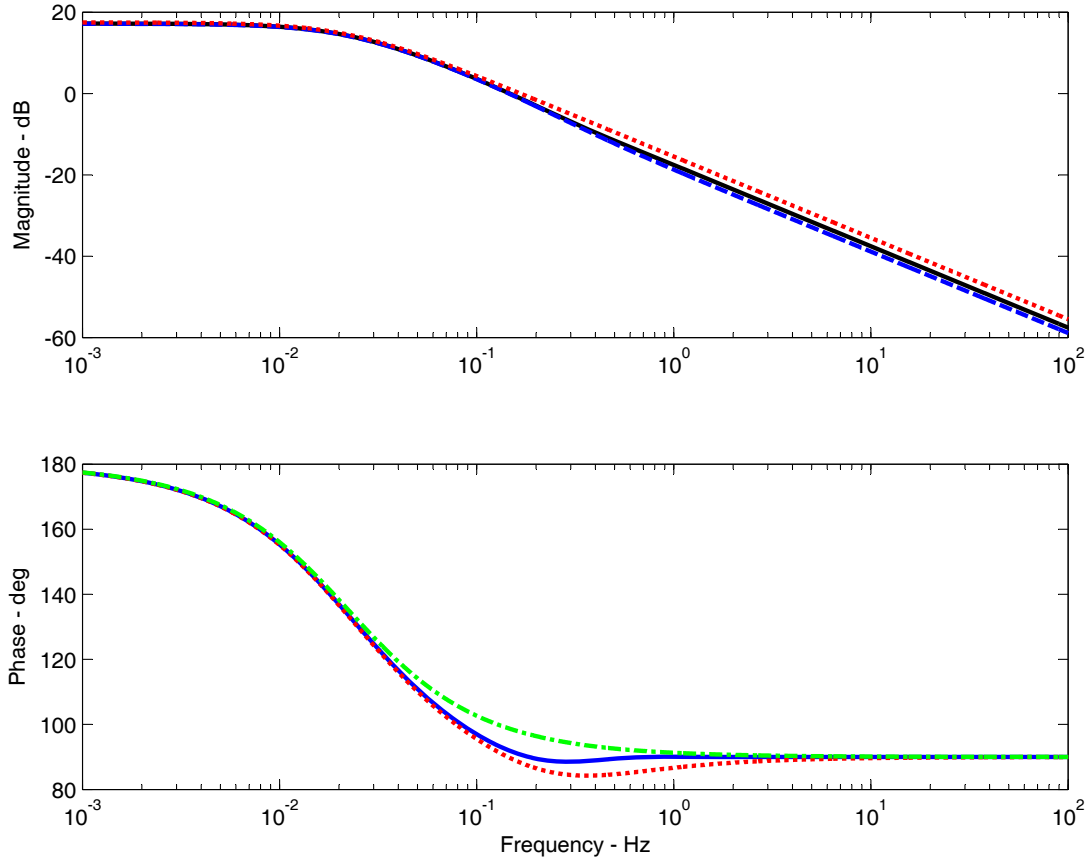

Figure 2.4. Frequency response for exact solution (solid-black) and analytical solution with 26 (dashed - blue), 4 (dash-dotted - green) and 2 (dotted - red) term approximations: Output concentration $(C(L,i\omega)-C(0,i\omega))/I(i\omega)$.

2.4 Modeling Cost, Convergence and Accuracy

To compare the convergence and accuracy of the various modeling methods, we introduce two error measurements that quantitatively compare the efficiency of the six methods using the L_2 norm and L_∞ norm. When calculating the accuracy, the 100th order analytical solution is adopted as the baseline model and the error is measured in both time domain and frequency domain.

Figures 2.5 and 2.6 show the errors versus truncation order, N, for the analytical method. All four error metrics approaches zero as the model order increases. The detailed error plots of the other methods are at the end of this chapter.

For IMA, the error decreases as the order increases in the frequency domain contin-

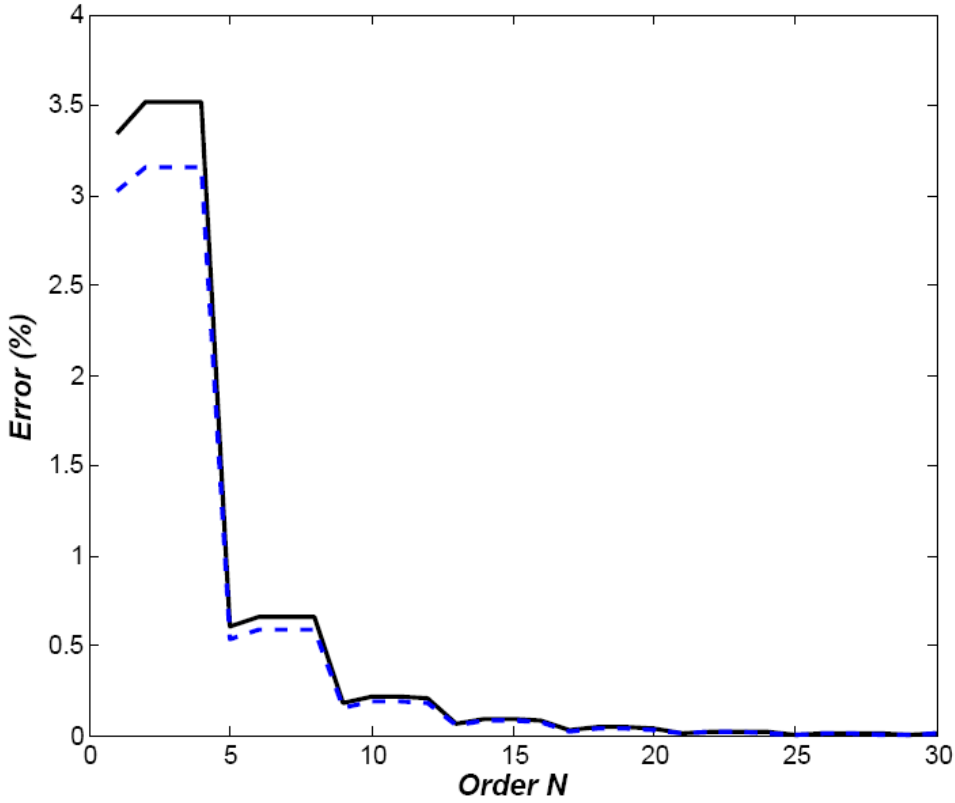

Figure 2.5. Error metrics for analytical method solution in time domain, L_2 norm (solid - black) and L_∞ norm (dashed - blue)

uously and smoothly, but in time domain, the error drops faster before 4th order and hits a plateau. Also, note that for IMA, its L_∞ norms are more significant than L_2 norms. Besides, IMA requires much lower order than the other methods except Padé to achieve the same error level but IMA involves tedious symbolic calculations to solve for the analytical expressions of all the parameters before one can implement it into the computers. To achieve 1% and 0.5% error level, one need IMA models with order 3 and 4.

Padé method can achieve pretty good accuracy with relatively low order and usually, that's preferred by control engineers regarding modeling. But similar to IMA, if the object transfer function is very complicated involving such functions as hyperbolic trigonometric ones, it takes plenty effort on symbolic calculation to solve for the coefficients prior to digital implement.

For Ritz method, its error decreases very quickly before hitting a minimum at 8th order, then stays in the plateau region as the model order keeps climbing up.It is probably

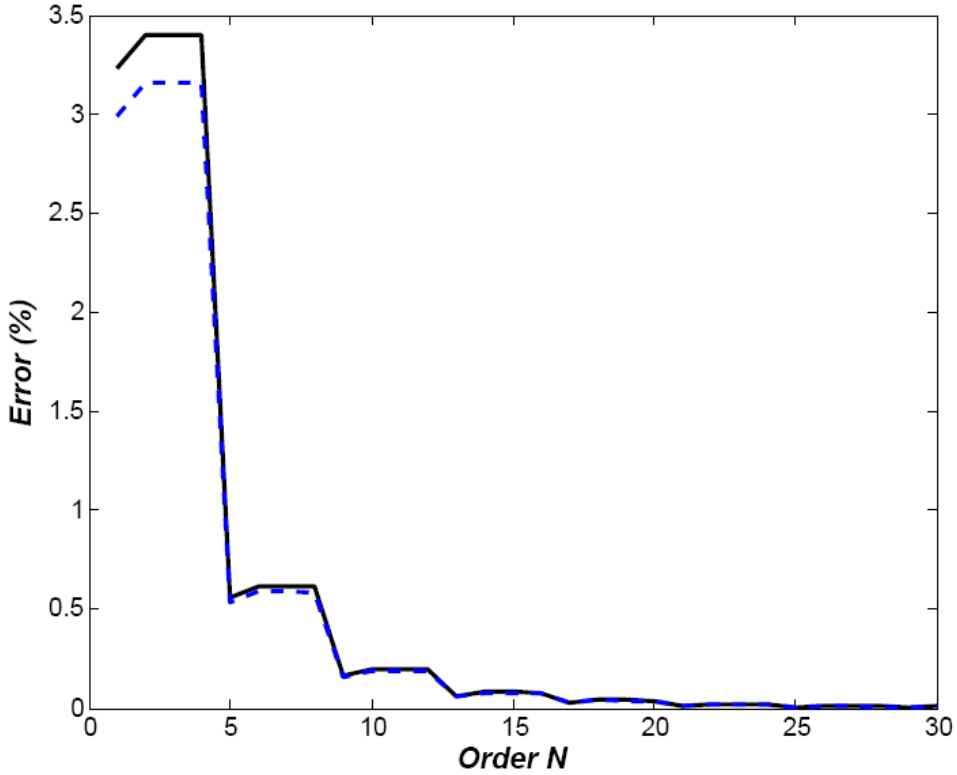

Figure 2.6. Error metrics for analytical method solution in frequency domain, L_2 norm (solid - black) and L_∞ norm (dashed - blue)

because that when the order increases there comes numerical issues when computing. When implementing, one advantage of the method is that all the matrices generated are symmetric which makes all the eigenvalues real. Another advantage is that it is very straight forward to implement into a computer since all the entries of the matrices are set.

FEM method converges at a moderate speed comparing to the others. Because for odd order, the nodes are not distributed unevenly into two domains, generally the odd orders have relatively higher error than the next even orders and the error drops in a zigzag shape. More, FEM does not require any symbolic analysis before going into computer implementation since the consistent of the matrices are the same no matter the order and the system parameters.

The error metrics for FDM also drops with the increase of the order but it requires much higher order than the other methods. Another, the errors for FDM models drop in a zigzag form which is basically caused by the uneven node in two domains. But as

a trade-off, FDM is mathematically straightforward, no symbolic calculations needed before hand as IMA or analytical methods and very easy to implement because the structures of the matrices don't change according to the order and the input parameters. To achieve 1% and 0.5% error level, FDM model with order 27 and 15 are necessary.

To summary, a crossover comparison of the six methods is listed in Table. 2.2 which shows the orders required to keep error under 1% and 0.5% for each methods.

Table 2.2. Approximation Order Required for Electrolyte Diffusion Problem

Method	Step Response				Frequency Response			
	L_2		L_∞		L_2		L_∞	
	0.5%	1%	0.5%	1%	0.5%	1%	0.5%	1%
PAM	1	1	2	2	3	3	3	3
IMA	4	3	4	4	4	3	4	3
RM	6	4	6	4	6	4	6	4
AM	9	5	9	5	9	5	9	5
FEM	10	10	10	12	10	12	10	14
FDM	27	15	27	15	27	15	27	15

2.5 Conclusions

For all the methods, the error convergences as the model order increases. The Padé approximation method converges the fastest. This method can only be applied to fairly simple problems where the power series can be determined analytically. The IMA and Ritz methods both use domain integration and provide the second and third best convergence. The Ritz method requires integration for all equations, complicating the process. As a variational method, however, the convergence is smooth and monotonic. The IMA equations are relatively easy to generate but the convergence characteristics are less well behaved. The analytical and FEM methods have similar convergence properties, coming in at fourth and fifth on the list. Both of these methods have guaranteed and smooth convergence properties. FDM is the least efficient method and lacks proven convergence properties but it is the easiest to formulate and solve. For the all of the methods the time and frequency domain L_2 and L_∞ error metrics are very close, but for IMA, its L_∞ norms are more significant than L_2 norms. This may imply that IMA method may have better

control on the total error energy. But as the trade-off of the convergence speed, IMA and Padé are somehow cumbersome and tedious to adjust the model order to reach the desired performance if one does not have any prior knowledge about how much error quantitatively is acceptable, since it needs to symbolically solve the explicit expressions for all the parameters involved; Analytical method costs a lot of effort and time to find the system eigenvalues iteratively and numerically. Both these methods require a lot of symbolic calculation prior to any computer implementation while Ritz, FEM and FDM methods are more straightforward, not requiring any mathematical analysis in advance since their structures are mostly unchanged regardless of the order and input parameters.

Chapter 3

Nondestructive Forensic Pathology of Lead-Acid Batteries

3.1 Introduction

Another key function of a sophisticated battery management system (BMS) is to estimate cells' state of charge (SOC) and state of health (SOH). Accurate SOH estimation requires aging detection as the battery pack operates. Therefore, nondestructive methods are favored in this case. This chapter proposes a nondestructive forensic pathology to perform online aging identification. A new 75Ah AGM VRLA battery is compared to a dead battery of the same make and model that was cycled over course of several months on an Arbin BT2000. Each battery consists of six chambers connected in series (see Fig. 3.1) containing eighteen cells in parallel. The test results are used to diagnose the dead chambers and their cause of the death. Since these cells in parallel were not differentiated in this study and their total voltage is the same as that of a single Pb-acid cell, they are referred as cells in this chapter.

In order for nondestructive forensic pathology of dead cells to work, each aging mechanism must have a unique signature that can be measured from the available sensors. In this work, individual cell voltage and pressure measurements are available and the current can be controlled to completely charge/discharge, pulse charge/discharge, and sinusoidally charge/discharge for EIS. These are considered to be nondestructive measurements because the access terminals and pressure ports could be built into the

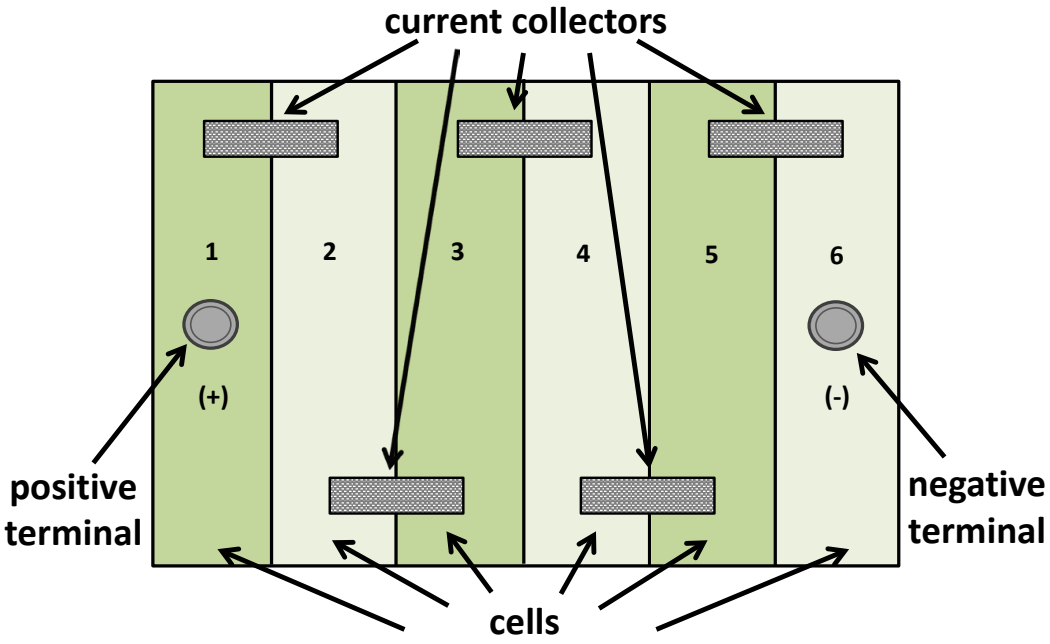

Figure 3.1. VRLA Battery Configuration: Six cells in chambers 1 - 6 are individually sealed and connected in series through current collectors.

battery. Voltage and pressure sensors are attached during the autopsy to make the desired measurements. The results of this autopsy are then used to revive the battery, adjust the BMS utilization, or direct recycling efforts.

3.2 Experimental Procedure

3.2.1 Battery Cycling

The dead battery was cycled on an Arbin BT2000 for 31,560 cycles using a duty cycle representative of an electric locomotive operating an 8 hour shift in a switchyard. The duty cycle consisted of 80 small pulse discharge/charge cycles and a constant-current-constant-voltage (CC-CV) charge at the end of the shift. The battery was declared dead when the capacity fell to approximately half of its initial value.

3.2.2 Full Charge/Discharge and Pulse Train Testing

The new and dead batteries were fully charged and discharged using an AE Techron

LVC 5050 linear amplifier controlled by dSPACE.

For pulse train testing, each battery was initially discharged to 70% SOC and then subjected to a charge-discharge cycle for 30 minutes. The pressure response was minimal during these tests so only the voltage data was collected.

The measured capacities of the new and dead batteries are 70-75Ah and 36-43Ah, respectively. During full charge/discharge testing, the batteries were discharged from 100% SOC until a cutoff voltage of 10V was reached. The batteries were rested for at least 24 hours and then charged until a cutoff voltage of 15V was reached. Note that the current flowing through the new and dead batteries during testing were not equal, because of the noted difference in charge capacity.

Five rods were threaded to a depth of approximately 0.5 inches into the top of each cell current collector so that individual cell voltages could be measured during testing. Holes were drilled into each individual cell and tubes were inserted and sealed to enable pressure measurement (See Fig. 3.2). Omega PX309 pressure sensors were attached to the tubing and electrically connected to dSPACE to measure the cell pressures. All the cell pressures were zeroed so that the discrepancy in gas generation inside each cell is only due to the health condition of the cells.

3.2.3 Impedance Testing

Battery impedance was measured using the Frequency Response Analyzer (FRA) method, for which a small sinusoidal battery voltage and the current response are the input and output of the system, respectively [92]. The small cell voltage signal passes through an external circuit that removes the DC offset (i.e. the battery OCV) and amplifies the remaining AC signal. A DAQ system then reads the level-shifted and amplified voltage signal. The external circuitry ensures that the voltage signal spans the full range of the analog to digital input channel. This reduces quantization error, which improves signal quality and reduces noise in EIS plots.

Since battery impedance is very small (on the order of $m\Omega$), only a 10mV battery voltage signal was necessary for producing a substantial current response. The frequency of the battery voltage signal was held constant for five cycles at logarithmically spaced points between 0.01Hz to 100Hz. A FFT was used to analyze the voltage and current signals separately. Impedance was then calculated from amplitude and phase

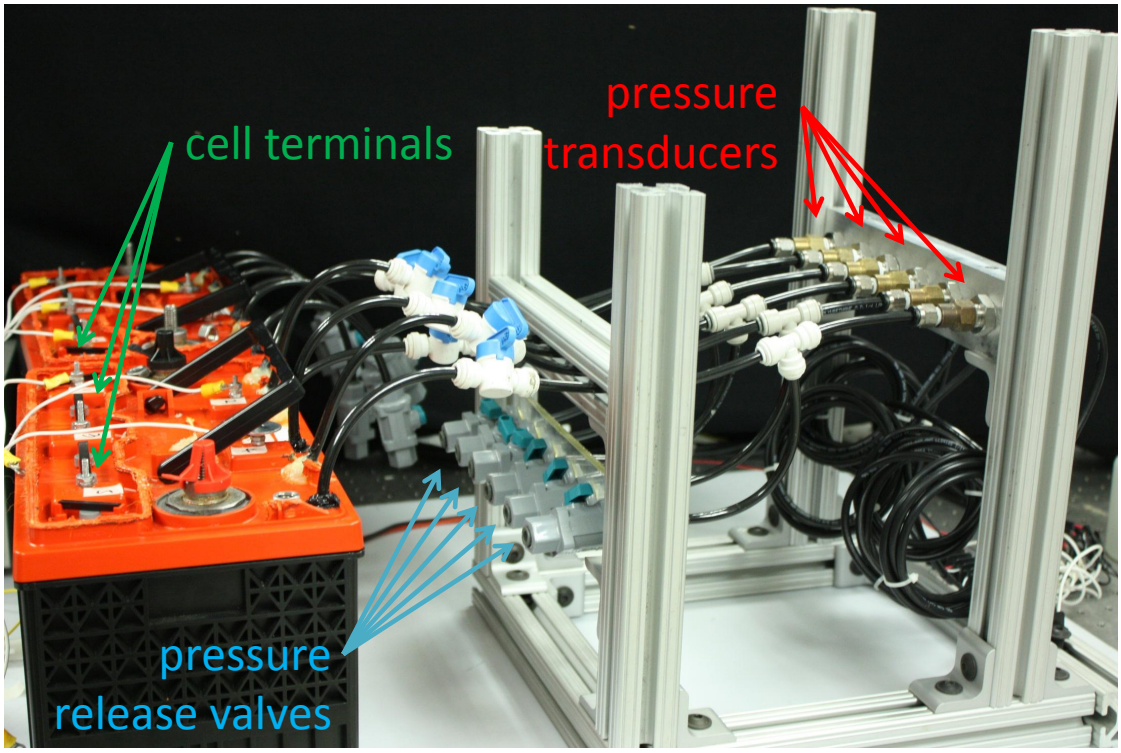

Figure 3.2. Photograph of the experimental setup.

data. The test circuit was validated using a Solartron SI1255B Frequency Response Analyzer.

3.3 Results and Discussion

3.3.1 Full Charge/Discharge Testing

Figures 3.3 and 3.4 show the experimental results from full charge/discharge of the new and dead battery, respectively. The left column of each figure is for charge and the right column is for discharge. The charge starts from a fully discharged state at 12.5V and 11.5V for the new and dead batteries, respectively. The voltage immediately jumps at the onset of charge current due to the ohmic resistance and then slowly climbs to the cutoff voltage of 15V. Current rates of 7A and 5A for the new and dead batteries were chosen to be approximately C/10. The new and dead battery reach full charge after 10.2 hrs and 9.1 hrs, respectively, indicating charge rates close to C/10. The total charge

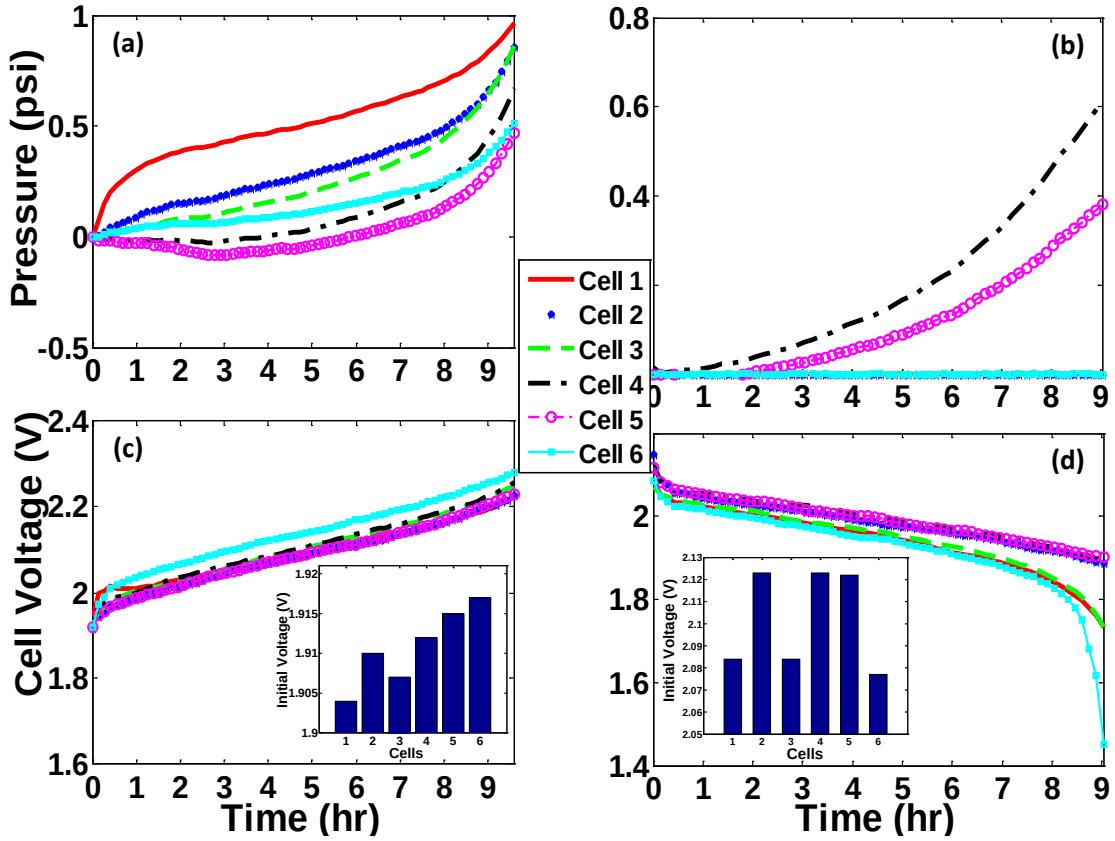

Figure 3.3. Charge/discharge of the new battery: (a) Cell pressure during charge; (b) Cell pressure during discharge; (c) Cell voltage during charge with inset showing initial distribution; and (d) Cell voltage during discharge with inset showing initial distribution.

transferred to the new and dead batteries is 70Ah and 40Ah, respectively.

Other than the voltage shift due to increased ohmic resistance, the new and dead battery voltage curves look similar, especially at low state of charge (SOC). At higher SOC, however, the dead battery voltage curve loses the smooth quality of the new battery and has a nonuniform growth in slope.

The cause for this nonuniformity in the dead battery voltage curve becomes clear from the cell voltage and pressure measurements in Figs. 3.4(a) and 3.4(c), respectively. While there is almost no pressure generated in the new battery (See Fig. 3.3(a)), the dead battery shows significant pressure rise due to gassing in several cells. In fact, the inset of Fig. 3.4(a) shows the pressure in Cell #5 plateauing after 8.8 hrs, indicating that the cell vented excess pressure though a factory installed safety valve. The inset in Figure 3.4(c) shows that the growth in voltage is coordinated with the increase in pressure so the cells with demonstrated water loss (Cells #2, #5, #6) are directly responsible for the growth

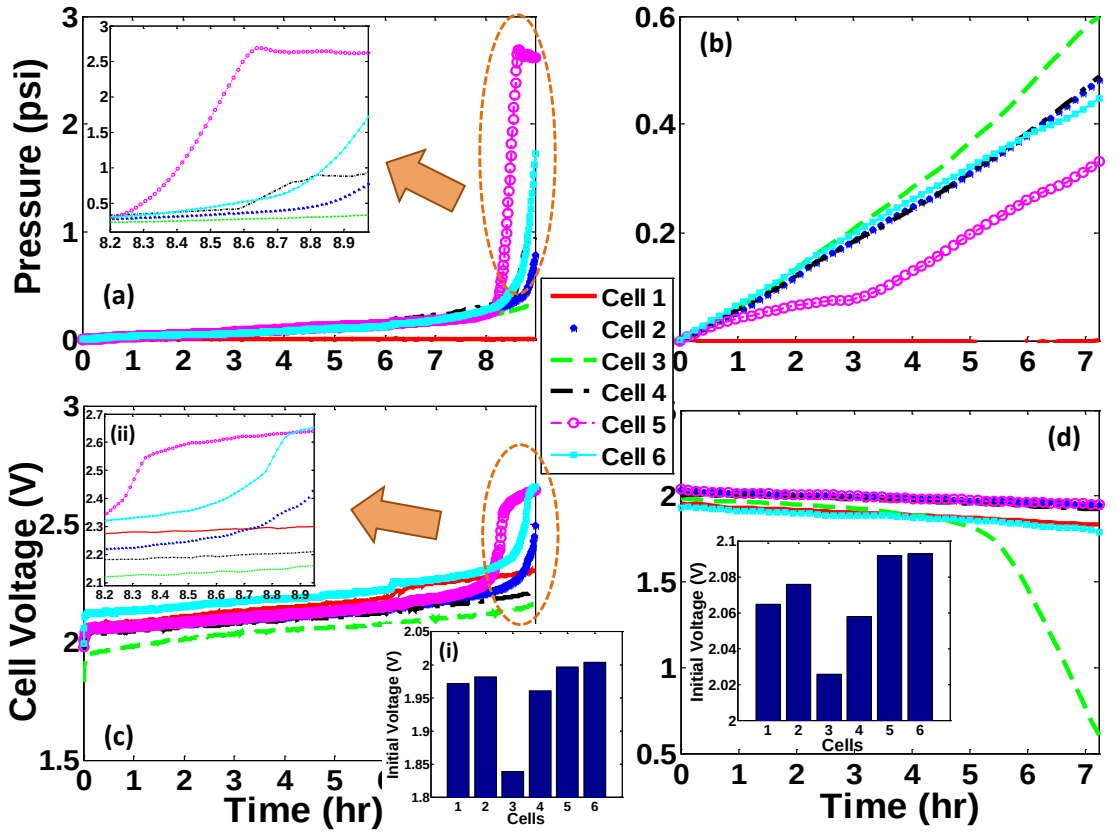

Figure 3.4. Charge/discharge of the dead battery: (a) Cell pressure during charge with inset showing pressure build-up; (b) Cell pressure during discharge; (c) Cell voltage during charge with insets showing (i) the initial distribution and (ii) voltage change at the end of charge; and (d) Cell voltage during discharge with inset showing initial distribution.

in voltage and associated reduction in capacity.

The hypothesis that water loss is responsible for the death of Cells #2, #5, and #6 is buttressed by the uneven voltage distribution in the cells prior to charge. Voltage is directly related to acid concentration [62] and acid concentration increases with water loss. The three cells with gassing also have the highest initial voltage as shown by the inset plot in Fig. 3.4(c). Contrast the uneven initial voltage distribution of the dead battery with the uniform distribution for the new battery in Fig. 3.3(c).

The discharge starts from a fully charged state at 12.61V and 12.41V for the new and dead batteries, respectively. The voltage immediately jumps at the onset of discharge current due to the ohmic resistance and then slowly decreases to the cutoff voltage of 9.5V. At the approximately C/10 current rate, the new and dead battery are fully discharged after 9.1 hrs and 7.2 hrs, respectively. The total charge delivered by the new

and dead batteries is 70Ah and 40Ah, respectively.

In addition to the negative offset due to increased ohmic resistance, the dead battery discharge curve has a shorter plateau and more rapidly drops off with decreasing SOC. As expected, gassing does not play a significant role. The cell voltage plot in Fig. 3.4(d) shows that Cell #3 experiences a rapid decrease in voltage after five hours of discharge. The other five cells have relatively normal discharge curves and could provide significantly more charge if not for the reduction in battery voltage caused by Cell #3.

The rapid voltage drop in Cell #3 during discharge is indicative of sulphation. Sulphation reduces the effective active area and acid concentration, both of which decrease capacity. Cell #3 has the lowest initial voltage (see inset in Fig. 3.4(d)), indicating low acid concentration. Cell #3 also did not show symptoms of gassing during charge which would be indicative of corrosion, another possible degradation mechanism.

3.3.2 Pulse Train Testing

Figures 3.3.2 and 3.3.2 show the response of the new and aged batteries at 50% SOC to a current pulse train. The distribution of the new and aged cell voltages are dramatically different. The spread of voltages in the aged battery implies substantial differences in the states of health of each cell. Each cell of the new battery, on the other hand, shows a nearly identical dynamic response to the pulse train, suggesting that the variance in cell capacity and health is minimal. Figures 3.3.2 and 3.3.2 also show that the initial response of each cell (i.e. the large voltage jump at the start of the first current pulse) in the aged battery was much larger than the initial response of each cell in the new battery. This suggests that the aged battery has significantly larger ohmic resistance. Furthermore, the time constants of the cells within the aged battery vary considerably, which indicates differences in capacitance.

3.3.3 Impedance Testing

Figures 3.3.3 and 3.3.3 show the EIS results. Like the pulse train data, the distribution among the aged cells is much more spread out than that of the new cells. The individual cell EIS plots for the new battery are fairly uniform, showing the 45° tail at low frequency, a mid frequency arc associated with double layer capacitance, and high frequency inductance. The EIS plots of the aged battery are more distributed, show-

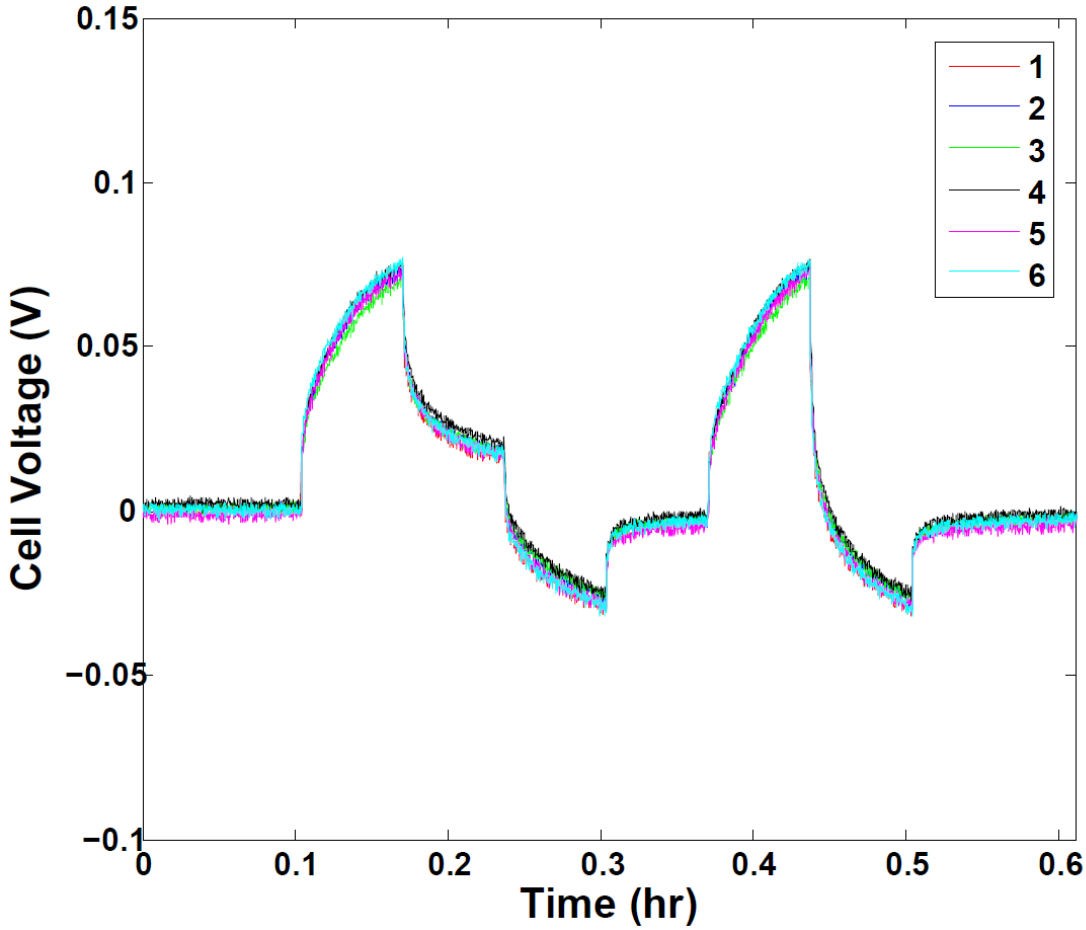

Figure 3.5. Pulse train voltage response of the new battery. The OCV of each cell was subtracted from each curve to facilitate comparisons between cells.

ing widely ranging resistance and capacitance. Cell #6 of the aged battery exhibits the largest ohmic resistance, which agrees with the pulse train data; however, no other correlations based on resistance data can be drawn between the EIS and pulse train data.

The radius of curvature in the high frequency impedance region was measured to determine the relative capacitance of each cell in the aged battery. Table 3.1 lists the cells in order of increasing capacitance, with 1 corresponding to the cell with the smallest capacitance and 6 to the largest (capacitance is inversely proportional to impedance).

Besides the increase in overall resistance due to aging, the correlation between the observed EIS spectra and specific degradation mechanisms is unclear, however, and warrants further study.

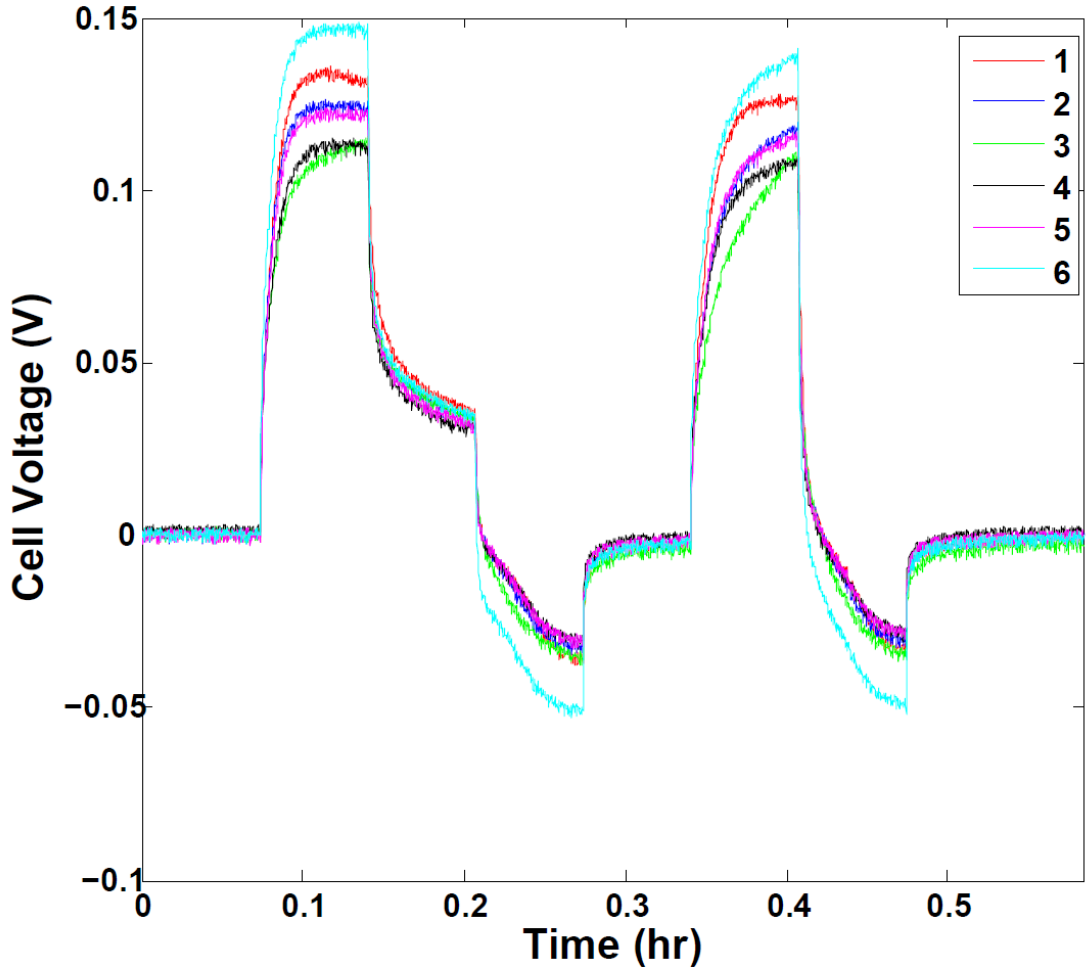

Figure 3.6. Pulse train voltage response of the old battery. The OCV of each cell was subtracted from each curve to facilitate comparisons between cells.

Table 3.1. The radius of curvature of each cell within the aged battery.

Cell	Red	Blue	Green	Black	Maroon	Cyan
Radii ($m\Omega$)	0.7591	0.7693	0.7985	0.8858	0.6459	0.6892
Ranking	4	3	2	1	6	5

3.3.4 Aging Diagnosis

3.3.4.1 Hard sulfation

Given that Cell #3 did not suffer severe gassing during charge (no pressure and volt-

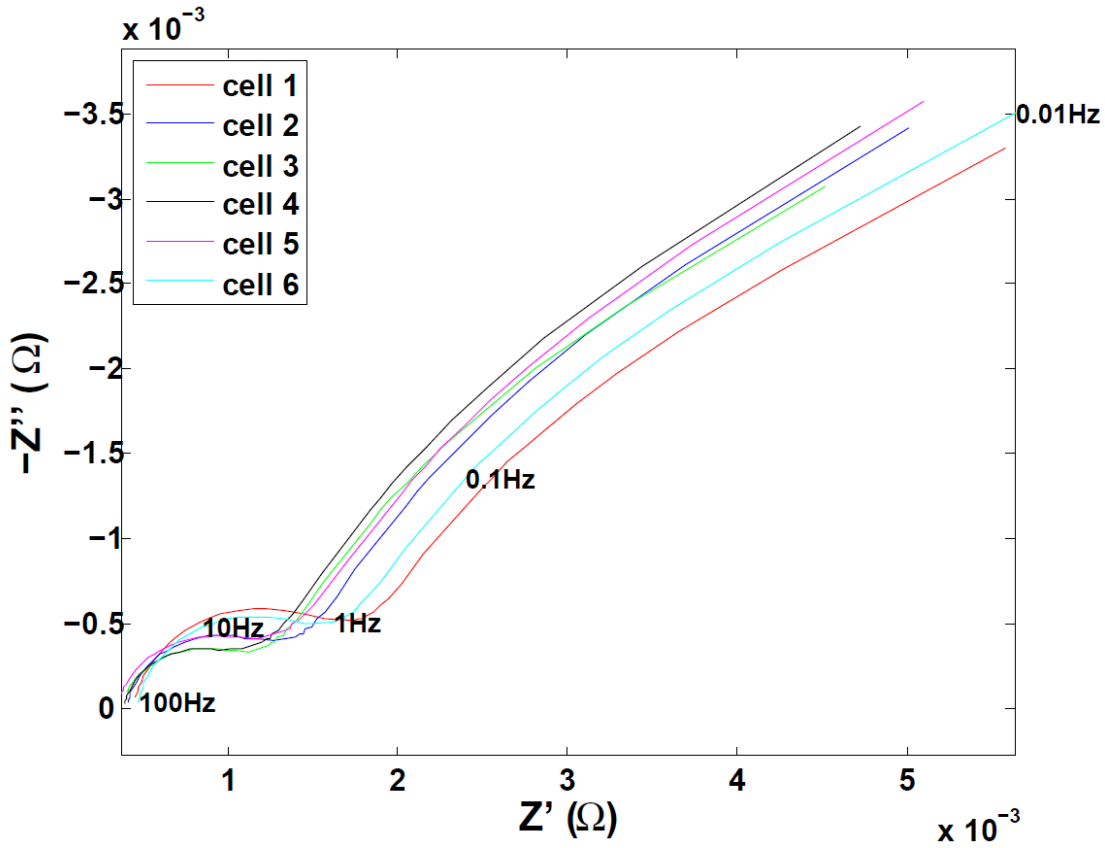

Figure 3.7. EIS plots of the new battery from 0.01Hz to 100Hz

age rise shown in Figs. 3.4(a) and (c)), Cell #3 is possibly dead from hard sulfation or corrosion. Irreversible hard sulfation refers to the hard crystallization of lead sulfate via recrystallization process, which causes part of the products of discharge can not be reused and decomposed in charge and results in loss of active material and thus, capacity. When hard sulfation occurs, the effective specific surface area will be reduced and the internal acid concentration will be lowered. Corrosion is a process that the electrode grid is oxidized and the layer of the oxidation products prevent the current flux to go through, resulting in impedance rise, but no direct effect on the internal acid concentration. For Pb-acid batteries, the internal acid concentration is reflected by the open circuit potential (OCV) [93]. As shown in Fig. 3.9, the OCV is a monotonically increase function of the acid concentration. Therefore, the lower initial OCV of Cell #3 in Fig. 3.4(c)(i) is indicative of hard sulfation. The combination of pulses of charge/discharge and long-term parasitic load in the duty cycles which aged the battery, provides friendly environment

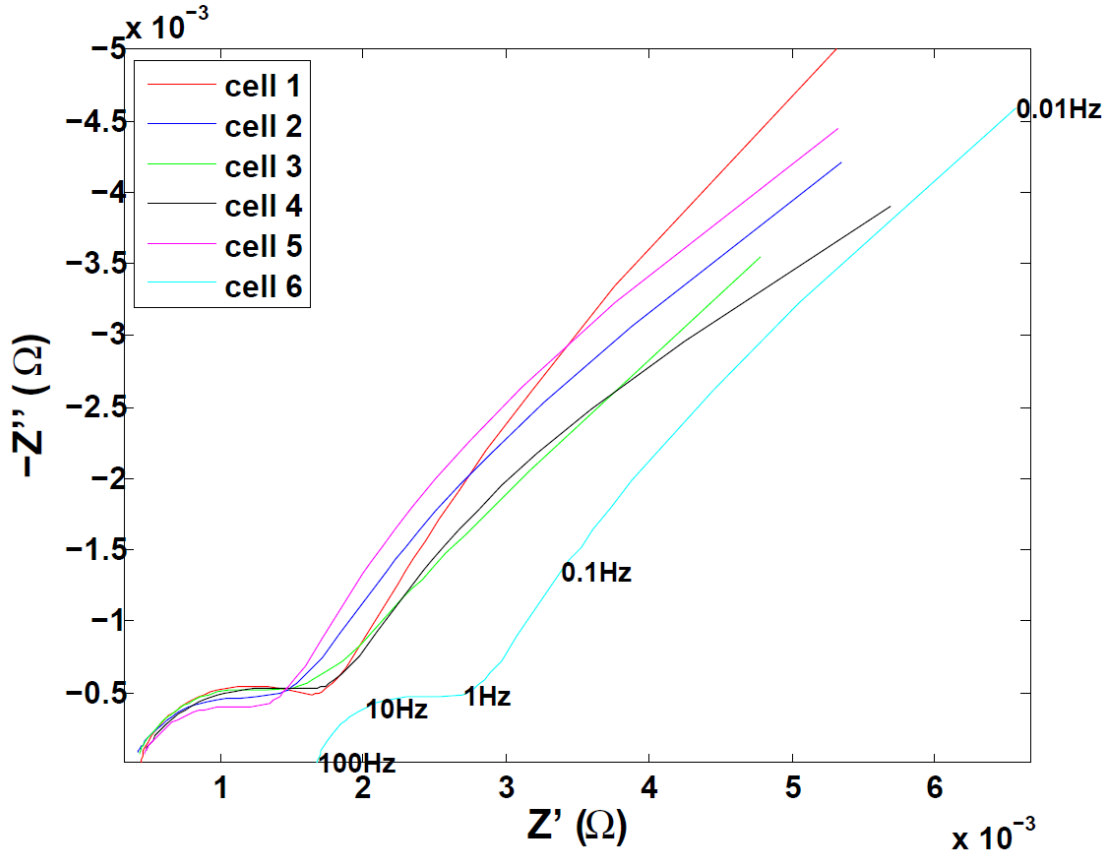

Figure 3.8. EIS plots of the dead battery from 0.01Hz to 100Hz

for hard sulfation. This is also indicative of hard sulfation as the prominent cause of death of Cell #3.

3.3.4.2 Water loss

Cells #2, #5, and #6 exhibit early voltage and pressure rise shown in Figure 3.4(c), implying that water loss is directly responsible for the growth in voltage and associated reduction in capacity. The three cells with gassing also have the highest initial voltage as shown by the inset plot in Fig. 3.4(c). This also indicates that the three cells are suffering from dehydration because voltage is directly related to acid concentration [62] and acid concentration increases with water loss.

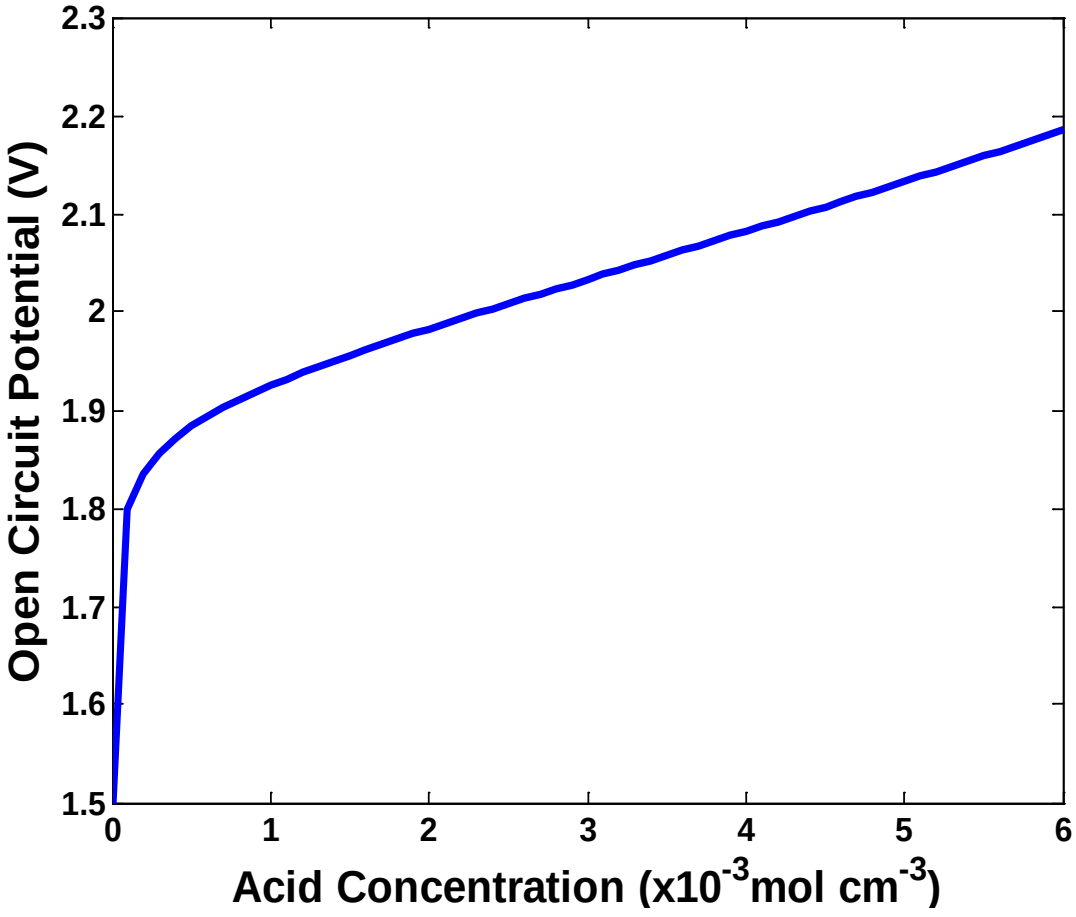

Figure 3.9. Open circuit potential as a monotonically increase function of acid concentration.

3.4 Conclusions

The causes of death for VRLA batteries can be determined from a full charge/discharge cycle while monitoring individual cell pressures and voltages. In this study, Cells #2, #5, and #6 of a dead VRLA battery became overcharged and started gassing earlier than other cells during charge so the cause of death for these cells was dehydration. Cell #3 displayed a sharp, voltage drop during discharge, indicating death by sulfation.

The pressure rise associated with gassing was accompanied by a sharp rise in cell voltages. This suggests that individual cell pressure sensors equipment might not be necessary to observe gassing.

The pathological capabilities of EIS and short duration pulse charge/discharge is not clear. The pulse train response and EIS curves are different for the dead and new bat-

teries and cells but the correlations are not fully understood. On-board SOH monitoring is more practical if the real-time data from everyday use can be used to determine the battery capacity. This motivates further study into the predictive capability of pulse train and EIS testing.

Chapter 4

Remediation of Sulfation in Lead-Acid Batteries Using Cell Voltage and Pressure Sensing

4.1 Introduction

Lead-acid is the most widely used chemistry for batteries in stationary and hybrid applications, with the majority consisting of a valve-regulated lead-acid (VRLA) design. The most common damage mechanisms for a VRLA battery include [2, 3, 4, 5, 6, 7, 8, 9, 10]:

- Positive electrode corrosion
- Irreversible hard sulfation
- Water loss/dry-out
- Positive electrode softening and shedding
- Electrolyte stratification
- Internal short-circuit
- Mechanical damage (current connector failure, case damage, *etc.*)
- Others (passive lead oxide film, thermal runaway, *etc.*)

They are often not independent from each other and multiple mechanisms can occur in one cell. VRLA batteries are designed to minimize these effects as much as possible but the operating environment, cell-to-cell and battery-to-battery manufacturing variations, and use can cause different degradation mechanisms to dominate capacity loss and/or impedance rise. With the ability to determine in real time the predominant degradation for each cell, battery management system (BMS) can predict the cell SOH accurately, adjust cell use accordingly and balance cells with respect to their health conditions so as to extend service life of the battery pack.

For system/control engineers, a practically optimal BMS design will have a very accurate yet computationally cheap baseline model, as fewer as possible sensors, and sophisticated controllers. The controllers use the model and the sensor measurements (e.g., current, voltage, temperature, etc.) to calculate/estimate the other states (e.g., state of charge, state of health), predict the future performance based on the external power demand (e.g., how much power and how long the pack can provide it, how much life will be left and when maintenance will be needed) so that the BMS can adjust the cells use, protect the cells from thermal runaway and other safety issues, balance the cells according to not only SOC but also SOH, maintain their service lives, and optimize the overall pack performance.

There are several challenges here. First, to have accurate estimation of SOC/SOH requires an underlying model including the predominant aging mechanisms but usually such a comprehensive model is complicated and computationally so expensive that it cannot be handled by a small on-board microprocessor. Second, more sensors make it easier for system engineers to design high performance controllers. Given the limited space within the pack and the large number of cells, it is typically not practical to have the detailed measurements that can be made in a laboratory setting. Third, in industrial applications, many manufacturing parameters such as acid concentration, saturation, and grid composition, needed for controllers design are not available due to IP agreements or contracts which drives engineers to add extra on-board sensing or use estimators based models.

To perform real-time aging diagnosis in vehicles/locomotives, nondestructive techniques with as few sensors as possible are favored because switching out an aged cell from a pack and examining it using laboratory tools/methods costs a lot of labor and system downtime and can only be performed at very low frequency. Many studies that

investigate aging in VRLAs use destructive techniques to identify degradation mechanisms. Studying a dissected battery using a scanning electron microscope and chemical analysis provides a physical understanding of aging processes, such as hard lead sulfate formation [24, 25, 26] or corrosion layer growth [27, 28]. Although these invasive techniques provide detailed information about the SOH of the battery, they can only be used posthumously. With nondestructive monitoring techniques, on the other hand, the BMS can diagnosis aging and implement unique charging strategies to extend service life.

Nondestructive techniques are also essential for accurate SOH estimation in real time. Most nondestructive techniques for on-line SOC/SOH estimation are model-based [29, 30, 31, 32] and require accurate model fitting. The techniques developed so far, however, do not specify the degradation mechanisms that cause battery aging or use models which requires **a priori** knowledge of major degradation. Trying to include every possible failure mode in the model can result in computationally-expensive models that on-board BMS cannot handle. Analyzing data from nondestructive tests may offer an alternative to a model-based approach for SOH estimation. Nondestructive tests that require only current and voltage data include: full change/discharge cycling, pulse train, and Electrochemical Impedance Spectroscopy (EIS). In particular, EIS is influenced by SOC [33] and the shape of the impedance curve is often related to degradation mechanisms, such as gassing at a single electrode [34].

In this study, individual cell voltage and pressure measurements are available and the current can be controlled to completely charge/discharge, pulse train, and sinusoidally charge/discharge for EIS. These are considered to be nondestructive measurements because the access terminals and pressure ports could be integrated relatively easily into the battery. Voltage and pressure sensors are attached during the autopsy to make the desired measurements. The results of this autopsy can then be used to revive the battery, adjust the BMS utilization, or direct recycling efforts.

The ability to not only identify degraded cells within a VRLA battery but also to restore their capacity could dramatically prolong battery life. Typical VRLA batteries have multiple cells connected in series. As the battery ages, the cell capacities diverge and the cell with the lowest capacity limits the overall battery capacity. A BMS that identifies sulfated cells and has the ability to desulfate those cells could increase the overall capacity of an aged battery.

Negative plate sulfation is one of the most prominent aging mechanisms for VRLA

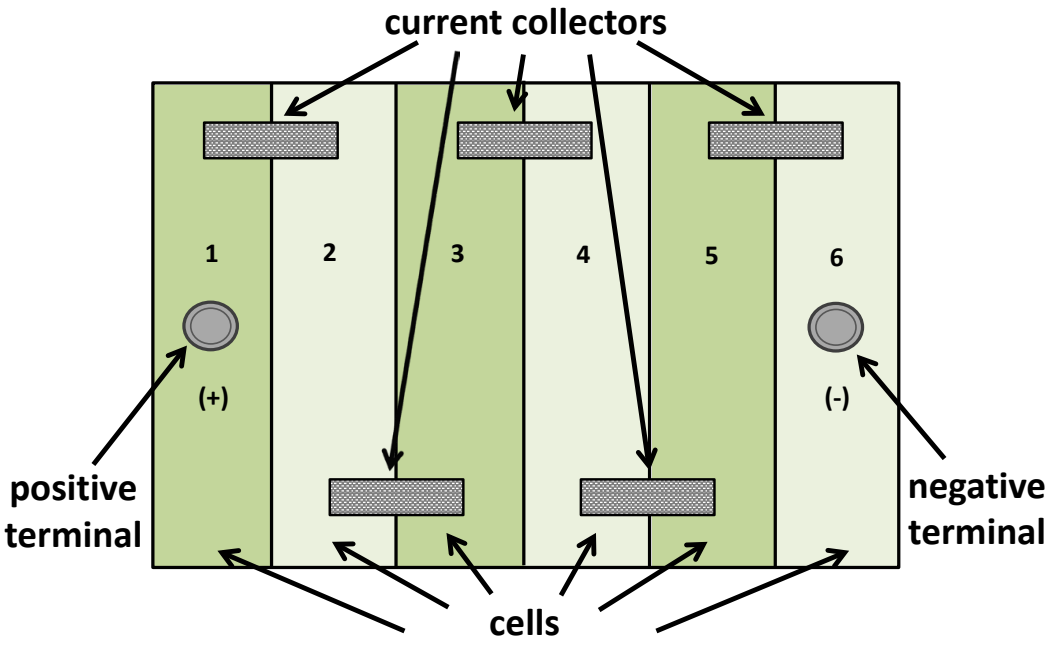

Figure 4.1. VRLA Battery Configuration: 6 cells in chambers 1 - 6 are individually sealed and connected in series through current collectors

batteries and is especially common in hybrid vehicle applications [35, 36]. Gibson *et al.* conclude that high rate charging and discharging at partial states of charge leads to the progressive accumulation of lead sulfate on the negative plates of VRLA batteries. Gibson *et al.* [24], Yamaguchi *et al.* [25], and Takehara [26] have thoroughly studied and developed an understanding of the structure and recrystallization of hard crystalline lead sulfate. Lead dioxide and lead are discharged in sulfuric acid to form lead sulfate and water. The reaction reverses during charge, lead sulfate being decomposed to produce lead dioxide and lead. Both reactions take place via dissolution-precipitation processes. During discharge, electrons are transferred to form lead ions then dissolved into the solution and supersaturation of Pb^{2+} may be achieved. After the nuclei are formed, $PbSO_4$ precipitates and the size of the $PbSO_4$ crystals depends on the concentration of sulfuric acid and the current density. During charge, lead sulfate dissolves into Pb^{2+} and SO_4^{2-}. Then electron transfer occurs on the electrode grid and the ions are oxidized/reduced to PbO_2 and Pb. This process is greatly affected by the current density, the diffusion rate, the crystal size and the solubility of $PbSO_4$. In addition, the reaction area changes

by several orders of magnitude during the reactions. The lead sulfate crystals formed through electrochemical process have rough surfaces with high porosity and activity. Therefore, the lead ions may dissolve from the crystals and re-crystallize back, a process known as Ostwald ripening. Crystals formed in recrystallization have finer surfaces with higher density and lower activity. Hence, these lead sulfate crystals have less reaction area and are much more difficult to be converted back during charge. Approaches to reducing sulfation include high-frequency pulse charging [49, 50], using carbon additives [43, 44] and expander components [9, 45, 46] and replacing the negative electrode with carbon [35, 47, 48].

Desulfation can restore some of the capacity lost to sulfation. Most commercial battery chargers/desulfators conduct desulfation using a technique known as "pulse conditioning", which consists of applying short, high-current pulses to a cell [94, 95, 96, 97]. Lam *et al.* found pulsed charging to be a promising approach towards enhancing the cycle life of Pb-Sb and Pb-Ca-Sn cells [51]. that Keyser *et al.* proposed to use high finishing currents and current-interrupt charging algorithm to minimize sulfation and gassing during cycling [52]. Hydrogen and oxygen production associated with the electrolysis of water molecules at high states of charge, however, can lead to water loss, another aging mechanism that decreases cell capacity. Desulfation techniques must minimize water loss to effectively recover lost capacity.

Electrolyte stratification is another common failure mode for lead-acid batteries. It is considered to be most severe in flooded batteries, much less prominent in AGM batteries and not significant at all in gelled batteries due to the immobilized electrolyte [37, 38, 39]. Electrolyte stratification causes a vertical distribution of acid and promotes the formation of irreversible lead sulfate in the lower parts of the electrodes [40, 41]. Electrolyte stratification can be mitigated by overcharging and gassing [10, 39, 40, 42].

Batteries may degrade due to multiple mechanisms at different speed, even cells in one pack, because of the variations in manufacturing, usage and working conditions, etc. The goal of the work in Chapter 4 is to develop real-time aging diagnostic techniques that can be integrated into battery management systems (BMS) to improve online state of health (SOH) estimation accuracy. Therefore, the methods should be nondestructive/non-intrusive (without opening the pack and cells), simple and cheap (use as few sensors, electronics, and supporting hardware as possible). There are electrochemical laboratory methods (such as using SEM and AFM) that are simple and

provide conclusive results in determining cell degradation. These are not practical for online/real-time usage because they require special equipment, skilled technicians and opening the battery which results in a lot of labor cost and system downtime. This motivates the approaches taken in this work to find other ways to determine the most likely degradation mechanisms in lead-acid batteries that can be implemented online in real-time at low cost.

In this study, a dead AGM VRLA battery is compared to a new battery of the same make and model. The dead battery was cycled over the course of several months on an Arbin BT2000 using a switchyard cycle. Each battery consists of six chambers connected in series (see Fig. 4.1) containing eighteen cells in parallel. The test results are used to diagnose the dead chambers and their cause of death. Since the 18 cells in parallel in each chamber were not differentiated in this study and their total voltage is the same as that of a single Pb-acid cell, they are referred to as cells here. After identifying the dominant aging mechanisms, a charging algorithm is designed and implemented to revive one of the dead cells in order to increase the overall capacity of the battery.

During the charge, individual cell voltage and pressure measurements are available and the current can be controlled to completely charge/discharge, pulse train, and sinusoidally charge/discharge for EIS. These are considered to be nondestructive measurements because the access terminals and pressure ports could be integrated relatively easily into the battery. Voltage and pressure sensors are attached during the autopsy to make the desired measurements. The results of this autopsy can then be used to revive the battery, adjust the BMS utilization, or direct recycling efforts.

4.2 Nondestructive Aging Diagnosis

As discribed in Chapter 3, an aged battery was cycled on an Arbin BT2000 for 31,560 cycles using a duty cycle representative of an electric locomotive operating an 8-hour shift in a switchyard. The duty cycle was a low-rate partial-state-of-charge cycle and consisted of 80 small pulse discharge/charge cycles and a constant-current-constant-voltage (CC-CV) charge at the end of the shift. The battery was declared dead when the capacity fell to approximately half of its initial value. In addition to the aged battery, a new battery was procured and used as a control. The measured capacities of the new and dead batteries were 70Ah and 40Ah, respectively. An AE Techron LVC 5050 linear

amplifier, dSPACE DAQ system, and additional custom-built hardware were integrated together and used to conduct cycling, pulse-train, and EIS testing (See Figs. 4.3 and 4.2).

Figure 4.2. A picture of the hardware used to conduct testing.

The cell voltage plot in Fig. 4.4(e) shows that Cell #3 experiences a rapid decrease in voltage after 50% depth of discharge (DOD). The other five cells have relatively normal discharge curves and could provide significantly more charge if not for the reduction in battery voltage caused by Cell #3. Therefore, Cell #3 had the lowest capacity which also dictated the capacity of the battery.

Given that Cell #3 did not suffer severe gassing during charge (no pressure and voltage rise shown in Figs. 4.5(b) and (e)), Cell #3 is possibly dead from hard sulfation or corrosion. Irreversible hard sulfation refers to the hard crystallization of lead sulfate via recrystallization process, which causes part of the products of discharge can not be reused and decomposed in charge and results in loss of active material and thus, capacity. When hard sulfation occurs, the effective specific surface area will be reduced and the internal acid concentration will be lowered. Corrosion is a process that the electrode grid is oxidized and the layer of the oxidation products prevent the current flux to go through, resulting in impedance rise, but no direct effect on the internal acid concentration. For

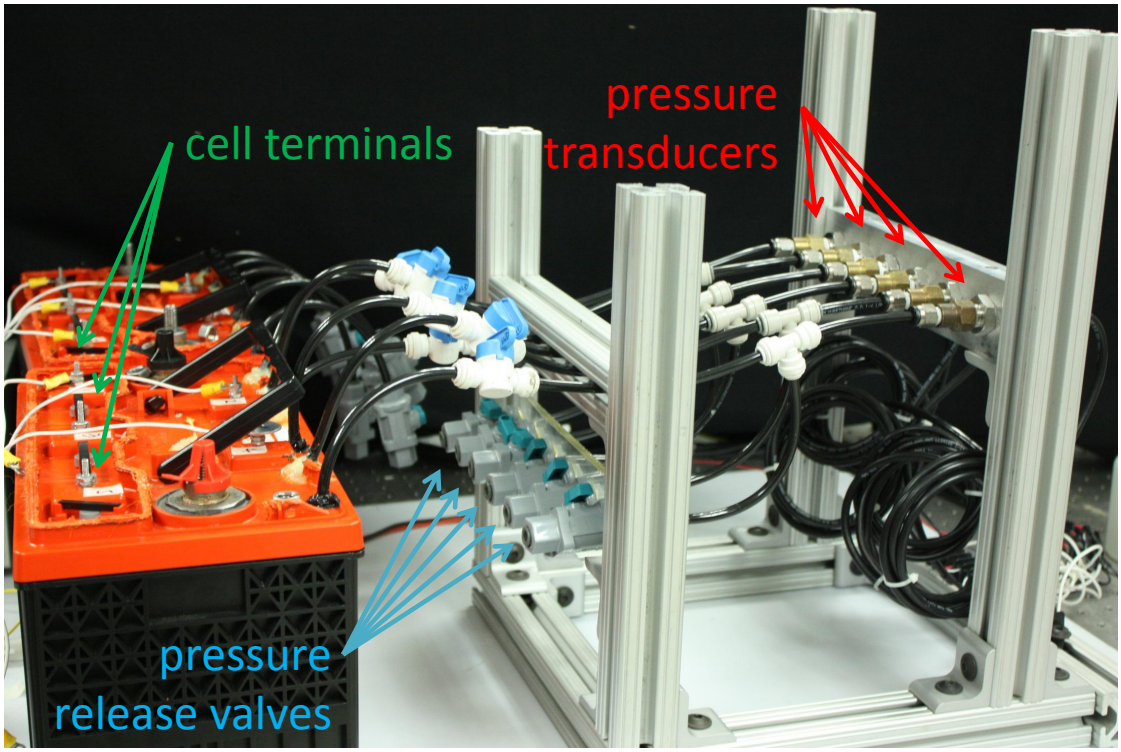

Figure 4.3. Photograph of the experimental setup

Pb-acid batteries, the internal acid concentration is reflected by the open circuit potential (OCV) [93]. Therefore, the lower initial OCV of Cell #3 in Fig. 4.4(g) is indicative of hard sulfation. The combination of pulses of charge/discharge and long-term parasitic load in the duty cycles which aged the battery, provides friendly environment for hard sulfation. This is also indicative of hard sulfation as the prominent cause of death of Cell #3.

4.3 Desulfation and Capacity Recovery

The test results identify sulfation in one cell and water loss in three cells as probable degradation mechanisms. The capacity of the dead VRLA battery was limited largely by sulfation in one of six cells. A desulfation/charging algorithm is developed to increase the capacity of the sulfated cell without causing water loss. The algorithm charges only

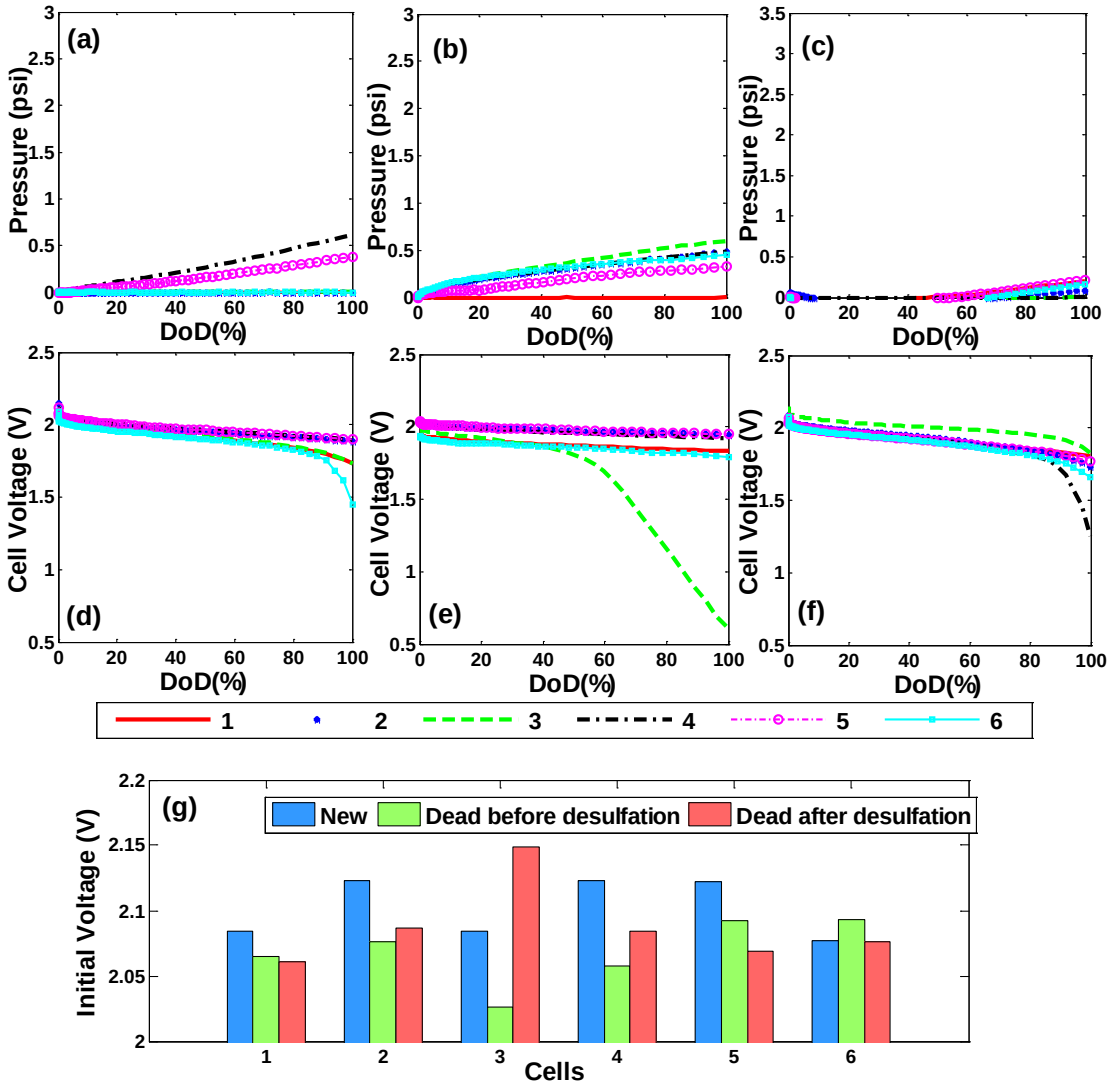

Figure 4.4. Discharge of the new and the dead batteries: (a) Cell pressure of the new battery; (b) Cell pressure of the dead battery before desulfation; (c) Cell pressure of the dead battery after desulfation; (d) Cell voltage of the new battery; (e) Cell voltage of the dead battery before desulfation; (f) Cell voltage of the dead battery after desulfation; (g) Initial cell voltages of the new and the dead batteries before and after desulfation

the sulfated cell while using cell pressure feedback control to minimize gas generation. Successful desulfation validates the diagnosis of sulfation in Cell #3 as the primary aging mechanism because corrosion is irreversible.

4.3.0.3 Gas Evolution During Overcharge

Optimal desulfation requires charging a cell with as much current as possible without crossing the voltage threshold that induces excessive gassing. The primary reaction in the positive electrode of a Pb-acid battery is

$$\mathrm{PbSO_4 + 2H_2O \underset{\text{discharge}}{\overset{\text{charge}}{\rightleftharpoons}} PbO_2 + HSO_4^- + 3H^+ + 2e^-}, \tag{4.1}$$

where the standard electrode potential $E^o_{PbO_2/PbSO_4} = 1.636V$ vs. SHE. The primary reaction in the negative electrode is

$$\mathrm{PbSO_4 + H^+ + 2e^- \underset{\text{discharge}}{\overset{\text{charge}}{\rightleftharpoons}} Pb + HSO_4^-}, \tag{4.2}$$

where $E^o_{Pb/PbSO_4} = -0.295V$ vs. SHE. The overall cell potential is $E^o_{cell} = E^o_{PbO_2/PbSO_4} - E^o_{Pb/PbSO_4} = 1.931$, but the actual cell potential E_{cell} depends on acid concentration, according to the Nernst Equation [1],

$$E = E^o_{cell} + \frac{RT}{nF} ln \left(\frac{a_{H^+} \cdot a_{HSO_4^-}}{a_{H_2O}} \right), \tag{4.3}$$

where $R = 8.314 J/(K\,mol)$ is the universal gas constant, $F = 9.64810^{-4} C/mol$ is Faraday's constant, T is the temperature in degrees K, n is the number of moles of electrons transferred and a_{H_2O}, a_{H^+}, and $a_{HSO_4^-}$ are the reactant concentrations.

During charging, oxygen evolves at the positive electrode,

$$\mathrm{2H_2O \rightarrow O_2 + 4H^+ + 4e^-}, \tag{4.4}$$

at the water decomposition voltage $E^o_{O_2} = 1.23V$ vs. SHE and hydrogen recombines,

$$\mathrm{H_2 \rightarrow 2H^+ + 2e^-}. \tag{4.5}$$

Hydrogen also evolves at the negative electrode,

$$\mathrm{2H^+ + 2e^- \rightarrow H_2}, \tag{4.6}$$

at $E^o_{H_2} = 0V$ vs. SHE and oxygen recombines

$$O_2 + 4H + 4e^- \rightarrow 2H_2O. \tag{4.7}$$

Oxygen evolution occurs when the positive electrode potential is above $E^o_{O_2}$ and hydrogen evolution occurs when the negative electrode potential is below $E^o_{H_2}$. Similarly, oxygen and hydrogen recombination occur when the electrode potentials are below $E^o_{O_2}$ and above $E^o_{H_2}$, respectively. The electrode potentials of a Pb-acid battery exceed the gas production thresholds ($E^o_{Pb/PbSO_4} < E^o_{H_2}$ and $E^o_{PbO_2/PbSO_4} > E^o_{O_2}$), so hydrogen and oxygen continually evolve during charging. Thus, these secondary reactions are unavoidable [93] but the gas generation rates can be extremely small if the overpotential voltage is not too large. The gas evolution rate increases exponentially with voltage above and below $E^o_{O_2}$ and $E^o_{H_2}$, respectively.

Oxygen generated at the surface of the positive electrode passes through gas paths in the AGM separator to the negative electrode. Then, the oxygen dissolves in the electrolyte and is reduced at the lead surface to produce water. Finally, the water is transported to the positive electrode to close the oxygen cycle [10, 58, 59, 61]. The oxygen reduction efficiency relies heavily on the saturation level of the separator because a decrease in the saturation level leads to an increase in the void space in the separator [50]. Hence, when a VRLA battery ages, the saturation level is lowered due to multiple aging mechanisms and the oxygen cycle becomes more efficient. Similarly, hydrogen can be transported to the positive electrode, but the hydrogen recombination rate is very small due to poor kinetics that it can be neglected [98]. Therefore, no internal hydrogen cycle exists. When the cell is overcharged, gas evolution accelerates and excessive gas leaves the cell and if 100% SOC is reached, the gas being released will ultimately consist of hydrogen and oxygen with a ratio of 2:1.

4.3.1 Desulfation Charging Algorithm

The optimal desulfation/charging algorithm is to direct all the charging current to the primary reaction, decomposing lead sulfate, using as large a current as possible but still suppressing the side reaction, gassing the most. The desulfation charging algorithm starts with constant-current (CC) charge to 2.40V. At this point, the cell is close to full SOC. After that, the internal cell pressure, $P(t)$, is fed back to the con-

troller to see if the pressure generation rate is within the tolerable range ($\dot{P} \cong \dot{P}_D = 6.8948\,kPa/day\,(1psi/day)$). If the pressure rate is below the threshold value, the charging rate is increased. If the gassing process exceeds the pressure rate limit, meaning that too much current is going into a side reaction instead of recovering the cell capacity, the charging rate is decreased. In this way, the current used is as large as possible to convert sulfate but not gas to maximize the capacity recovered and the charge speed while minimizing gas generation. A PID controller ensures that the gassing pressure rate tracks $\dot{P}_D$. Conventional integral action is modified to account for the fact that the pressure within the cell cannot be decreased by discharge and the recombination and leaking rates that reduce pressure are very slow.

The objective of the desulfation control algorithm is to pump charge into the cells while minimizing water loss. Water loss is the number of moles of water that are converted to gas. Using the ideal gas law, the number of moles of gas produced is

$$n = \frac{\Delta PV}{RT} + n_{leak}, \tag{4.8}$$

where $\Delta P = P_{atm} + P_g - P_0$, V is the cell gas volume, R is the ideal gas constant, and T is temperature. The parameters R and V are constant and assumed to be constant, respectively. Atmospheric pressure P_{atm} and gauge pressure P_g change in time relative to the initial pressure P_0. The cell chambers are not entirely sealed so gas leaks out with the approximate dynamics

$$\dot{n}_{leak} = \lambda P_g, \tag{4.9}$$

where λ is an experimentally determined rate constant. Using the measured P_g, P_0, P_{atm}, and T and integrating Eq. (4.9), one can calculate and regulate the number of moles of gas produced using Eq. (4.8). For a sealed cell, if P_{atm} falls precipitously then P_g can rise and cause the cell to vent. After venting, P_0 is reset and desulfation continues.

4.3.2 Results and Discussions

The experimental tests in section 4.2 indicate that Cell #3 of the tested VRLA battery died of sulfation. To validate the test results and restore the capacity, Cell #3 is desulfated using the algorithm described in the previous section. Table 4.1

summarizes the desulfation test parameters. The four tests averaged 78.2 hrs and

Table 4.1. Desulfation test results

Trial	Duration (hrs)	Charge Acceptance	Charge Speed (Ah/hr)
1	75	88.10%	0.289
2	94	97.93%	0.167
3	72	93.92%	0.175
4	72	97.73%	0.180

had an average charging current of 0.2A. The low charge acceptance of the first test indicates the conversion of hard sulfate to acid. The other three tests had higher charge acceptance, suggesting that the available sulfate had mostly been converted in the first iteration.

The three plots in Figure 7 illustrated that the controller worked as expected. The two lines in Fig. 4.6(a) represented the allowable pressure generation and the actual pressure (both after compensated for temperature, atmosphere pressure and leaking). Figures 4.6(b) and (c) display the corresponding voltage and current. When started, the pressure generation rate was slower than the tolerance, thus the current was increased and the voltage rose accordingly. Until the pressure generation rate caught up the allowed rate, the current was oscillating around the 1.7A so was the voltage because the pressure generation rate was swinging around the limit. After 5 hrs to the end of the test, the pressure generation rate passed the limit and the current was therefore attenuated to about 20-50mA and the voltage was still oscillating around 2.25V. This was possible the voltage threshold at which the gassing process occurred at the allowed rate as shown in Fig. 4.6(a).

Figure 4.7 shows the measured cell capacity after each desulfation test. Over the course of four tests, the capacity increased from 39.9 Ah to 56 Ah, or a 41% increase in capacity. The first desulfation test showed the largest capacity gain of 11.6 Ah (29%). The second test yielded another 4 Ah (10%) increase in capacity. The small capacity drop after the third test is possibly due to measurement variation. Together, the third and fourth tests yielded only another 0.7 Ah (1.3%) increase in capacity. Further capacity changes were minimal, suggesting that other mechanisms, such as corrosion, may have become dominant. Alternatively, the lead sulfate crystals closest to the negative electrode may be harder than the outer layers, and therefore more difficult to break down.

Although the capacity of the sulfated cell increased by 41%, the final cell capacity of 56.3 Ah was far from the nominal capacity of 88 Ah.

The full charge/discharge test shown in Figs. 4.5(c), (f), and 4.4(c), (f) that the capacity of the battery increased 12 Ah (30%) from 40 Ah to 52.4 Ah. The increase in overall battery capacity is less than the increase observed in the sulfated cell alone, suggesting that a different cell may now be responsible for limiting the capacity of the battery. Figs. 4.4(e) and (f) show that the shape of cell #3's voltage discharge curve after desulfation is similar to the other cells and no longer dramatically decreases before the other cells, as was observed before desulfation. Figs. 4.5(g) and 4.4(g) show that the desulfated cell's initial voltage is higher during both charge and discharge. This change is due to the fact that desulfation has converted more lead sulfate back into lead, lead dioxide, and sulfuric acid, increasing the acid concentration. Both observations support the conclusion that that Cell #3 has been successfully desulfated. Figures 4.5(c) and (f) show that Cell #3 gases more easily after desulfation. The increase in acid concentration, and therefore cell voltage, may be responsible for causing for early gassing. A higher OCV during charging increases the overpotential inside the cell and promotes gassing.

4.4 Conclusions

A desulfation charging algorithm is implemented and proves that desulfation can partially reverse capacity loss, showing a 41% capacity increase in one cell of an aged VRLA battery and a 30% capacity increase overall. The results also validate the diagnosis of sulfation as an important aging mechanism, responsible for at least 33% of the capacity loss of this cell, or 25% of the capacity loss of the whole battery. The inability to restore the cell to its original capacity indicates that other aging mechanisms such as corrosion and water loss also contribute to aging. The tests show diminishing returns after 313 hrs of desulfation.

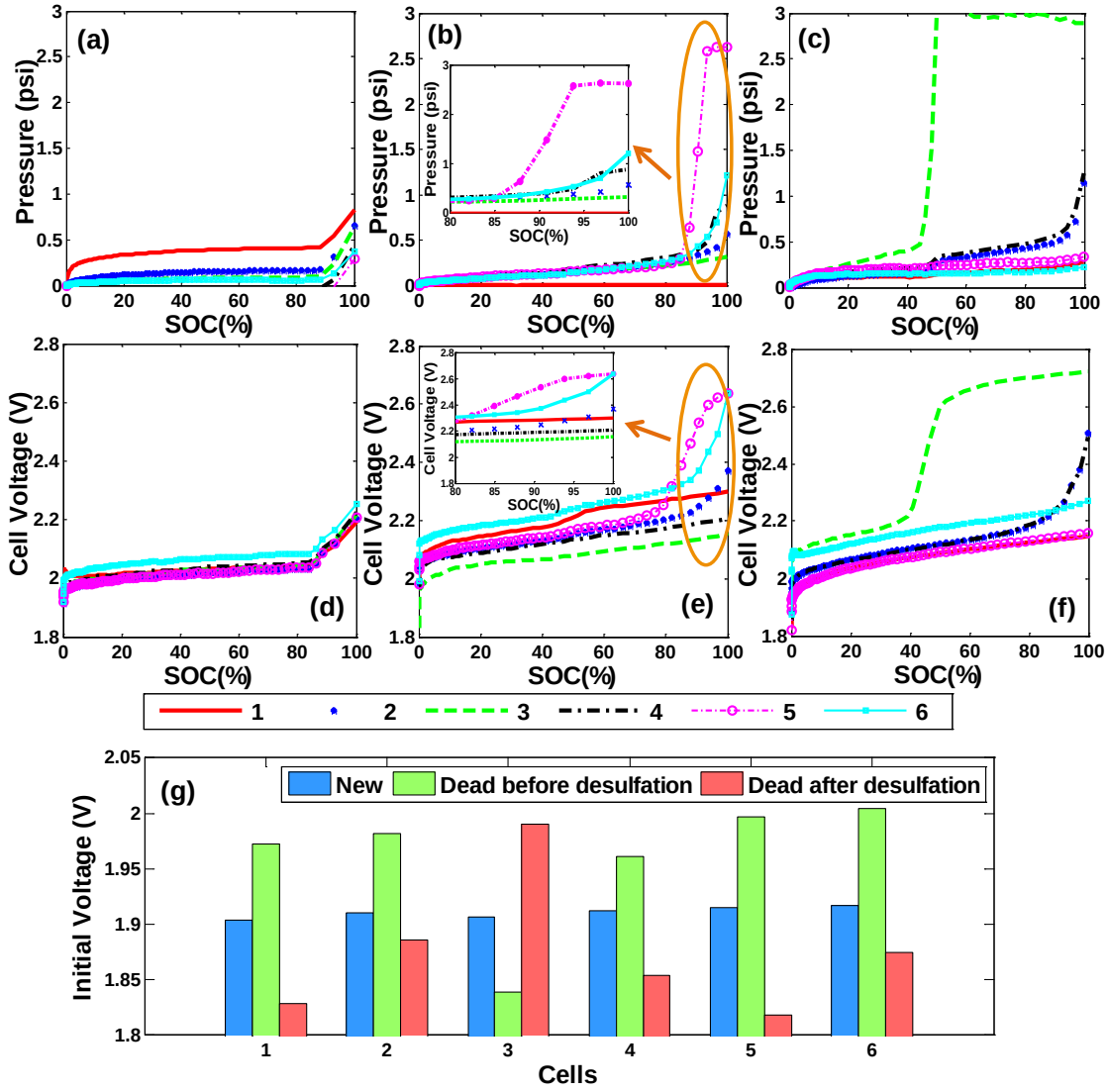

Figure 4.5. Charge of the new and the dead batteries: (a) Cell pressure of the new battery; (b) Cell pressure of the dead battery before desulfation with inset showing the pressure build-up at the end of charge; (c) Cell Pressure of the dead battery after desulfation; (d) Cell voltage of the new battery; (e) Cell voltage of the dead battery before desulfation with inset showing voltage rise at the end of charge; (f) Cell voltage of the dead battery after desulfation; (g) Initial cell voltages of the new and the dead batteries before and after desulfation

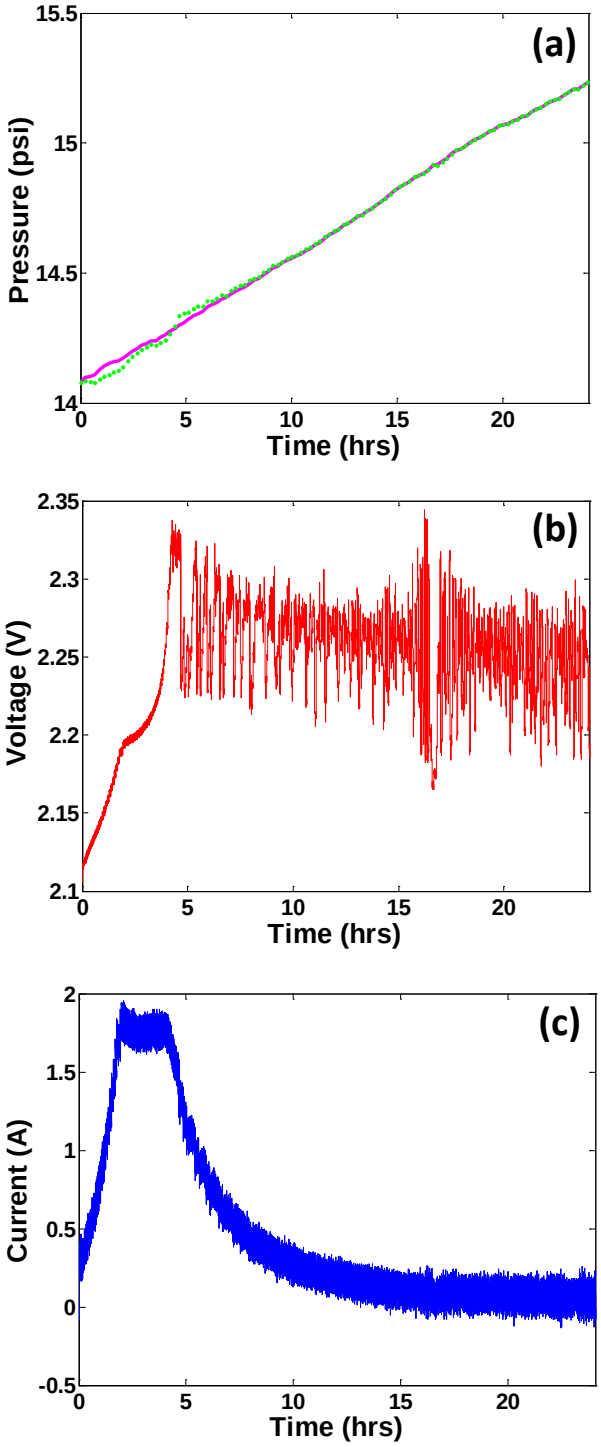

Figure 4.6. Desulfation charge control experimental time response: (a) pressure, desired (magenta-solid) and measured (green-dotted); (b) voltage; and (c) current

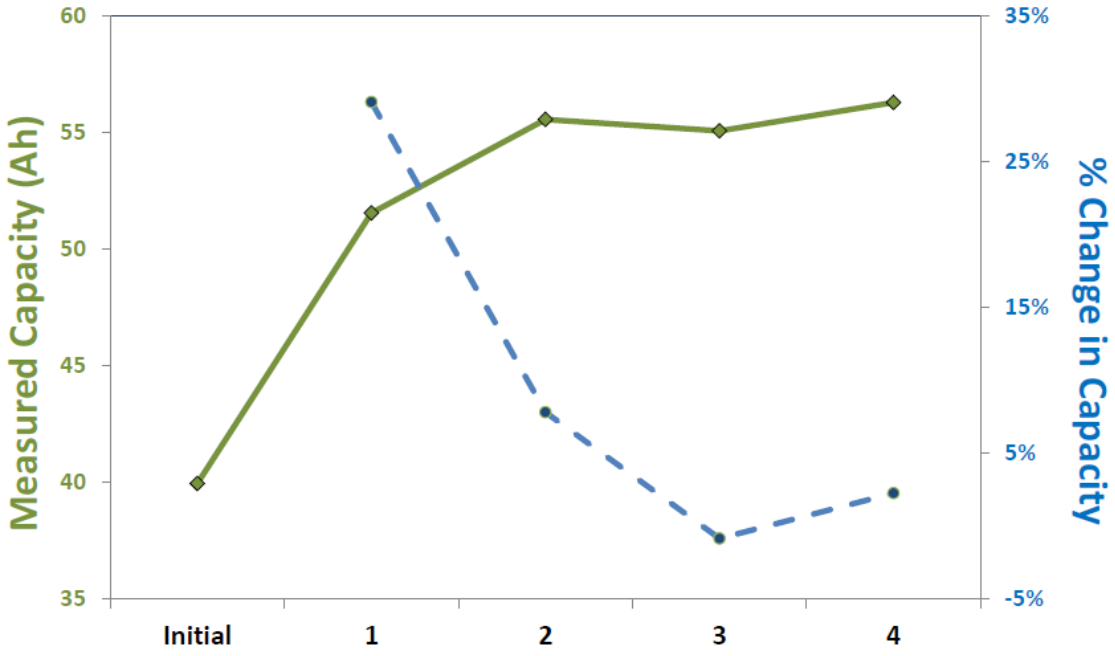

Figure 4.7. Capacity after desulfation: Measured cell capacity after each desulfation test, left (green-solid); Percent of the change in cell capacity, right (blue-dashed)

Chapter 5

A Control-Oriented Model for Lead-Acid Batteries Including Degradation

5.1 Introduction

Large-scale battery packs are a crucial and costly component of many "green" technologies, especially in hybrid vehicles and renewable energy applications. State-of-the-art battery packs are often greatly oversized and underutilized for safety and reliability reasons, resulting in higher cost. Downsizing battery packs is possible with more sophisticated battery management systems (BMS) that can push the cells to operate in a wider SOC range and under higher rate load without the risk of premature degradation or thermal runaway. With an advanced BMS, manufacturers and users can also cut cost on maintenance and warranties. One key element of an advanced BMS is models with high fidelity and low computational costs, which can predict the battery performance accurately and be easily adopted for state estimators design.

In this work, a lumped, nonlinear state space model is developed including two electrolysis side reactions. The model captures cell performance at high SOC during both charge and overcharge. The model is experimentally validated using a VRLA battery with cell voltage and pressure sensing.

5.2 Electrochemical Model

A VRLA cell consists of two electrodes with a separator in between. During discharge, the cell outputs energy by consuming lead, lead dioxide, and sulfuric acid to produce lead sulfate and water. During charge, it absorbs energy to decompose lead sulfate back into lead, lead dioxide, and sulfuric acid. The primary reactions are

$$\text{(Anode)}\ \ \mathrm{PbSO_4} + 2\,\mathrm{H_2O} \underset{discharge}{\overset{charge}{\rightleftharpoons}} \mathrm{PbO_2^-} + 3\,\mathrm{H^+} + 2\,\mathrm{e^-}, \tag{5.1}$$

$$\text{(Cathode)}\ \ \mathrm{PbSO_4} + \mathrm{H^+} + 2\,\mathrm{e^-} \underset{discharge}{\overset{charge}{\rightleftharpoons}} \mathrm{Pb} + \mathrm{HSO_4^-}. \tag{5.2}$$

The standard electrode potentials for the primary reactions are

$$E^o_{PbO_2/PbSO_4} = 1.636V \text{ vs. SHE},$$
$$E^o_{Pb/PbSO_4} = -0.295V \text{ vs. SHE}.$$

The overall cell potential depends on acid concentration, as described by the Nernst Equation [1],

$$E_{cell} = 1.931 + \frac{RT}{nF} ln\left(\frac{c_{H^+} c_{HSO_4^-}}{c_{H_2O}}\right), \tag{5.3}$$

where $R = 8.314 J/(K\,mol)$ is the universal gas constant, $F = 9.64810^{-4} C/mol$ is Faraday's constant, T is the temperature in K, n is the number of moles of electrons transferred, and c_{H_2O}, c_{H^+}, and $c_{HSO_4^-}$ are the reactant concentrations. The cell potential increases during charge because acid concentration is increasing.

In addition to the primary reactions, side reactions may occur during charge/overcharge. Oxygen evolves and hydrogen recombines at the anode. At the cathode, oxygen is oxidized and hydrogen is generated. These side reactions are

$$\text{(Anode)}\ \ 2\,\mathrm{H_2O} \rightarrow \mathrm{O_2} + 4\,\mathrm{H^+} + 4\,\mathrm{e^-}, \tag{5.4}$$

$$\mathrm{H_2} \rightarrow 2\,\mathrm{H^+} + 2\,\mathrm{e^-}, \tag{5.5}$$

$$\text{(Cathode)}\ \ \mathrm{O_2} + 4\,\mathrm{H^+} + 4\,\mathrm{e^-} \rightarrow 2\,\mathrm{H_2O}, \tag{5.6}$$

$$2\,\mathrm{H^+} + 2\,\mathrm{e^-} \rightarrow \mathrm{H_2}. \tag{5.7}$$

with the standard electrode potentials

$$E^o_{O_2} = 1.23V \text{ vs. SHE},$$
$$E^o_{H_2} = 0V \text{ vs. SHE}.$$

Oxygen evolution accelerates when the anode potential is above $E^o_{O_2}$ and hydrogen evolution accelerates when the cathode potential is below $E^o_{H_2}$. Similarly, oxygen and hydrogen recombine when the electrode potential magnitudes are smaller than $E^o_{O_2}$ and $E^o_{H_2}$, respectively. The electrode potentials of the main reactions are greater in magnitude than the gas production thresholds ($E^o_{Pb/PbSO_4} < E^o_{H_2}$ and $E^o_{PbO_2/PbSO_4} > E^o_{O_2}$), so hydrogen and oxygen continually evolve during charging. Thus, these secondary reactions are unavoidable [93] but the gas generation rates are extremely small for low overpotential. Here, overpotential denotes how much an electrode potential shifts from its open circuit potential (OCV). The oxygen and hydrogen evolution rates increase exponentially with overpotential, according to Tafel/Bulter-Volmer kinetics [93].

Oxygen generated at the anode passes through the electrolyte and overhead space and then recombines at the cathode, forming an internal oxygen cycle. Similarly, hydrogen can be transported to and recombined at the positive electrode, but the hydrogen recombination rate is usually so small due to poor kinetics that it is neglected [98, 62].

5.3 Lumped Nonlinear Model

The lumped, nonlinear model is based on the following assumptions:

1. The acid and gas concentrations are assumed to be equal to their volumetric averages, $\bar{c}^H$, $\bar{c_e}^{O_2}$, $\bar{c_g}^{O_2}$ and $\bar{c_g}^{H_2}$. These are state variables of the lumped model.

2. The oxygen recombination kinetics are assumed to be much slower than the oxygen generation kinetics and are, therefore, neglected ($\bar{c_e}^{O_2} = 0$).

3. The electrode conductivity is assumed to be large so the solid phase potentials within each electrode are uniformed at $\phi_{s,p}$ and $\phi_{s,m}$.

4. The electrolyte potential as the cell reference voltage and set equal to zero.

5. Hydrogen recombination is neglected.

6. The cell temperature T is assumed to be known.

The resulting nonlinear model has 5 states (concentrations $\left\{\bar{c}^H, \bar{c_g}^{O_2}, \bar{c_g}^{H_2}\right\}$ and electrode potentials $\left\{\phi_{s,p}, \phi_{s,m}\right\}$), one input (current I), and two outputs (cell voltage and pressure rise $\{V, \Delta p\}$). Based on [98, 63], the state equations are

$$\begin{aligned}\dot{\bar{c}}^H =& \frac{1}{\rho}\left[L_p \frac{3-2t_+^0}{2F} a_{e,p} i_{e,p} + L_p \frac{1-t_+^0}{F} a_{e,p}^{O_2} i_{e,p}^{O_2}\right. \\ &\left. + L_m \frac{1-2t_+^0}{2F} a_{e,m} i_{e,m} + L_m \frac{1-t_+^0}{F} a_{e,m}^{H_2} i_{e,m}^{H_2}\right], \end{aligned} \tag{5.8}$$

$$\dot{\bar{c}}_g^{O_2} = \frac{1}{4F\rho} L_p a_{e,p}^{O_2} i_{e,p}^{O_2}, \tag{5.9}$$

$$\dot{\bar{c}}_g^{H_2} = \frac{L_m}{2F\rho} a_{e,m}^{H_2} i_{e,m}^{H_2} RT, \tag{5.10}$$

$$\dot{\phi}_{s,p} = \frac{1}{a_{dl,p} C_{dl,p}} \left(\frac{I}{AL_p} - a_{e,p} i_{e,p} - a_{e,p}^{O_2} i_{e,p}^{O_2}\right), \tag{5.11}$$

$$\dot{\phi}_{s,m} = \frac{1}{a_{dl,m} C_{dl,m}} \left(-\frac{I}{AL_m} - a_{e,m} i_{e,m} - a_{e,m}^{H_2} i_{e,m}^{H_2}\right), \tag{5.12}$$

The states are coupled by transfer current densities through nonlinear Bulter-Volmer and Tafel kinetics,

$$i_{e,j} = i_{0,ref,j} \left(\frac{c^H}{c_{ref}^H}\right)^{\gamma_j^H} \left[exp\left(\frac{\alpha_{aj} F}{RT}\eta_j\right) - exp\left(-\frac{\alpha_{cj}}{RT}\eta_j\right)\right], \tag{5.13}$$

$$\begin{aligned} i_{e,j}^{O_2} =& i_{0,ref,j}^{O_2} \left(\frac{c^H}{c_{ref}^H}\right)^{\gamma_j^{O_2}} \left[exp\left(\frac{\alpha_{aj}^{O_2} F}{RT}\eta_j^{O_2}\right)\right. \\ &\left. - \left(\frac{c_e^{O_2}}{c_{e,ref}^{O_2}}\right)^{\delta_j^{O_2}} exp\left(-\frac{\alpha_{cj}^{O_2} F}{RT}\eta_j^{O_2}\right)\right], \end{aligned} \tag{5.14}$$

$$i_{e,j}^{H_2} = -i_{0,ref,j}^{H_2} \left(\frac{c^H}{c_{ref}^H}\right)^{\gamma_j^{H_2}} exp\left(-\frac{\alpha_{cj}^{H_2}}{RT}\eta_j^{H_2}\right), \tag{5.15}$$

where $j = p$ (anode) or m (cathode) and the overpotentials

$$\eta_j = \phi_s - \phi_e - U_j, \tag{5.16}$$

$$\eta_j^{O_2} = \phi_s - \phi_e - U_j^{O_2}, \tag{5.17}$$

$$\eta_j^{H_2} = \phi_s - \phi_e - U_j^{H_2}. \tag{5.18}$$

The output equations are

$$V_{cell} = \phi_{s,p} - \phi_{s,m} + R_c I, \tag{5.19}$$

$$\Delta p = \left(\bar{c_g}^{O_2} + \bar{c_g}^{H_2}\right) RT + \frac{p_0}{T_0} T. \tag{5.20}$$

All model parameters and variables are listed in the Nomenclature.

Nonlinearity from specific interfacial area evolution is included in the model to capture cell performance during full charge and overcharge. During charge, the specific interfacial area for the primary reactions evolves according to

$$a_{e,i} = a_{e,i,max}\left(1 - EUC^{\zeta_1}\right), \tag{5.21}$$

where $i = p,m$. The specific interfacial areas for the side reactions and the double layer effect

$$a_i = a_{i,max} EUC^{\zeta_2}, \tag{5.22}$$

where $i = O_2, H_2, dl$. The electrode utilization coefficient,

$$EUC = b(1 - SOC), \tag{5.23}$$

where

$$SOC = \frac{\bar{c}^H - \bar{c}^H_{min}}{\bar{c}^H_{max} - \bar{c}^H_{min}}. \tag{5.24}$$

5.4 Model validation and Analysis

The nonlinear lumped model was validated with cell testing data from a 12V, 70Ah VRLA AGM battery consisting of six modules in series and 18 cells in parallel in each module. The parameters used in the model were taken from the battery specifications and literature and are listed in Tab. 5.1. The nonlinear ODEs were integrated numeri-

cally in MATLAB. The battery was modified to allow independent voltage and pressure measurement for all six modules. Temperature change was estimated from the lumped thermal capacitance and heat transfer to/from the cell. The battery was tested using a battery testing station consisting of an AE Techron LVC 5050 linear amplifier, dSPACE DAQ system, and additional custom-built circuits (See Fig. 5.1) [99, 78].

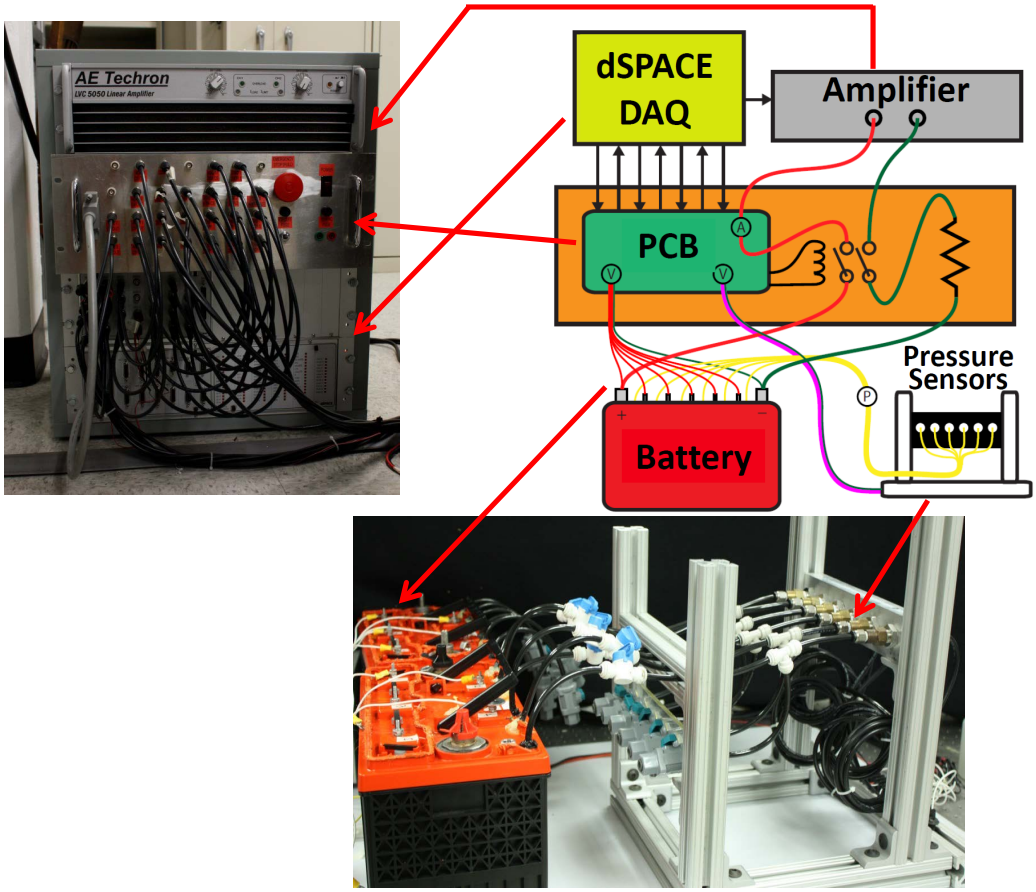

Figure 5.1. Scheme of the experimental setup

Figures 5.2 (a), (b), (c), and (d) illustrate the results from two simulations and experiments using data from one module of the VRLA battery. The first test starts from 60% SOC with a constant charge rate of 0.1C and the second test starts from 30% SOC and charges at 0.15C. The model responses (solid lines) and the testing results (markers) match very well. The model successfully captures the cell voltage behavior, deviating only slightly during overcharge when the voltage and pressure rise quickly due to the electrolysis side reaction. During overcharge, the cell response is no longer linear and

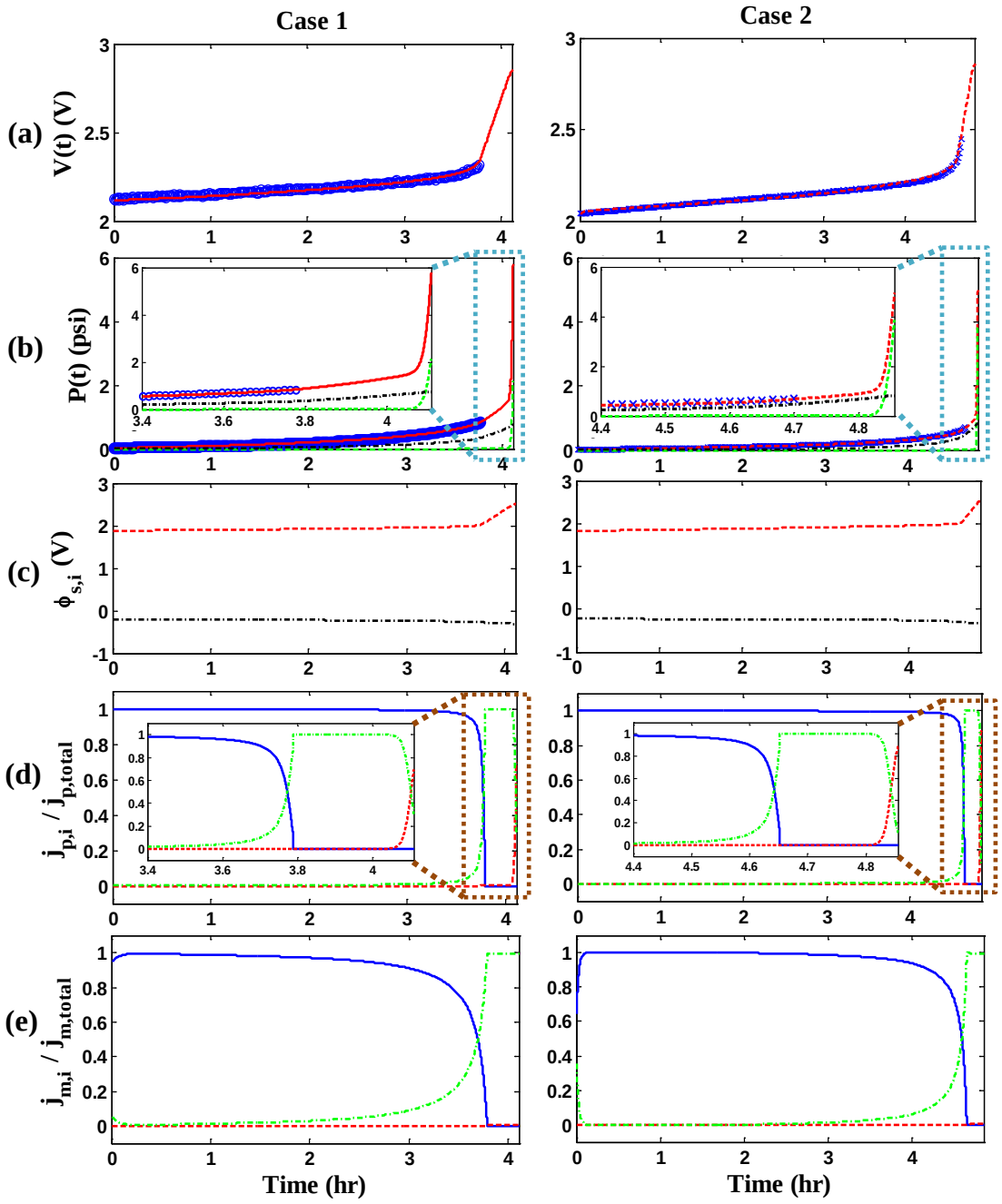

Figure 5.2. Experimental (○ and ×) and simulated (lines) charging results for one module of a 12V 70Ah Pb-Acid battery at 0.1C (Case 1 - left column) and 0.15C (Case 2 - right column): (a) Voltage; (b) Pressure (simulated total-solid, oxygen-dashed, and hydrogen-dash-dotted); (c) Anode (dashed) and cathode (dash-dotted) potentials; (d) Anode reaction current ratios for the primary reaction (solid), oxygen evolution (dashed), and the double layer (dash-dotted); (e) Cathode reaction current ratios for the primary reaction (solid), hydrogen evolution (dashed), and the double layer (dash-dotted).

Table 5.1. Model Parameters

Parameters	Value
γ_p^H	0
γ_m^H	0
$\gamma_p^{O_2}$	6
$\gamma_m^{H_2}$	2
$\delta_p^{O_2}$	2
ζ_1	0.083 for SOC$<$70%; 0.2 otherwise
ζ_2	0.05 for SOC$<$75%; 0.4 otherwise
A	415.34 cm^2
b	0.7
$C_{dl,p}$	0.005 F/cm^2
$C_{dl,m}$	0.005 F/cm^2
C_v	0.00121 $J/(mol\ K)$
F	96485 C/mol
H'	0.03181
$i_{0,ref,p}^H$	4.45e-6 A/cm^2
$i_{0,ref,m}^H$	5.77e-7 A/cm^2
$i_{0,ref,p}^{O_2}$	2.5e-30 A/cm^2
$i_{0,ref,m}^{H_2}$	9.36e-15 A/cm^2
k	10 cm/s
L_p	0.159 cm
L_{sep}	0.159 cm
L_m	0.159 cm
R	8.3143 $J/(mol\ K)$
R_c	0.0045 Ω
T	298 K
t_+^0	0.72
U^{O_2}	1.64 V
U^{H_2}	0.35 V
v	2286 cm^3

the current switches from the primary reactions to the gassing reactions, causing the overpotentials on both electrodes to separate even further. These high overpotentials are observed in the simulated and experimental cell voltages after 3.4 hrs (Case 1) and 4.2 hrs (Case 2) in Fig. 5.2 (a). The model also predicts the pressure responses quite well. Figure 5.2 (b) show that the pressure rises almost linearly during the initial charge due to thermal expansion from internal heat generation. During overcharge, the pressure grows

rapidly due to the accelerated gas generation, especially oxygen evolution.

The model also reveals how the internal battery states evolve. Figures 5.2 (c) show that the anode solid phase potentials contribute more to the cell voltage rise than the cathode solid phase potentials. This is because oxygen generation initiates before hydrogen generation during overcharge. The reaction current densities, shown in Figs. 5.2 (d), reflect this result. The anode reaction current density for the primary reaction dominates initially. During overcharge, the primary reaction slows down because all available active materials have been consumed. The double layer capacitance then begins to charge, providing a quick rise in solid phase potential. This accelerates oxygen generation, as indicated by the rise of oxygen reaction current density.

Similar processes occur in cathode but later in the overcharge process when potential is significantly high, as shown in Figs. 5.2 (f).

5.5 Conclusions

The nonlinear 5th-order state space model including degradation is developed in this work. It preserves the electrochemical processes and parameters of the underlying fundamental PDE model. Validated with testing data, the model accurately captures the voltage and the pressure responses during charge and overcharge. The model also captures the potentials, reaction current densities, and gassing responses observed in the fundamental model, making it well suited for model-based analysis, simulation, estimation, and BMS design.

Chapter 6

A Health-Cautious Charging Strategy for Lead-Acid Cells

6.1 Introduction

6.1.1 Electrochemical Model

A VRLA cell consists of two electrodes with a separator in between. During discharge, the cell outputs energy by consuming lead, lead dioxide, and sulfuric acid to produce lead sulfate and water. During charge, it absorbs energy to decompose lead sulfate back into lead, lead dioxide, and sulfuric acid. The primary reactions are

$$\text{(Anode)}\ \ \mathrm{PbSO_4} + 2\mathrm{H_2O} \underset{discharge}{\overset{charge}{\rightleftharpoons}} \mathrm{PbO_2^-} + 3\mathrm{H^+} + 2\mathrm{e^-}, \tag{6.1}$$

$$\text{(Cathode)}\ \ \mathrm{PbSO_4} + \mathrm{H^+} + 2\mathrm{e^-} \underset{discharge}{\overset{charge}{\rightleftharpoons}} \mathrm{Pb} + \mathrm{HSO_4^-}. \tag{6.2}$$

In addition to the primary reactions, side reactions may occur during charge/overcharge. Oxygen evolves and hydrogen recombines at the anode. At the cathode, oxygen is oxidized and hydrogen is generated. These side reactions are

$$\text{(Anode)}\ \ 2\mathrm{H_2O} \rightarrow \mathrm{O_2} + 4\mathrm{H^+} + 4\mathrm{e^-}, \tag{6.3}$$

$$\mathrm{H_2} \rightarrow 2\mathrm{H^+} + 2\mathrm{e^-}, \tag{6.4}$$

$$\text{(Cathode)}\ \ \mathrm{O_2} + 4\mathrm{H^+} + 4\mathrm{e^-} \rightarrow 2\mathrm{H_2O}, \tag{6.5}$$

$$2\mathrm{H}^{+} + 2\mathrm{e}^{-} \rightarrow \mathrm{H}_2. \tag{6.6}$$

with the standard electrode potentials

$$E^{o}_{O_2} = 1.23V \text{ vs. SHE},$$
$$E^{o}_{H_2} = 0V \text{ vs. SHE}.$$

Oxygen evolution accelerates when the anode potential is above $E^{o}_{O_2}$ and hydrogen evolution accelerates when the cathode potential is below $E^{o}_{H_2}$. Similarly, oxygen and hydrogen recombine when the electrode potential magnitudes are smaller than $E^{o}_{O_2}$ and $E^{o}_{H_2}$, respectively. The electrode potentials of the main reactions are greater in magnitude than the gas production thresholds ($E^{o}_{Pb/PbSO_4} < E^{o}_{H_2}$ and $E^{o}_{PbO_2/PbSO_4} > E^{o}_{O_2}$), so hydrogen and oxygen continually evolve during charging. Thus, these secondary reactions are unavoidable [93] but the gas generation rates are extremely small for low overpotential. Here, overpotential denotes how much an electrode potential shifts from its open circuit potential (OCV). The oxygen and hydrogen evolution rates increase exponentially with overpotential, according to Tafel/Bulter-Volmer kinetics [93].

Oxygen generated at the anode passes through the electrolyte and overhead space and then recombines at the cathode, forming an internal oxygen cycle. Similarly, hydrogen can be transported to and recombined at the positive electrode, but the hydrogen recombination rate is usually so small due to poor kinetics that it is neglected [98, 62].

6.1.2 Nonlinear State Space Model with Lumped Parameters

In previous work, a nonlinear model with lumped parameter has been developed by assuming

1. The acid and gas concentrations are assumed to be equal to their volumetric averages, $\bar{c}^{H}$, $\bar{c_e}^{O_2}$, $\bar{c_g}^{O_2}$ and $\bar{c_g}^{H_2}$. These are state variables of the lumped model.

2. The oxygen recombination kinetics are assumed to be much slower than the oxygen generation kinetics and are, therefore, neglected ($\bar{c_e}^{O_2} = 0$).

3. The electrode conductivity is assumed to be large so the solid phase potentials within each electrode are uniformed at η_{O_2} and η_m.

4. The electrolyte potential is the reference voltage and set equal to zero.

5. Hydrogen recombination is neglected.

6. The cell temperature T is assumed to be known.

The nonlinear model is fifth order with one input and two output,

$$\dot{\bar{c}}^{H} = \frac{1}{\rho}\left[L_p \frac{3-2t_+^0}{2F} a_{e,p} i_{e,p} + L_p \frac{1-t_+^0}{F} a_{e,p}^{O_2} i_{e,p}^{O_2} + L_m \frac{1-2t_+^0}{2F} a_{e,m} i_{e,m} + L_m \frac{1-t_+^0}{F} a_{e,m}^{H_2} i_{e,m}^{H_2}\right], \tag{6.7}$$

$$\dot{\bar{c}}_g^{O_2} = \frac{1}{4F\rho} L_p a_{e,p}^{O_2} i_{e,p}^{O_2}, \tag{6.8}$$

$$\dot{\bar{c}}_g^{H_2} = \frac{L_m}{2F\rho} a_{e,m}^{H_2} i_{e,m}^{H_2} RT, \tag{6.9}$$

$$\dot{\phi}_{s,p} = \frac{1}{a_{dl,p} C_{dl,p}} \left(\frac{I}{AL_p} - a_{e,p} i_{e,p} - a_{e,p}^{O_2} i_{e,p}^{O_2}\right), \tag{6.10}$$

$$\dot{\phi}_{s,m} = \frac{1}{a_{dl,m} C_{dl,m}} \left(-\frac{I}{AL_m} - a_{e,m} i_{e,m} - a_{e,m}^{H_2} i_{e,m}^{H_2}\right), \tag{6.11}$$

The states are coupled by transfer current densities through nonlinear Bulter-Volmer and Tafel kinetics,

$$i_{e,j} = i_{0,ref,j} \left(\frac{c^H}{c_{ref}^H}\right)^{\gamma_j^H} \left[exp\left(\frac{\alpha_{aj} F}{RT}\eta_j\right) - exp\left(-\frac{\alpha_{cj}}{RT}\eta_j\right)\right], \tag{6.12}$$

$$i_{e,j}^{O_2} = i_{0,ref,j}^{O_2} \left(\frac{c^H}{c_{ref}^H}\right)^{\gamma_j^{O_2}} \left[exp\left(\frac{\alpha_{aj}^{O_2} F}{RT}\eta_j^{O_2}\right) - \left(\frac{c_e^{O_2}}{c_{e,ref}^{O_2}}\right)^{\delta_j^{O_2}} exp\left(-\frac{\alpha_{cj}^{O_2} F}{RT}\eta_j^{O_2}\right)\right], \tag{6.13}$$

$$i_{e,j}^{H_2} = -i_{0,ref,j}^{H_2} \left(\frac{c^H}{c_{ref}^H}\right)^{\gamma_j^{H_2}} exp\left(-\frac{\alpha_{cj}^{H_2}}{RT}\eta_j^{H_2}\right), \tag{6.14}$$

where $j = p$ (anode) or m (cathode) and the overpotentials

$$\eta_j = \phi_s - \phi_e - U_j, \tag{6.15}$$

$$\eta_j^{O_2} = \phi_s - \phi_e - U_j^{O_2}, \tag{6.16}$$

$$\eta_j^{H_2} = \phi_s - \phi_e - U_j^{H_2}. \tag{6.17}$$

The output equations are

$$V_{cell} = \phi_{s,p} - \phi_{s,m} + R_c I, \tag{6.18}$$

$$\Delta p = \left(\bar{c_g}^{O_2} + \bar{c_g}^{H_2}\right) RT + \frac{p_0}{T_0} T. \tag{6.19}$$

All model parameters and variables are listed in the Nomenclature.

Nonlinearity also comes from specific interfacial area evolution. During charge, the specific interfacial area for the primary reactions evolves according to

$$a_{e,i} = a_{e,i,max}\left(1 - EUC^{\zeta_1}\right), \tag{6.20}$$

where $i = p,m$. The specific interfacial areas for the side reactions and the double layer effect

$$a_i = a_{i,max} EUC^{\zeta_2}, \tag{6.21}$$

where $i = O_2, H_2, dl$. The electrode utilization coefficient,

$$EUC = b(1 - SOC), \tag{6.22}$$

The nonlinear lumped model was validated with cell testing data from a 12V, 70Ah VRLA AGM cell and showed good prediction on the cell performance.

6.2 Health-Cautious Charging Strategy

The conventional charging protocol is constant current followed by constant voltage, CC-CV charge. A cell is charged under constant current until it hits a maximum voltage; then the cell is switched to be charged at that voltage with current being tailored down to its minimum. The CV step often overcharges a cell, which is critical to restore the full capacity back in the cell but, on the other side, also introduces side reactions such as water electrolysis/gassing. The reaction rates of electrolysis heavily depends on the holding voltage. The higher the holding voltage, the faster the cell gases. In practical, the hold-

ing voltage is often chosen empirically, based on new cell ratings, and stays the same throughout a cell's service life. As the cell degrades, internal impedance increases and capacity fades, the cell will experience more gassing during the same CV step. Lowering the CV holding voltage helps but lower to which level is a tricky question, especially if one cell has unbalanced degraded electrodes. Previous work [78] illustrates an alternative charging protocol, constant-current constant-pressure-generation-rate, which controls the charging current and the gassing rate by using pressure feedback. The charging protocol was able to direct more input energy towards the primary reactions while suppressing gassing. The desulfation experiments showed that this charging protocol could reduce lead sulfate crystals, restore more capacity, produce less gassing during overcharge and achieve better charging acceptance. However, few lead-acid batteries from the market are equipped with pressure sensors. Installing one to each cell on commercial lead-acid batteries can be costly and time-consuming, especially when there is a large-scale lead-acid battery pack. One way around it is to adopt a charge/overcharge model of lead-acid cells and estimate and control overpotentials, η's, use the model. Based on Eq.6.13, 6.14, 6.16, and 6.17, the gas generation rates are controlled by the overpotentials, η's. Therefore, using the charging protocol, constant-current constant-overpotential, will result in constant gas generation rate at desired level.

In a lead-acid cell, positive overpotential, η_{O_2}, directly controls oxygen generation and negative overpotential, η_{H_2}, controls hydrogen generation. Thus, there are three variations to control the overpotentials, on the positive electrode, on the negative electrode, or both. When controlling both η_{H_2} and η_{O_2}, if one potential limit is more conservative than the other, say minimum η_{H_2} is the dominant constraint, the control effect will be the same as only limiting η_{H_2}. If the two potential limits are comparable, i.e., both of them are active, the control effect will look like a CC-CV case. Therefore, this work will focus on controlling η_{H_2} and η_{O_2} separately and comparing with CC-CV charging.

Also in this work, two SOC estimators are studied and compared – current counting and internal acid level. The current counting method basically integrals the current over time, assuming that all the input charge goes to restore cell capacity. This methods is simple and fairly accurate for medium and low SOC region, but it starts losing accuracy when the SOC is getting close to full, the cell is being overcharged, and the side reactions starts to kick in and steal input energy from the primary reactions. The second method uses the internal acid concentration level as an indicator of SOC. When a cell is

charged, lead sulfate is decomposed to acid, lead and lead dioxide, raising the internal acid concentration. Therefore, the SOC estimation based on the internal acid concentration is more accurate and robust, not affected by SOC range. The only cavity of this method is that if the cell degrades mainly due to dry out or corrosion instead of sulfation, its overall internal acid concentration will be pumped up. One need to calibrate the reference internal acid concentration at 100% SOC to keep the estimation accurate.

6.2.1 Simulation and Analysis

In this study, ϕ_e is taken as the reference. The three charging protocols with different holding voltages/overpotentials are compared:

- Constant-current constant-Voltage with maximum voltages at 2.28V, 2.3V, 2.35V, 2.4V, 2.45V, 2.47V;
- Constant-current constant-negative-overpotential with minimum η_{H_2} at -0.52V, -0.54V, -0.56V, -0.57V, -0.58V, -0.60V;
- Constant-current constant-positive-overpotential with maximum η_{O_2} at 0.44V, 0.46V, 0.47V, 0.48V, 0.49V, 0.50V.

They all have with the same battery parameters and initial conditions, start at 80% SOC in constant-current mode with a current at 10A, and end after 4 hours.

In all scenarios, the current started at maximum then tapered down to small levels as shown in Fig. 6.1. With low cell voltages (solid blue and solid red shown in inset (i)) or low negative overpotentials (dashed blue and dashed red shown in inset(ii)), the current started taper right after it passed 80% SOC, much earlier than the other cases. But these early in current decrease have much slower decay rates than other cases. In the inset (i), it is obvious that, during CC-CV charge, the higher the holding voltage, the longer it stays at maximum current. After switching to voltage control mode, the higher voltage cases drop current faster than those with lower holding voltages. Inset (ii) illustrates similar behaviors during CC-Cη_{H_2} charge and the general shapes of current very much resemble CC-CV cases. Lower (in magnitude) holding voltage yields earlier mode switch from CC to Cη but slower current decay afterward. CC-Cη_{O_2} shows a different trend in the inset (iii), lower holding voltage also leads to earlier switch. However, in

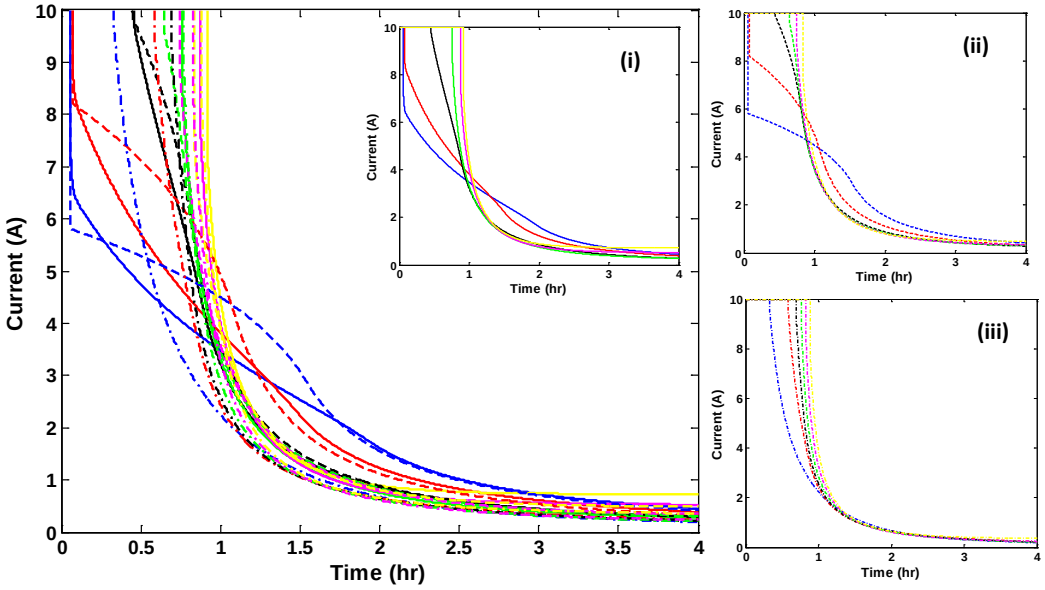

Figure 6.1. Current decrease under different charging protocols with insets showing (i) CC-CV (solid lines) at 2.28V (blue), 2.3V (red), 2.35V (black), 2.4V (green), 2.45V (magenta), 2.47V (yellow); (ii) CC-Cη_{H_2} (dashed lines) at -0.52V (blue), -0.54V(red), -0.56V (black), -0.57V (green), -0.58V (magenta), -0.60V (yellow); and (iii) CC-Cη_{O_2} (dash-dotted lines) at 0.44V (blue), 0.46V (red), 0.47V (black), 0.48V (green), 0.49V (magenta), 0.50V (yellow).

this case, the decay rates after switch are in general very close between different η_{O_2} cases, which indicates that topping at lower η_{O_2} gets less charge over the course.

Figure 6.2 shows the voltages using different charging strategies. The solid lines are the CV cases. The dashed lines and the dash-dotted lines represent the Cη_{H_2} and the Cη_{H_2} cases, respectively. During charge and overcharge, CC-Cη_{H_2} charging drives the cell voltage to increase fast initially and then the growth slows as the current gets reduced. On the other side, under CC-Cη_{O_2} charging, the cell voltages shoot up to the ceiling first then slowly creep down.

The gas productions for all the charging are shown in Figure 6.3. For all the three charging strategies, a larger (in magnitude) cell voltage/overpotential results in more gas generation because higher voltage cap leads to higher overpotential, which is a critical drive force on gassing. Also note that, in general, the dashed lines (Cη_{H_2} cases) have bigger slopes than the dash-dotted lines (Cη_{O_2} cases) which is due to the fact that the hydrogen exchange current is larger than the oxygen exchange current, i.e., the hydrogen

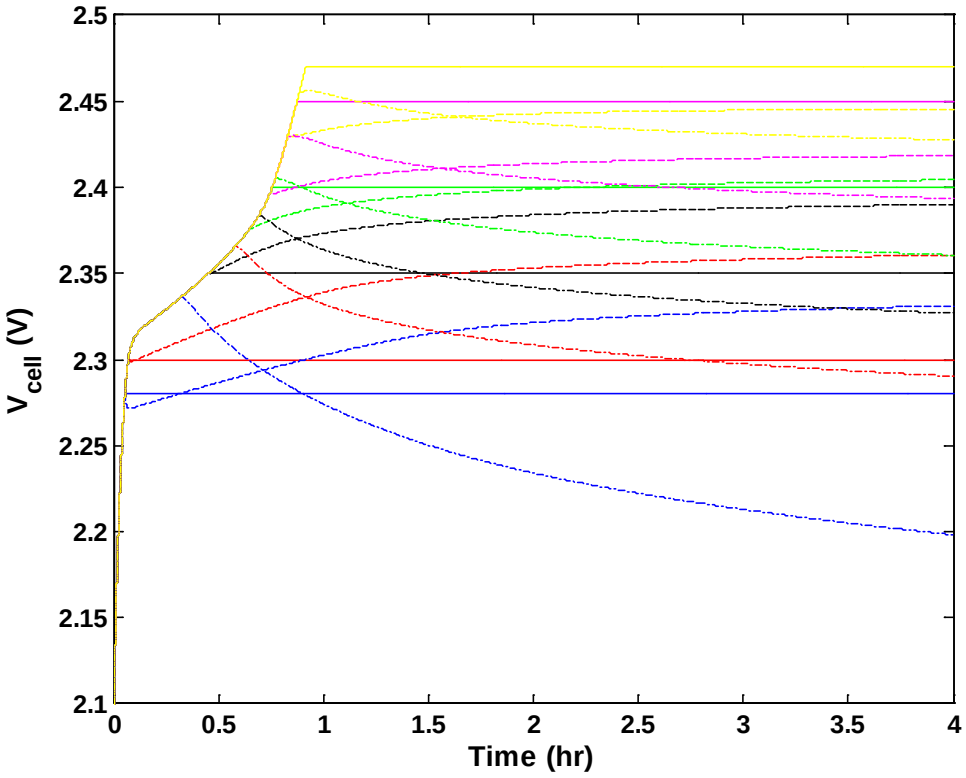

Figure 6.2. Cell voltage evolution under CC-CV (solid lines) charge at 2.28V (blue), 2.3V (red), 2.35V (black), 2.4V (green), 2.45V (magenta), 2.47V (yellow); under CC-Cη_{H_2} (dashed lines) at -0.52V (blue), -0.54V(red), -0.56V (black), -0.57V (green), -0.58V (magenta), -0.60V (yellow); and under CC-Cη_{O_2} (dash-dotted lines) at 0.44V (blue), 0.46V (red), 0.47V (black), 0.48V (green), 0.49V (magenta), 0.50V (yellow).

production is more energetic than the oxygen production.

The two SOC estimators are plotted in Figure 6.4 and 6.5. Again the higher the holding voltage/overpotential, the higher the SOC, which agrees with the current curves in Fig. 6.1, the less constrained voltage allows more current to be flooded in. The maximum SOC, which occurs in the case of CC-CV at 2.47V, reaches 112%. The minimum finishing SOC is 102%, under CC-Cη_{O_2} at 0.5V. However, the internal-acid-concentration-based SOC estimations shows that not all the input energy contribute to the primary reactions. As the charging progresses, the SOCs show diminishing returns. The SOC in the case of CC-CV at 2.47V only reaches 106% and the minimum case, CC-Cη_{O_2} at 0.5V, retains a similar curve as before, ending at 102%. This implies that

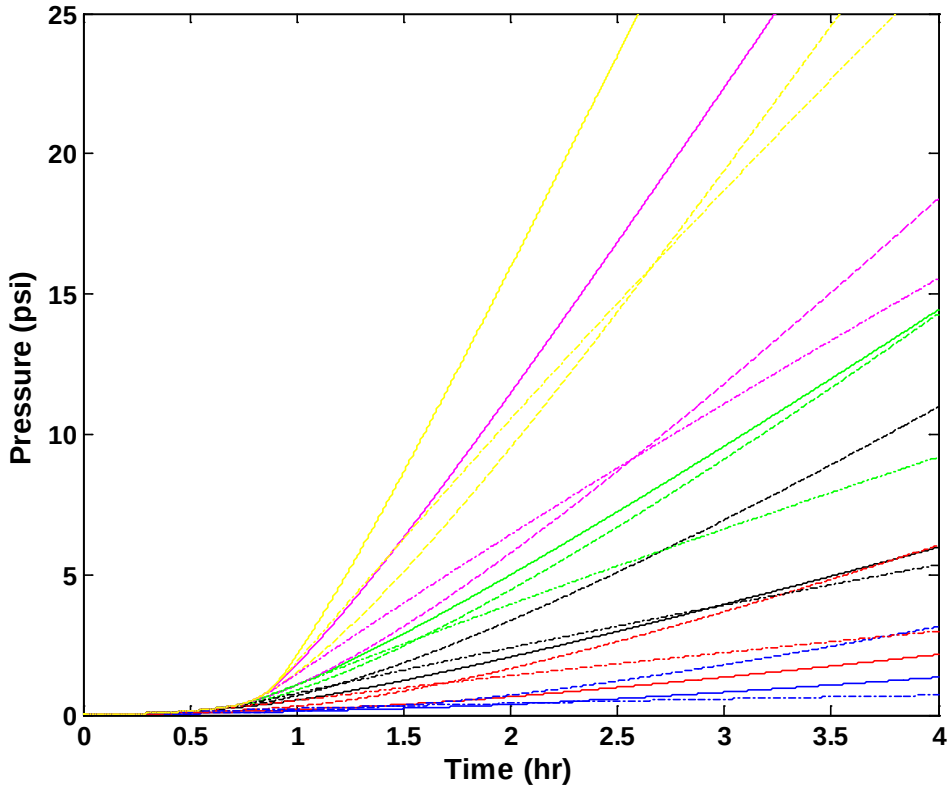

Figure 6.3. Gas generation under CC-CV (solid lines) charge at 2.28V (blue), 2.3V (red), 2.35V (black), 2.4V (green), 2.45V (magenta), 2.47V (yellow); under CC-Cη_{H_2} (dashed lines) at -0.52V (blue), -0.54V(red), -0.56V (black), -0.57V (green), -0.58V (magenta), -0.60V (yellow); and under CC-Cη_{O_2} (dash-dotted lines) at 0.44V (blue), 0.46V (red), 0.47V (black), 0.48V (green), 0.49V (magenta), 0.50V (yellow).

with lower holding voltage/potential, the charge efficiency is higher, i.e., less percent of input energy is wasted on side reactions. Comparing the two SOC estimators, the internal-acid-concentration-based one turns out to give better estimation in high SOC region.

6.2.2 Cast Study and Comparison

To compare the three charging strategies in details, three cases are picked up and compared toe-to-toe. One case runs CC-CV protocol which charges the cell at 10A constant current until the voltage hits 2.4V, then switches to CV mode and holds the cell voltage at 2.4V till the test time ends. Two cases run CC-Cη charge, using the ending overpo-

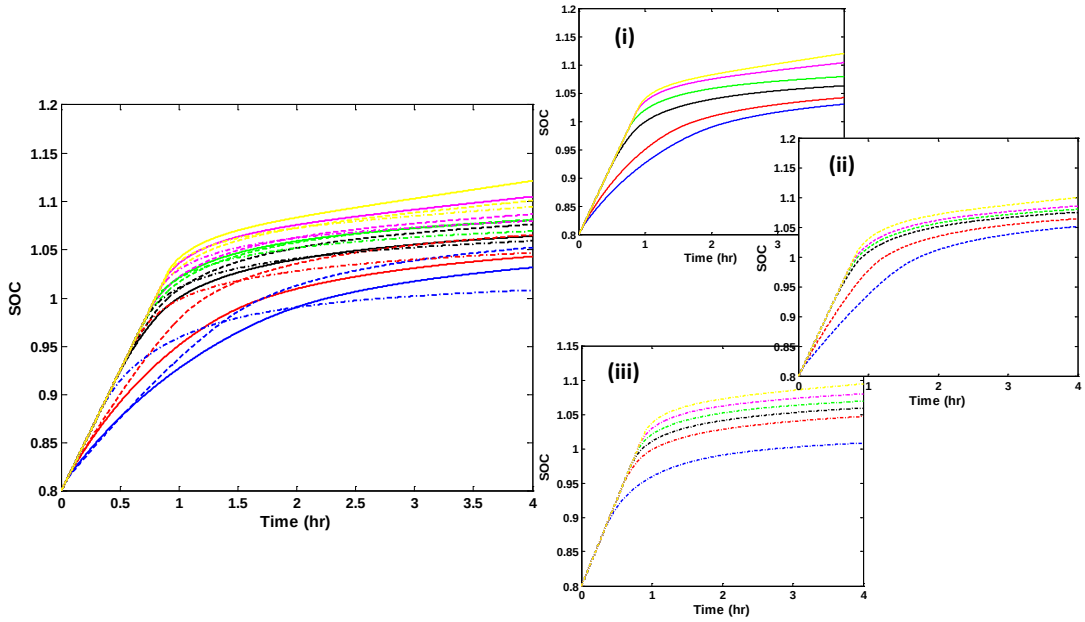

Figure 6.4. Current-counting-based SOC estimations under different charging protocols with insets showing (i) CC-CV (solid lines) at 2.28V (blue), 2.3V (red), 2.35V (black), 2.4V (green), 2.45V (magenta), 2.47V (yellow); (ii) CC-Cη_{H_2} (dashed lines) at -0.52V (blue), -0.54V(red), -0.56V (black), -0.57V (green), -0.58V (magenta), -0.60V (yellow); and (iii) CC-Cη_{O_2} (dash-dotted lines) at 0.44V (blue), 0.46V (red), 0.47V (black), 0.48V (green), 0.49V (magenta), 0.50V (yellow).

tentials in CC-CV case. Both starting with the same initial conditions as CC-CV charge, one switches to Cη_{O_2} mode at $0.49V$ and the other to Cη_{H_2} at $-0.57V$. Another two charges with tighter constraints, $\eta_{O_2} = 0.48V$ and $\eta_{H_2} = -0.56V$ are also investigated to illustrate the influence of the holding potentials on gassing and efficiency.

Figure 6.6 shows the current evolution during the five charge protocols. Generally, the current decreases exponentially during constant-voltage/overpotential stage. Compared with CC-CV (blue) and CC-Cη_{O_2} (black and magenta), holding negative overpotential (red and green) yields an earlier but smoother transition from constant current to constant voltage/ϕ_s. In contrast, CC-Cη_{O_2} charging cases stay in CC mode relatively longer than CC-CV and CC-Cη_{H_2} and the current drops faster after switching. This also indicates that CC-Cη_{H_2} charge takes in less energy than CV or Cη_{O_2}.

Figure 6.7 are the cell voltage and solid-phase potentials in the 5 cases. Similar to Fig. 6.2, CC-CV (blue) keeps the voltage constant while Cη_{H_2} increases the voltage

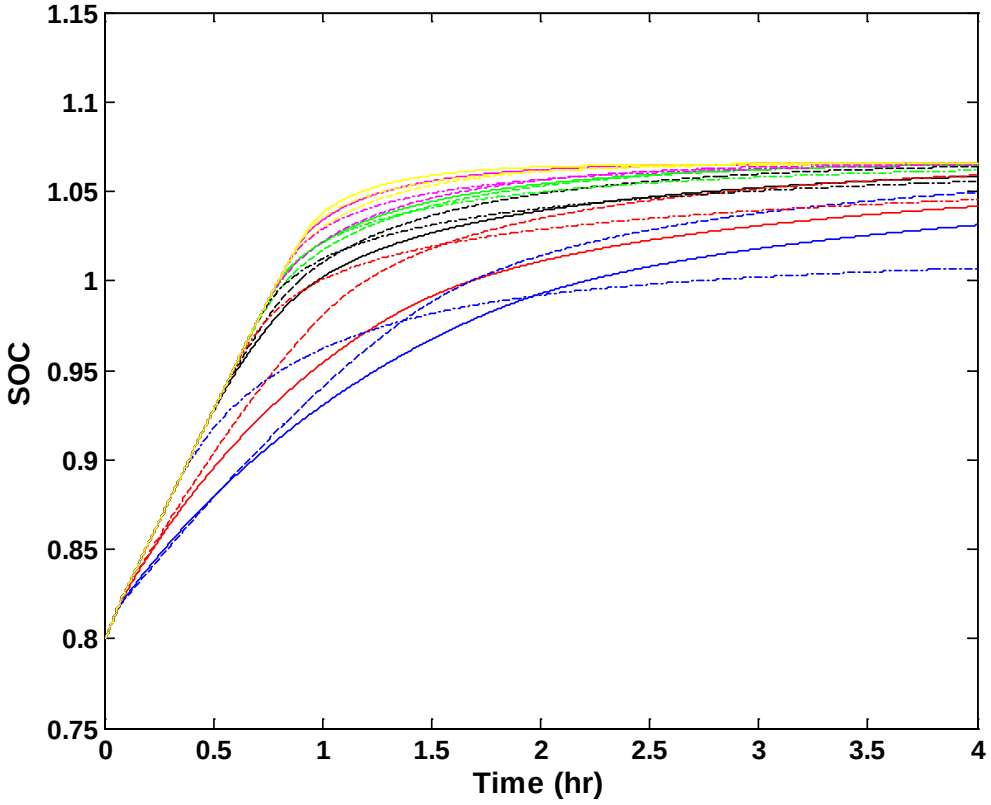

Figure 6.5. Internal-acid-concentration-based SOC estimations under CC-CV (solid lines) charge at 2.28V (blue), 2.3V (red), 2.35V (black), 2.4V (green), 2.45V (magenta), 2.47V (yellow); under CC-Cη_{H_2} (dashed lines) at -0.52V (blue), -0.54V(red), -0.56V (black), -0.57V (green), -0.58V (magenta), -0.60V (yellow); and under CC-Cη_{O_2} (dash-dotted lines) at 0.44V (blue), 0.46V (red), 0.47V (black), 0.48V (green), 0.49V (magenta), 0.50V (yellow).

gradually and Cη_{O_2} makes the current peaks first then slowly creep down. From the η_{H_2} and η_{O_2} subplots, it is obvious that if limiting one η , the other one will be constrained, too because basically suppressing half reaction of electrolysis will surely slow down the other half reaction.

Regarding the gas generation, shown in Fig. 6.8,CC-Cη_{O_2} with η_{O_2} held at 0.49V yields the largest gas generation while, if lowering η_{O_2} to 0.48V, the gas production is greatly reduced, slowest among the 5 cases. The main difference between the two comes from oxygen at the positive electrode. CC-Cη_{H_2} with η_{H_2} held at -0.57V generates similar gas volume as CC-CV at 2.4V. If move up the bar to -0.56V, the gas generation decreases by 25%, mainly from reduction in hydrogen production.

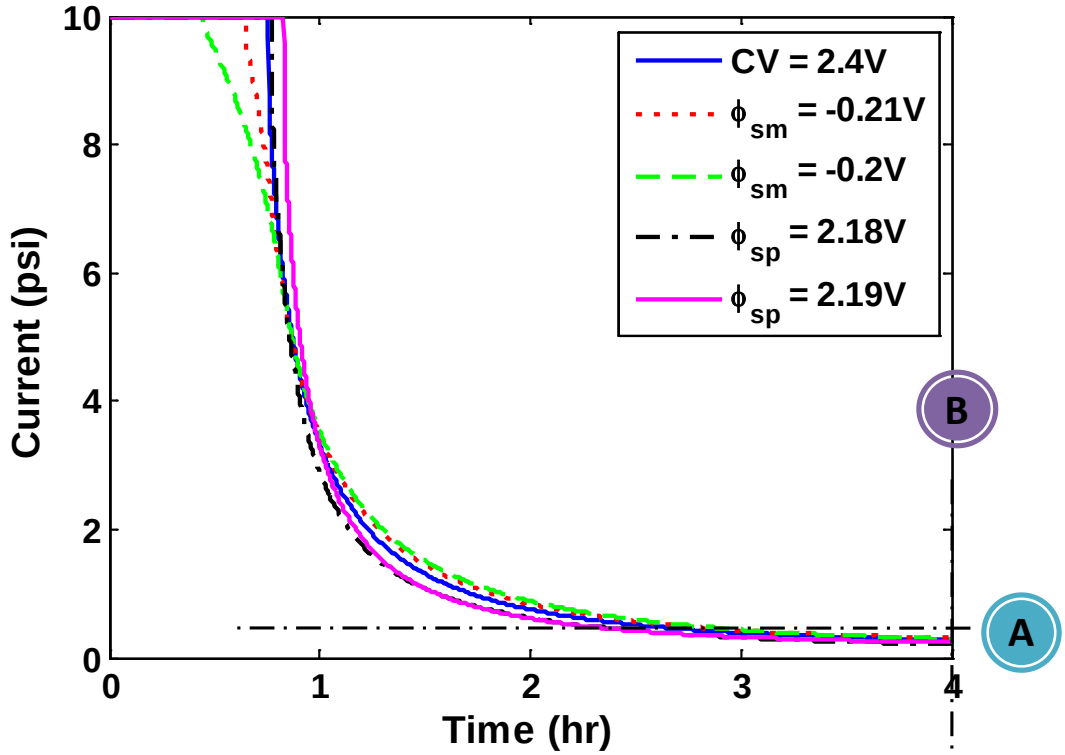

Figure 6.6. Current evolution during charge protocols: CC-CV at 2.4V (blue solid); CC-Cη_{H_2} at -0.57V (red dotted) and -0.56V (green dashed); CC-Cη_{O_2} at 0.48V (black dash-dotted) and 0.49V (magenta).

Figure 6.9 and 6.10 are SOC estimations based on current counting (Fig. 6.9) and internal acid concentration level (Fig. 6.10). Overall, the urrent counting method over-estimates the SOCs if compared to the internal acid concentration method. In Fig. 6.9, Cη_{O_2} at 0.49V (magenta) and CV at 2.4V (blue) charges result in the highest SOC which agrees with what has been observed in Fig. 6.6. In Fig. 6.10, even though Cη_{O_2} at 0.49V case (magenta) still shows slightly higher SOC around 106%, it is much closer to the others. This corresponds to the acid concentrations in Fig 6.11, which all approach the same value in the end.

To further investigate the three types of charging protocols and their effects, 5 case-by-case comparisons are conducted. Here, assume that acid concentration is the limiting factor for discharge and all acid restored can be beneficial for discharge. Therefore, one can use SOC_2/SOC_1 as the metric for charging efficiency, where SOC_1 is the current-

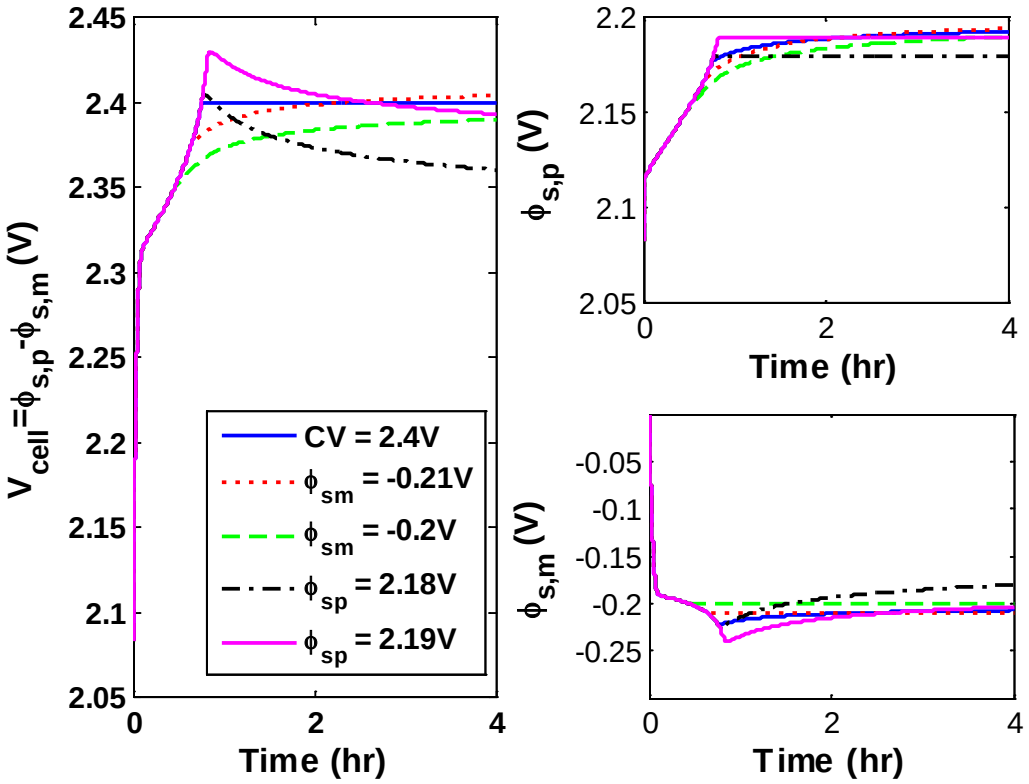

Figure 6.7. ϕ_s evolution during charge protocols: CC-CV at 2.4V (blue solid); CC-Cη_{H_2} at -0.57V (red dotted) and -0.56V (green dashed); CC-Cη_{O_2} at 0.48V (black dash-dotted) and 0.49V (magenta).

count-based SOC and SOC_2 is the internal-acid-concentration-based SOC.

6.2.2.1 Case A: Same finishing current

If take 0.4A as finishing criteria and end tests there ("A" in Fig. 6.6), the cell states from 5 charges are detailed in Table 6.1.

With $\phi_{s,m} = -0.57V$ (red), the finishing cell voltage is about 2.4V with slightly higher ending SOC but it takes longer to finish and generates more gas. Also, the charging efficiency is not as high as CV case (blue). If push the η_{H_2} to -0.56V (green), the charging time extends further and the cell voltage and SOC become lower but gas production is greatly reduced and charge efficiency is improved. On the other side, if limiting η_{O_2} to 0.49V (magenta), the max cell voltage quickly shoots to 2.43V then

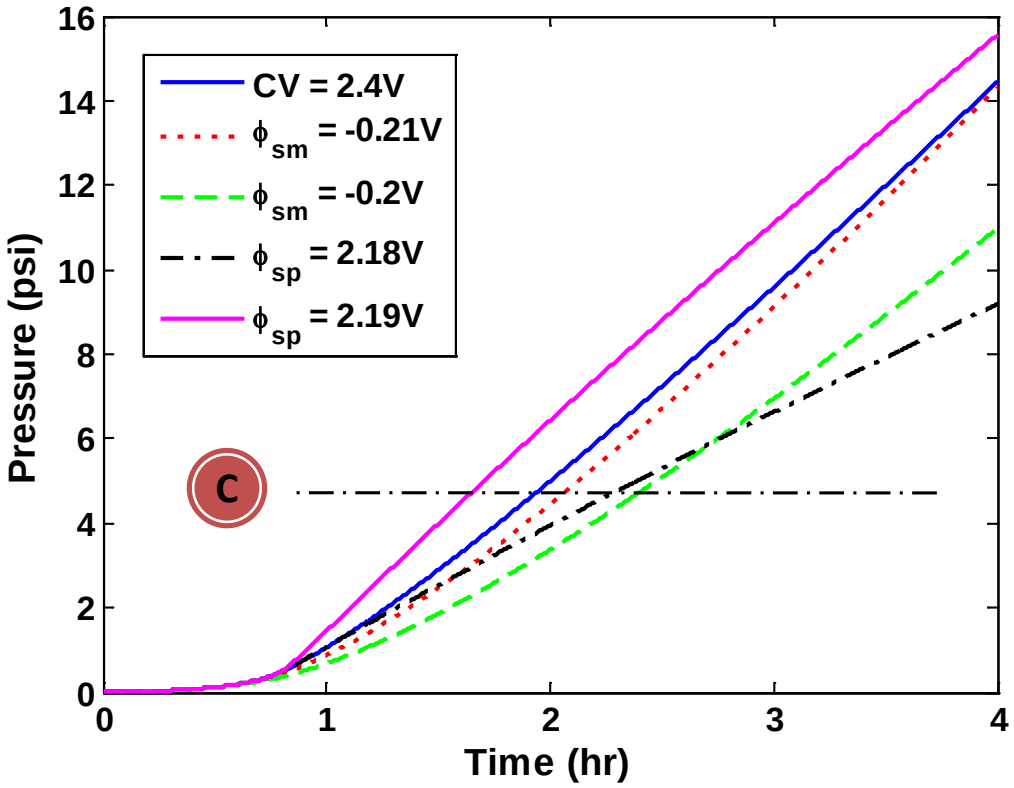

Figure 6.8. Pressure growth during charge protocols: CC-CV at 2.4V (blue solid); CC-Cη_{H_2} at -0.57V (red dotted) and -0.56V (green dashed); CC-Cη_{O_2} at 0.48V (black dash-dotted) and 0.49V (magenta).

gradually decays. The cell voltage comes back to 2.401V at $I = 0.4A$, very close to CV case with slightly less gassing and better charging efficiency. If we push the η_{O_2} control limits back to 0.48V (black), the max voltage is now around 2.4V but it falls to a much lower value when η_{O_2} is held. The ending SOC is lower, too. The return is shorter test time, even less gassing and further improved charge efficiency. Note that in all 5 cases, both interfacial area and exchange current for oxygen is much lower than those for hydrogen, but the η_{O_2} which directly controls oxygen generation is still more influence. Hence, if choose minimum current as the ending condition for floating charge, control η_{O_2} will be a better choice than η_{H_2}.

Figures 6.12, 6.13, and 6.14 plot all the charges based on pressures vs cell voltage/potentials. In the plots, when the floating charge current hits 0.4A, the CC-Cη_p cases (green markers) appear in the left bottom which means in general, they yield less

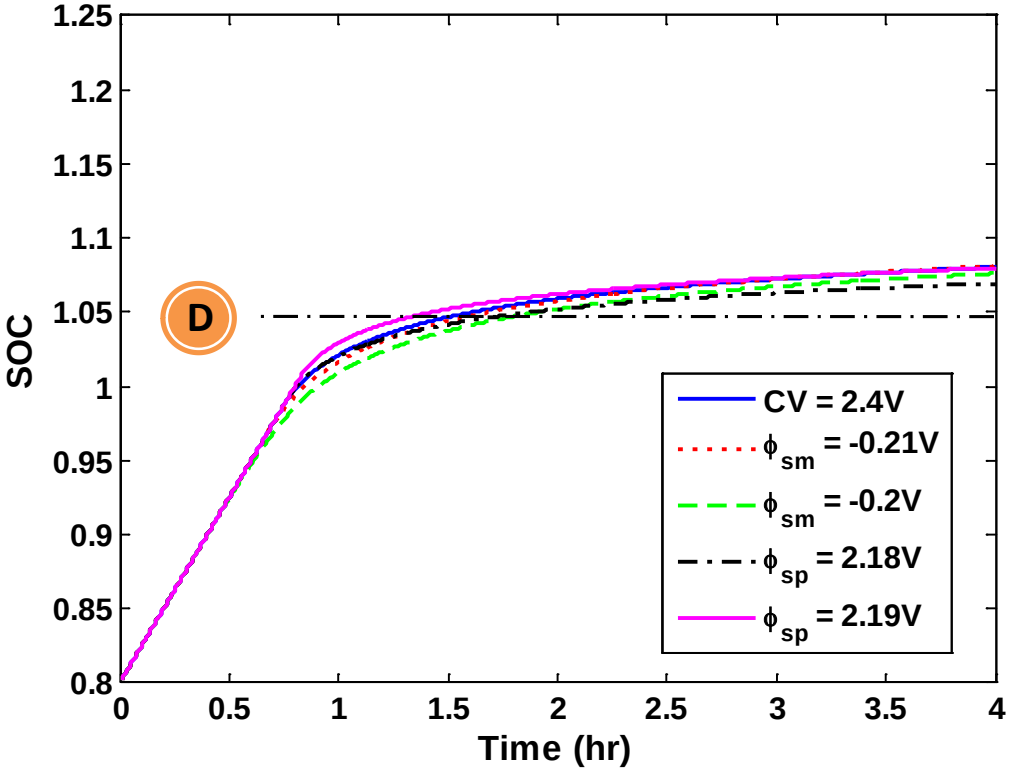

Figure 6.9. Current-counting-based SOC estimation during charge protocols: CC-CV at 2.4V (blue solid); CC-Cη_{H_2} at -0.57V (red dotted) and -0.56V (green dashed); CC-Cη_{O_2} at 0.48V (black dash-dotted) and 0.49V (magenta).

pressure generation than CC-CV and CC-Cη_m cases. Therefore, in the scenario, CC-Cη_p is the best control choice.

6.2.2.2 Case B: Same charging time

If choose to end the tests after 4-hour charging ("B" in Fig. 6.6), the cell states are shown in Table 6.2.

Given the same charge time, Cη_{O_2} at 0.48V (black) yields the least gassing and best charging efficiency. As a trade-off, its end cell voltage is the lowest. If increase the control limit to 0.49V (magenta), gassing will be largely promoted, lowering the efficiency. Both charges appear to be more efficient than CV at 2.4V (blue). The least efficient one is Cη_{H_2} at -0.57V (red) which has the highest ending current as expected,

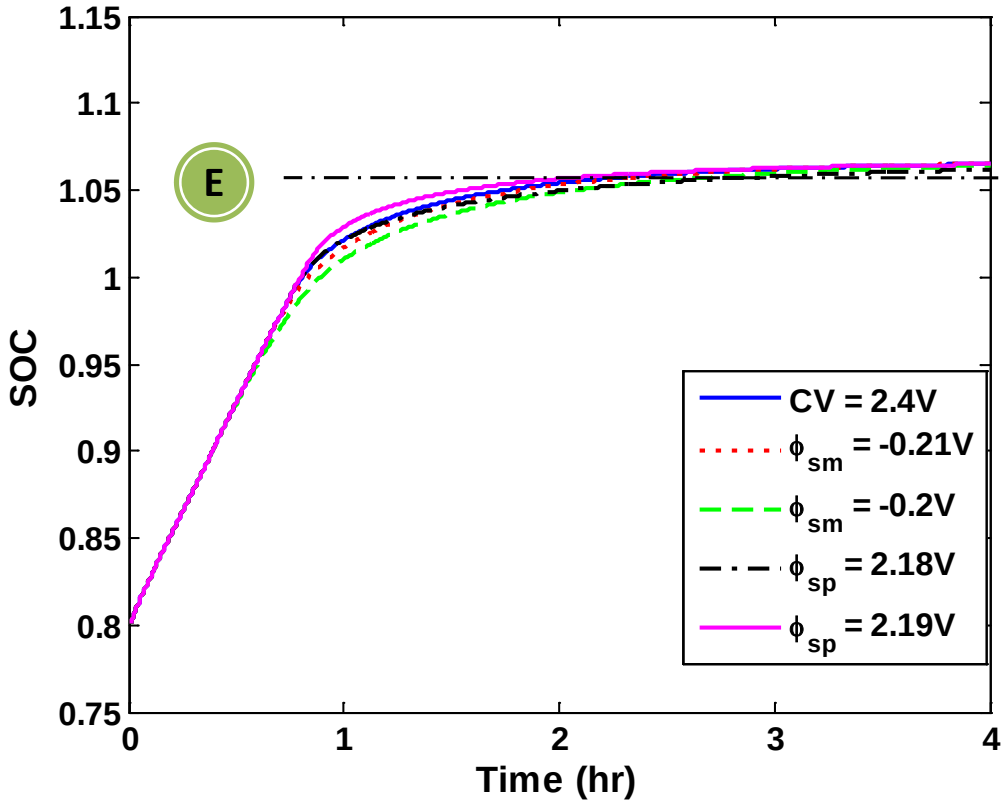

Figure 6.10. Internal-acid-based SOC estimation during charge protocols: CC-CV at 2.4V (blue solid); CC-Cη_{H_2} at -0.57V (red dotted) and -0.56V (green dashed); CC-Cη_{O_2} at 0.48V (black dash-dotted) and 0.49V (magenta).

and the highest cell voltage also. To make it more efficient and faster, one can push the control limit to -0.56V (green), which will significantly suppress gas generation and improve efficiency. From the results, gassing and ending voltage seem to be really sensitive to η control limits, especially η_{O_2}. Therefore, controlling Cη_{O_2} will be more robust if the sensing or estimation of η has large noise.

Figures 6.15, 6.16, and 6.17 plot all the charges based on pressures vs cell voltage/potentials. In the plots, when the tests are terminated at 4 hrs, the CC-Cη_m cases, in general, result in less gassing compared to CC-CV and CC-Cη_{H_2} charge (red dots are generally lower than green and blue markers). Therefore, in the scenario, CC-Cη_{H_2} is the best control choice.

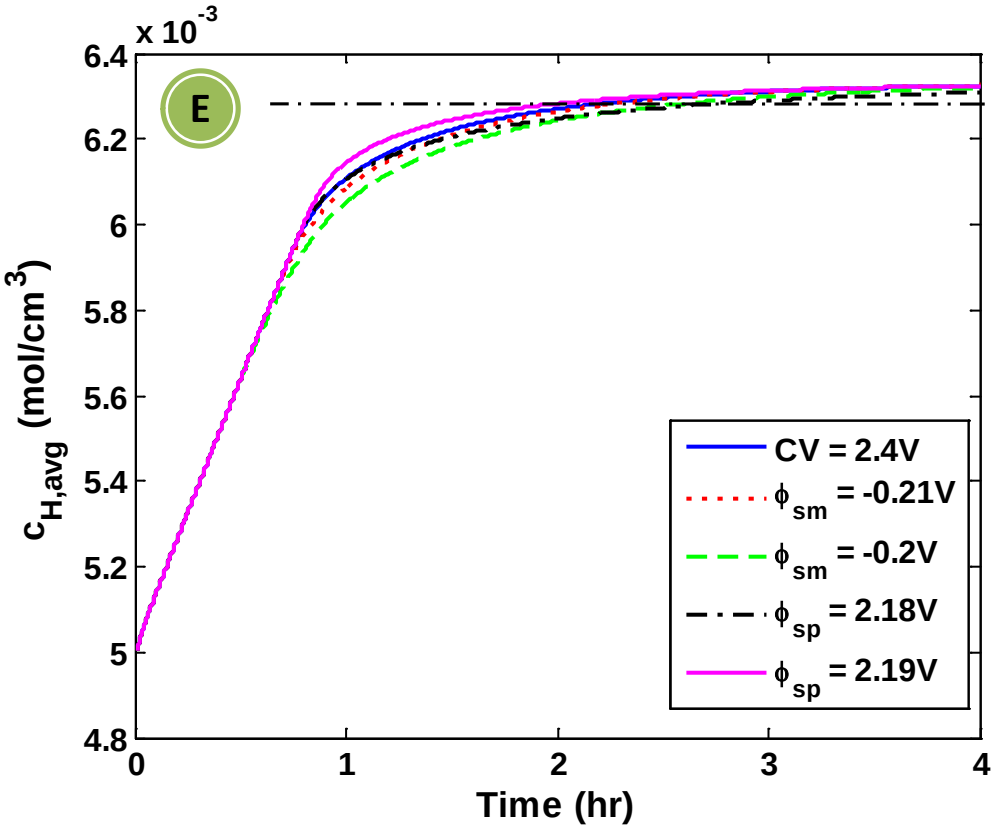

Figure 6.11. Scheme of the experimental setup

Table 6.1. Case comparison - Same ending current

Charging Protocol	Time (hr)	I (A)	V_{cell} (V)	η_{O_2} (V)	η_{H_2} (V)	P (psi)	SOC_1 (%)	SOC_2 (%)	Efficiency (%)
CV @ $2.4V$	2.952	0.4	2.400	2.191	-0.209	9.339	107.2	106.2	99.09
$C\eta_{H_2}$ @ $-0.21V$	3.149	0.4	2.403	2.193	-0.210	9.839	107.4	106.3	98.96
$C\eta_{H_2}$ @ $-0.20V$	3.183	0.4	2.388	2.188	-0.200	7.646	106.9	106.1	99.21
$C\eta_{O_2}$ @ $2.18V$	2.598	0.4	2.368	2.180	-0.188	5.557	105.9	105.5	99.62
$C\eta_{O_2}$ @ $2.19V$	2.586	0.4	2.401	2.190	-0.211	9.180	106.9	106.1	99.21

6.2.2.3 Case C: Same gas production

One can also use gas generation as the terminating condition (”C” in Fig. 6.8). Table 6.3 lists the cell variables at $P = 5$ *psi*.

Gas production on each electrode is controlled by the overpotentials and solid-phase potentials of the electrode is linear with the overpotential of that electrode. To suppress

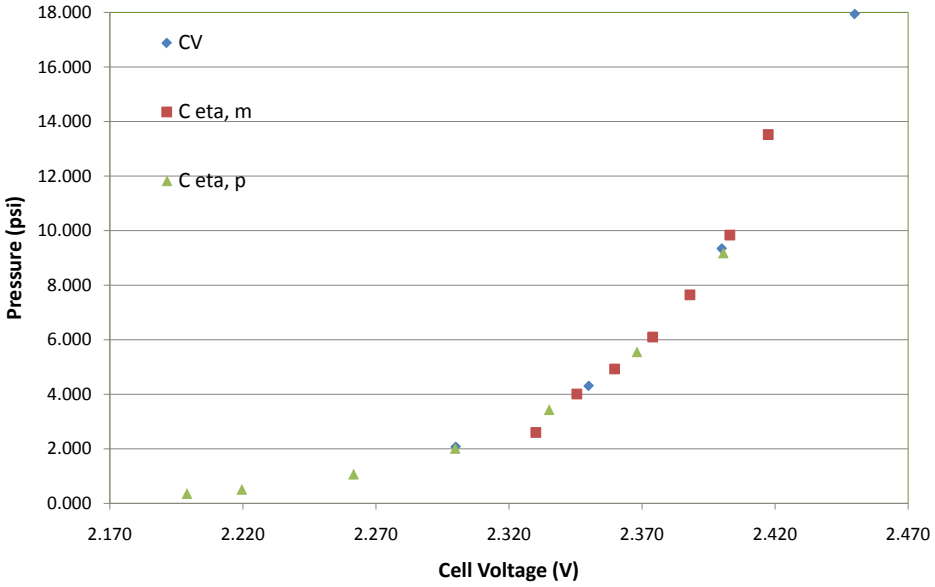

Figure 6.12. CC-Cη_{O_2} (green) vs CC-Cη_{H_2} (red) vs CC-CV (blue)

Table 6.2. Case comparison - Same charging time

Charging Protocol	Time (hr)	I (A)	V_{cell} (V)	η_{O_2} (V)	η_{H_2} (V)	P (psi)	SOC_1 (%)	SOC_2 (%)	Efficiency (%)
CV @ $2.4V$	4	0.288	2.400	2.193	-0.207	14.418	108.1	106.5	98.57
$C\eta_{H_2}$ @ $-0.21V$	4	0.310	2.404	2.194	-0.210	14.275	108.1	106.5	98.50
$C\eta_{H_2}$ @ $-0.20V$	4	0.290	2.390	2.190	-0.200	10.956	107.6	106.4	98.86
$C\eta_{O_2}$ @ $2.18V$	4	0.209	2.361	2.180	-0.181	9.178	106.9	106.2	99.29
$C\eta_{O_2}$ @ $2.19V$	4	0.238	2.393	2.190	-0.204	15.538	108.0	106.5	98.60

gassing, one can try to keep overpotentials low, i.e., keeping overpotentials close to zero. Thus, in Table 6.3, it shows that lower η_{O_2} and higher η_{H_2} charge protocols reach 5 psi the latest with lower charging current and cell voltage at the time. Comparing η_{H_2} at -0.57V and η_{O_2} at 0.49V, the latter has more gassing which agrees with what is concluded in previous cases that gassing is more sensitive to $\phi_{s,p}$.

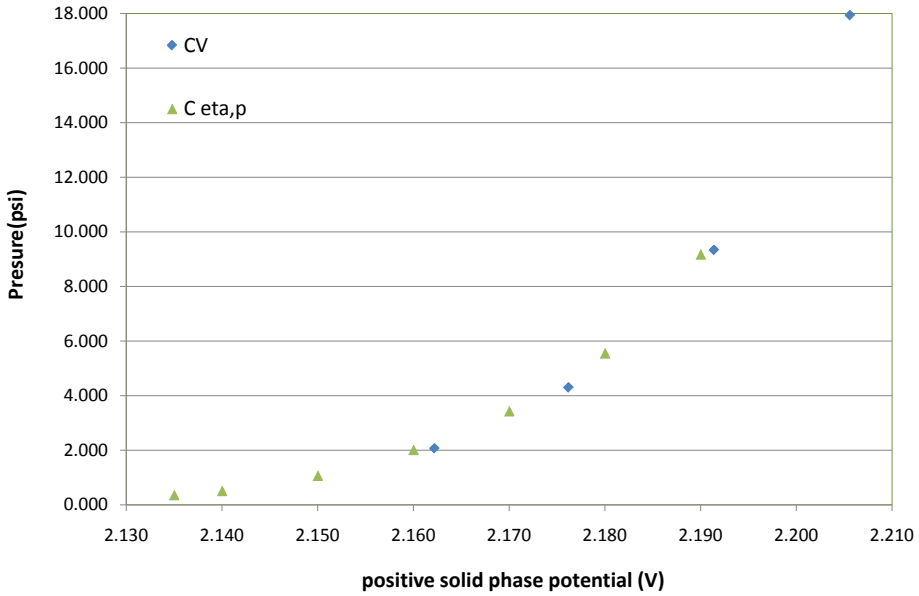

Figure 6.13. CC-Cη_{O_2} (green) vs CC-CV (blue)

Table 6.3. Case comparison - Same gas production

Charging Protocol	Time (hr)	I (A)	V_{cell} (V)	η_{O_2} (V)	η_{H_2} (V)	P (psi)	SOC_1 (%)	SOC_2 (%)	Efficiency (%)
CV @ $2.4V$	2.005	0.753	2.400	2.189	-0.211	5	105.9	105.4	99.53
$C\eta_{H_2}$ @ $-0.21V$	2.129	0.750	2.400	2.190	-0.210	5	106.0	105.5	99.48
$C\eta_{H_2}$ @ $-0.20V$	2.480	0.604	2.386	2.186	-0.200	5	106.1	105.5	99.50
$C\eta_{O_2}$ @ $2.18V$	2.390	0.460	2.370	2.180	-0.190	5	105.7	105.7	100.00
$C\eta_{O_2}$ @ $2.19V$	1.709	0.829	2.409	2.190	-0.219	5	105.7	105.3	99.60

6.2.2.4 Case D: Same overcharge

Table 6.4 shows the results if cut off the charge when a lead-acid cell is overcharged to 106% SOC.

In this scenario, the five end SOC_2's and the efficiencies are very close . The two Cη_{O_2} charge protocols gas more than the two Cη_{H_2} charges. Among them, Cη_{H_2} at -0.47V achieves the same voltage and potentials as CV at 2.4V with less gassing but longer time. Cη_{O_2} at 2.19V yields the most gassing and it reaches 6% overcharge the

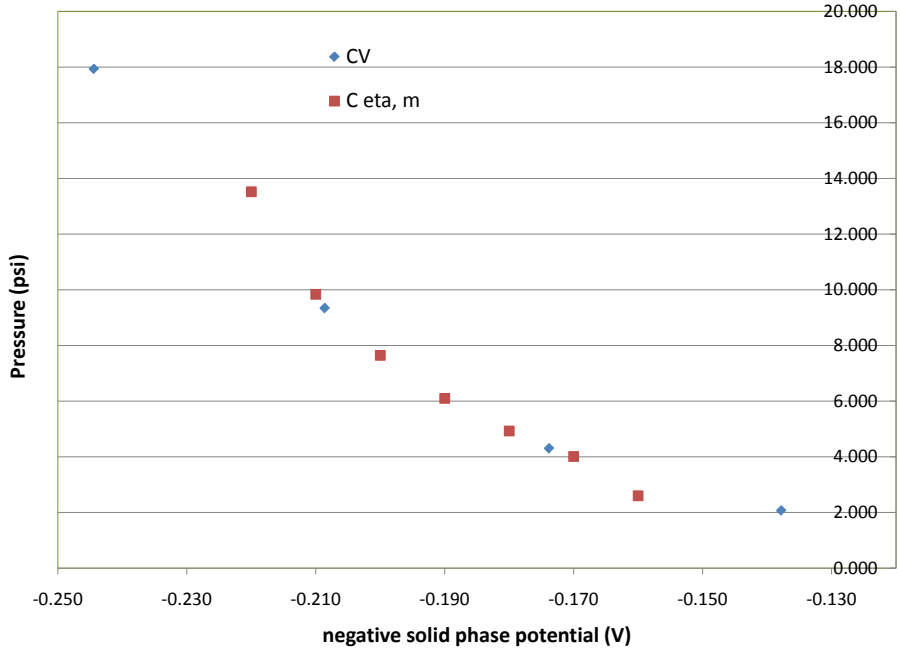

Figure 6.14. CC-Cη_{H_2} (red) vs CC-CV (blue)

Table 6.4. Case comparison - Same overcharge

Charging Protocol	Time (hr)	I (A)	V_{cell} (V)	η_{O_2} (V)	η_{H_2} (V)	P (psi)	SOC_1 (%)	SOC_2 (%)	Efficiency (%)
CV @ $2.4V$	2.056	0.720	2.400	2.189	-0.211	5.223	106.0	105.5	99.49
$C\eta_{H_2}$ @ $-0.21V$	2.119	0.756	2.400	2.190	-0.210	4.954	106.0	105.5	99.49
$C\eta_{H_2}$ @ $-0.20V$	2.438	0.623	2.386	2.186	-0.200	4.851	106.0	105.5	99.51
$C\eta_{O_2}$ @ $2.18V$	2.658	0.386	2.368	2.180	-0.188	5.717	106.0	105.6	99.60
$C\eta_{O_2}$ @ $2.19V$	1.867	0.697	2.407	2.190 -	0.217	5.773	106.0	105.5	99.53

fastest while it takes much longer for Cη_{O_2} at 0.48V to absorb 6% overcharge. CV at 2.4V is second fastest to reach 6% overcharge. In this case, η_{H_2} is playing a more critical role in controlling gassing and charge speed given the same overcharge which is probably due to that the transfer current for hydrogen is large than that for oxygen.

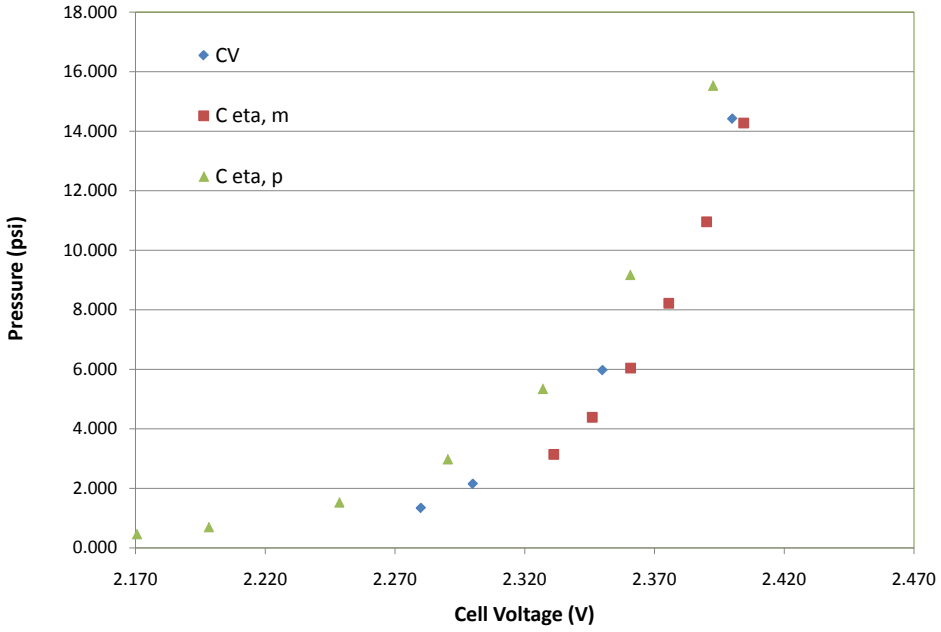

Figure 6.15. CC-Cη_{O_2} (green) vs CC-Cη_{H_2} (red) vs CC-CV (blue)

6.2.2.5 Case E: Same acid concentration level

Besides overcharge, alternative terminating condition can be internal acid concentration level, which represent how much acid has been restored, i.e., how much energy that actually gets turned into cell capacity. If 106% SOC_2 (equivalent to $6.3d - 3mol/cm^3$) is the ending criteria (”E” in Figs. 6.10 and 6.11), the results are detailed in Table 6.5

Table 6.5. Case comparison - Same acid concentration level

Charging Protocol	Time (hr)	I (A)	V_{cell} (V)	η_{O_2} (V)	η_{H_2} (V)	P (psi)	SOC_1 (%)	SOC_2 (%)	Efficiency (%)
CV @ $2.4V$	2.606	0.482	2.400	2.191	-0.209	7.716	106.8	106	99.24
$C\eta_{H_2}$ @ $-0.21V$	2.657	0.514	2.402	2.192	-0.210	7.426	106.8	106	99.22
$C\eta_{H_2}$ @ $-0.20V$	3.046	0.429	2.388	2.188	-0.200	7.110	106.8	106	99.27
$C\eta_{O_2}$ @ $2.18V$	3.458	0.257	2.363	2.180	-0.183	7.805	106.6	106	99.41
$C\eta_{O_2}$ @ $2.19V$	2.433	0.440	2.402	2.190	-0.212	8.468	106.8	106	99.27

To achieve 6% overcharge based on acid concentration level, it takes the longest time to charge a lead-acid cell using Cη_{O_2} at 0.48V. The reward is the least input energy, i.e.,

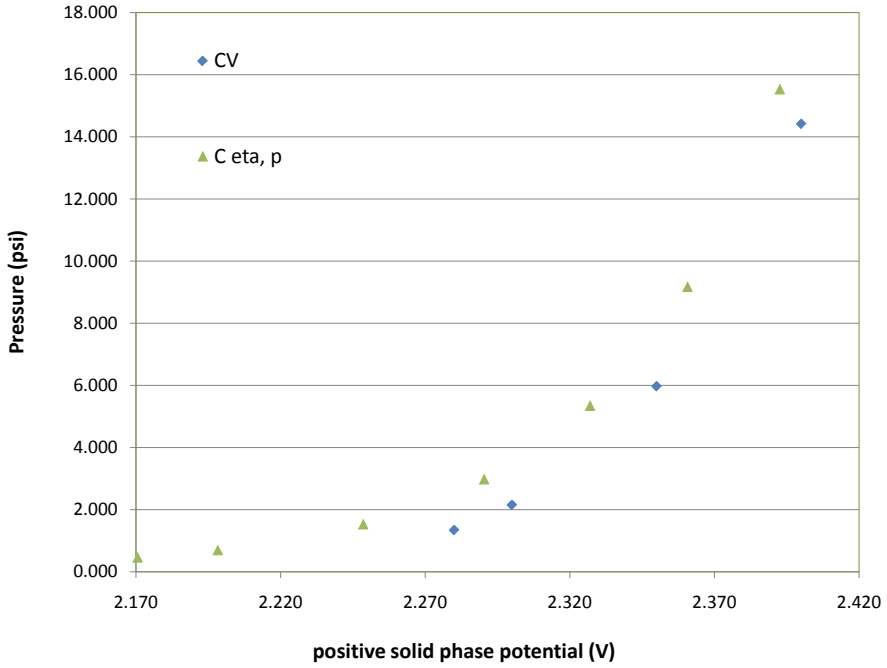

Figure 6.16. CC-Cη_{O_2} (green) vs CC-CV (blue)

best conversion from electrical energy to chemical energy. The runner-up is to charge at $\eta_{H_2} = -0.56V$. Also they are the two with lowest end current and gas production. This is because both have tighter constraints on gassing. When a lead-acid cell gets close to full charge, its primary reactions slow down and show higher resistance to input energy while its side reactions start becoming energetic. If limiting side reactions, the current cannot flood into either primary reactions or side reactions but be reduced, prolonging the charge time in this case. Hence, if charge time is not too big a concern, using CC-Cη charge will lead to high charge efficiency if holding the potential close to zero.

6.3 Conclusions

In this work, a new charging strategy, constant-current constant-overpotential, is proposed. Compared with the conventional constant-current constant-voltage charge protocol, CC-Cη is shown to have better control over gassing during overcharge, which improves charging efficiency. Also, a SOC estimation based on internal acid concen-

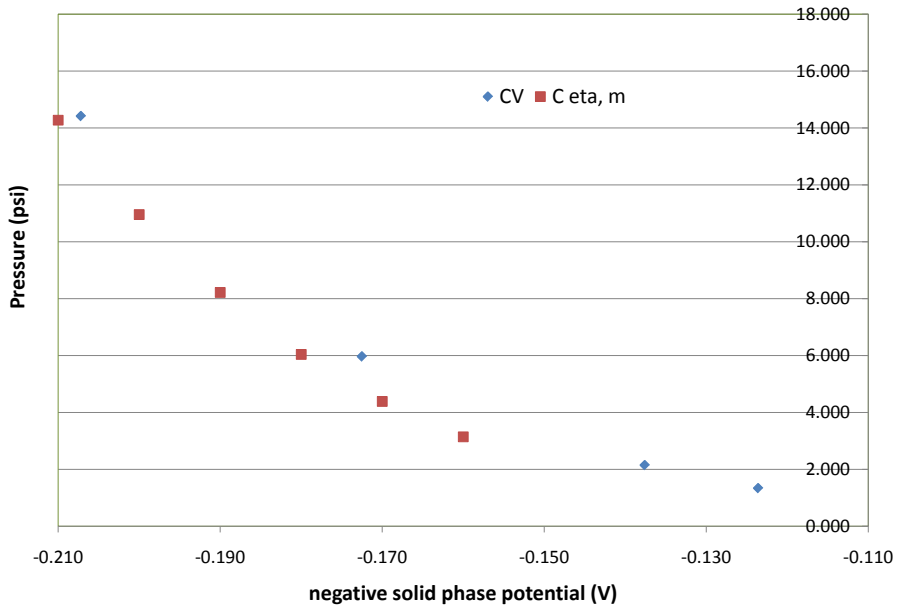

Figure 6.17. CC-Cη_{H_2} (red) vs CC-CV (blue)

tration is adopted. This method overcomes the drawbacks that a current-counting-based SOC estimator has in high SOC region, which turns out to be a better choice during overcharge. There are two variations of CC-Cη, controlling positive overpotential and controlling negative overpotential. Case study compares these two charging protocols with CC-CV charging under different charge ending condition. The results suggest

- if choose minimum current as the ending condition for floating charge, η_{O_2} is the best control choice;
- if given same charging time, gassing and ending voltage seem to be really sensitive to η control limits, especially η_{O_2}. If charging time is the termination condition, controlling η_{H_2} yields less gassing;
- if cap the gas production, the lower the holding voltages/potentials, the less gas generation;
- if limit the input energy, η_{H_2} has more impact than η_{O_2};

- if time is not the major concern, using CC-Cη charge and tightly constrain η will lead to high charge efficiency.

Chapter 7

Conclusions and Future Work

7.1 Conclusions

The ultimate goal of this research is to develop hardware and software for intelligent battery management system, which can monitor pack's condition, calculate/estimate crucial states such as state of charge and state of health, predict the future performance, adjust cells use, prevent thermal runaway and other safety issues, maintain pack's service lives, and optimize the overall pack performance and cost. In the present work, modeling and experiment techniques have been studied separately. Discretization modeling methods as promising candidates for developing simple but accurate models that are suitable for BMS are investigated and compared. Each has its distinct pros and cons. Padé and FDM are the most and the least efficient, respectively. But Padé only applies to systems that are analytical and differentiable. FDM is the simplest in math to implement. Ritz is a good trade-off since it is quite efficient and easy to use. On the other hand, a nondestructive aging diagnosis method has been developed for VRLA batteries and alongside, a battery testing station has been designed and built, which integrates programmable amplifier, dSPACE/ControlDesk, sensors, and Matlab/Simulink. The diagnosis method is demonstrated to identify water loss and hard sulfation in aged lead-acid cells by loading the cells with different current profiles and analyzing their voltage and pressure responses. It provides a non-intrusive real-time aging detection tool with minimum sensor placement which can be easily integrated into a BMS. Furthermore, the hardware can be extended to function as a desulfator with changes in the charge algorithm. A desulfation charge control is implemented which adaptively ad-

just the charge current to restore cell capacity in the shortest time and avoid excessive gassing during overcharge. On the sulfated cell, a desulfation charge control succeeds to remove hard sulfation and recover its capacity, which also pumps up the capacity of the entire string. Nevertheless, it is very costly to have pressure sensors installed on each cell in a lead-acid battery. An alternative is to have a system model for charge/overcharge which predicts gassing based on the cell initial conditions and applied current. This work presents a nonlinear 5th-order state space model including degradation for lead-acid cells. It is based on the electrochemical processes and adopts parameters of the underlying fundamental PDE model. The model is validated with testing data. The results show that the model accurately captures the voltage and the pressure responses during charge and overcharge. Besides, it also captures the potentials, reaction current densities, and gassing responses observed in the fundamental model, making it well suited for model-based analysis, simulation, estimation, and BMS design. After forming the electrolysis-included system model, a charging strategy, constant-current constant-overpotential, is proposed. Compared with the conventional constant-current constant-voltage charge (CC-CV) protocol, CC-Cη is shown to have better control over gassing during overcharge, which is health-cautious and improves charging efficiency. Also, a SOC estimator based on internal acid concentration is adopted. This method overcomes the drawbacks that a current-counting-based SOC estimator has in high SOC region, which turns out to be a better choice during overcharge. There are two variations of CC-Cη charge protocol, controlling positive overpotential and controlling negative overpotential. Case study compares these two charging protocols with CC-CV charging under different charge ending condition. The comparison results suggest

- if choose minimum current as the ending condition for floating charge, η_{O_2} is the best control choice;
- if given same charging time, gassing and ending voltage seem to be really sensitive to η control limits, especially η_{O_2}. If charging time is the termination condition, controlling η_{H_2} yields less gassing;
- if cap the gas production, the lower the holding voltages/potentials, the less gas generation;
- if limit the input energy, η_{H_2} has more impact than $\phi_{s,p}$;

- if time is not the major concern, using CC-Cη charge and tightly constrain η will lead to high charge efficiency.

7.2 Future Work

7.2.1 Modeling and Control

We have shown in the current work that constant-current constant-overpotential charge has the potential to be more health cautious and efficient than constant-current constant voltage charge. However, η_{H_2} and η_{O_2} are difficult to be directly measured online. Therefore, to apply the CC-Cη charge in real time, state estimators needs to be designed and adjusted as the cell aged. And, the algorithm needs to be validated using the battery testing station. The desulfation charge has been shown to work on sulfated cells. But the mechanism is still unclear which warrants further study.

Fast charge is another area to explore with the nonlinear degradation-included model. Optimization tools can be adopted to design control policies that balances the charge time and charge efficiency/gassing. Given the knowledge of when gas production really gets energetic, one can apply as large a current as a cell can accept, say 5C, to recharge the cell in a short time and stop just before the side reactions kick in; then switch to floating charge mode with controlled η.

Cell balancing during floating charge will be another interesting topic using CC-Cη charge. When a lead-acid battery pack ages, the cells might have a wide spread of state of health. The state-of-art cell balancing strategies often balance the cells to the same voltage to give them a uniform discharge power. By doing this with CC-CV charge, the cells with lower voltages get more charge which might also have more gassing along the charge and gets dried out earlier. Replacing the balancing charge with CC-Cη will reduce the age caused during floating charge and maximize the restored capacity to give the overall pack better power/energy and service life.

7.2.2 Real-time Degradation and Cell Balancing

The battery testing station built for real-time aging diagnosis and remediation has many advantages. It can perform multiple tests in one set with high precision and a lot of flexi-

bility. It can implement control algorithms with different types of sensing and feedback. Its voltage range makes it capable of testing many battery chemistries, such as Li-ion, NiMH, lead-acid, etc. The current version only have one channel but can be easily expanded to two channels with just a duplicate of the circuit boards. If more channels are needed, an external power supply needs to be added and the amplifier built-in can function as a secondary power source for small current like floating charge.

We show in the current work that using the battery test station, we can perform real-time aging diagnosis on lead-acid cells. This feature enables us to perform cell balancing based on cell's State of Health (SOH) instead of cell voltages/State of Charge (SOC). Cell balancing based on cell voltages/SOC gives a uniformed distribution of cell voltages and maximizes the available discharge power; while cell balancing based on SOH focuses more on maximizing the available energy. In a string pack, the overall capacity is dictated by the weakest cell. So cell balancing based on SOH will benefit the pack's service life by keeping the cell capacity distribution tight.

Bibliography

[1] LAM, L., J. DOUGLAS, R. PILLIG, and D. RAND (1994) "Minor elements in lead materials used for lead/acid batteries 1. Hydrogen- and oxygen-gassing characteristics," *Journal of Power Sources*, **48**(1 - 2), pp. 219 – 232.

[2] BODE, H. (1977) *Lead-acid batteries*, Wiley.

[3] CULPIN, B. and D. RAND (1991) "Failure modes of lead/acid batteries," *Journal of Power Sources*, **36**(4), pp. 415 – 438.

[4] HOLLENKAMP, A. (1996) "When is capacity loss in lead/acid batteries 'premature'?" *Journal of Power Sources*, **59**(1-2), pp. 87 – 98.

[5] RAND, D. (1997) "The lead/acid battery, a key technology for global energy management," *Journal of Power Sources*, **64**, pp. 157–174.

[6] SCHIFFER, J., D. U. SAUER, H. BINDNER, T. CRONIN, P. LUNDSAGER, and R. KAISER (2007) "Model prediction for ranking lead-acid batteries according to expected lifetime in renewable energy systems and autonomous power-supply systems," *Journal of Power Sources*, **168**(1), pp. 66 – 78.

[7] BINDNER, H., T. CRONIN, P. LUNDSAGER, J. MANWELL, U. ABDULWAHID, and I. BARING-GOULD (2005) *Lifetime Modelling of Lead Acid Batteries*, *Tech. Rep. Risø-R-1515(EN)*, RisøNational Laboratory, Denmark.

[8] RUETSCHI, P. (2004) "Aging mechanisms and service life of lead-acid batteries," *Journal of Power Sources*, **127**(1-2), pp. 33 – 44.

[9] COOPER, A. and P. MOSELEY (2003) "Progress in overcoming the failure modes peculiar to VRLA batteries," *Journal of Power Sources*, **113**(2), pp. 200 – 208.

[10] MOSELEY, P. (2000) "Improving the valve-regulated lead-acid battery," *Journal of Power Sources*, **88**(1), pp. 71 – 77.

[11] J.NEWMAN (1991) *Electrochemical Systems*, 2 ed., Prentice Hall, Englewood Cliffs, NJ.

[12] GU, W. and C. WANG (1997) "Numerical Modeling of the Coupled Electrochemical and Transport Processes in Lead-Acid Batteries," *Journal of Power Sources*, **144**(6).

[13] APPEL, P. W., D. B. EDWARDS, and T. STALICK (1993) "Modeling the effects of electrolyte diffusion and paste conductivity on lead/acid battery performance," *Journal of Power Sources*, **46**(1), pp. 49 – 60.

[14] FAN, D. and R. E. WHITE (1991) "A Mathematical Model of a Sealed Nickel-Cadmium Battery," *Journal of The Electrochemical Society*, **138**(1), pp. 17–25.

[15] GU, W. B., C. Y. WANG, and B. Y. LIAW (1998) "The use of computer simulation in the evaluation of electric vehicle batteries," *Journal of Power Sources*, **75**(1), pp. 151 – 161.

[16] VIDTS, P. D., J. DELGADO, and R. E. WHITE (1995) "Mathematical Modeling for the Discharge of a Metal Hydride Electrode," *Journal of The Electrochemical Society*, **142**(12), pp. 4006–4013.

[17] FULLER, T., M. DOYLE, and J. NEWMAN (1994) "Simulation and optimization of the dual lithium ion insertion cell," *Journal of the Electrochemical Society*, **141**, pp. 1–10.

[18] SMITH, K., C. RAHN, and C. WANG (2007) "Control Oriented 1D Electrochemical Model of Lithium Ion Battery," *Energy Conversion and Management*, **48**, pp. 2565–2578.

[19] GU, W. B. and C. Y. WANG (2000) "Thermal-Electrochemical Modeling of Battery Systems," *Journal of The Electrochemical Society*, **147**(8), pp. 2910–2922.

[20] PRINS-JANSEN, J. A., J. D. FEHRIBACH, K. HEMMES, and J. H. W. DE WIT (1996) "A Three-Phase Homogeneous Model for Porous Electrodes in Molten-Carbonate Fuel Cells," *Journal of The Electrochemical Society*, **143**(5), pp. 1617–1628.

[21] MUKHERJEE, P. P., C.-Y. WANG, and Q. KANG (2009) "Mesoscopic modeling of two-phase behavior and flooding phenomena in polymer electrolyte fuel cells," *Electrochimica Acta*, **54**(27), pp. 6861 – 6875.

[22] DURR, M., A. CRUDEN, S. GAIR, and J. MCDONALD (2006) "Dynamic model of a lead acid battery for use in a domestic fuel cell system," *Journal of Power Sources*, **161**.

[23] SALAMEH, Z., M. CASACCA, and W. LYNCH (1992) "A mathematical model for lead-acid batteries," *Energy Conversion, IEEE Transactions on*, **7**(1), pp. 93 –98.

[24] GIBSON, I. and K. PETERS (1982) "Sulphation in discharged lead-acid batteries," *Journal of Power Sources*, **8**(2), pp. 143 – 157.

[25] YAMAGUCHI, Y., M. SHIOTA, Y. NAKAYAMA, N. HIRAI, and S. HARA (2000) "In situ analysis of electrochemical reactions at a lead surface in sulfuric acid solution," *Journal of Power Sources*, **85**(1), pp. 22 – 28.

[26] TAKEHARA, Z. (2000) "Dissolution and precipitation reactions of lead sulfate in positive and negative electrodes in lead acid battery," *Journal of Power Sources*, **85**(1), pp. 29 – 37.

[27] SCHAECK, S., T. KARSPECK, C. OTT, M. WECKLER, and A. STOERMER (2011) "A field operational test on valve-regulated lead-acid absorbent-glass-mat batteries in micro-hybrid electric vehicles. Part I. Results based on kernel density estimation," *Journal of Power Sources*, **196**(5), pp. 2924 – 2932.

[28] SCHAECK, S., T. KARSPECK, C. OTT, D. WEIRATHER-KOESTNER, and A. STOERMER (2011) "A field operational test on valve-regulated lead-acid absorbent-glass-mat batteries in micro-hybrid electric vehicles. Part II. Results based on multiple regression analysis and tear-down analysis," *Journal of Power Sources*, **196**(5), pp. 2933 – 2938.

[29] PILLER, S., M. PERRIN, and A. JOSSEN (2001) "Methods for state-of-charge determination and their applications," *Journal of Power Sources*, **96**(1), pp. 113 – 120.

[30] BHANGU, B., P. BENTLEY, D. STONE, and C. BINGHAM (2005) "Nonlinear observers for predicting state-of-charge and state-of-health of lead-acid batteries for hybrid-electric vehicles," *Vehicular Technology, IEEE Transactions on*, **54**(3), pp. 783 – 794.

[31] GOULD, C., C. BINGHAM, D. STONE, and P. BENTLEY (2009) "New Battery Model and State-of-Health Determination Through Subspace Parameter Estimation and State-Observer Techniques," *Vehicular Technology, IEEE Transactions on*, **58**(8), pp. 3905 –3916.

[32] FAIRWEATHER, A., M. FOSTER, and D. STONE (2011) "Battery parameter identification with Pseudo Random Binary Sequence excitation (PRBS)," *Journal of Power Sources*, **196**(22), pp. 9398 – 9406.

[33] VISWANATHAN, V. V., A. J. SALKIND, J. J. KELLEY, and J. B. OCKERMAN (1995) "Effect of state of charge on impedance spectrum of sealed cells Part II: Lead acid batteries," *Journal of Applied Electrochemistry*, **25**, pp. 729–739.

[34] THELE, M., E. KARDEN, E. SUREWAARD, and D. SAUER (2006) "Impedance-based overcharging and gassing model for VRLA/AGM batteries," *Journal of Power Sources*, **158**(2), pp. 953 – 963.

[35] LAM, L., N. HAIGH, C. PHYLAND, and A. URBAN (2004) "Failure mode of valve-regulated lead-acid batteries under high-rate partial-state-of-charge operation," *Journal of Power Sources*, **133**(1), pp. 126 – 134.

[36] MOSELEY, P. T. (2004) "High rate partial-state-of-charge operation of VRLA batteries," *Journal of Power Sources*, **127**(1-2), pp. 27 – 32.

[37] LAMBERT, D., P. GREENWOOD, and M. REED (2002) "Advances in gelled-electrolyte technology for valve-regulated lead-acid batteries," *Journal of Power Sources*, **107**(2), pp. 173 – 179.

[38] (2008), "IEEE Guide for Optimizing the Performance and Life of Lead-Acid Batteries in Remote Hybrid Power Systems," IEEE Std 1561-2007.

[39] CATHERINO, H. A., F. F. FERES, and F. TRINIDAD (2004) "Sulfation in lead-acid batteries," *Journal of Power Sources*, **129**(1), pp. 113 – 120.

[40] MATTERA, F., D. BENCHETRITE, D. DESMETTRE, J. MARTIN, and E. POTTEAU (2003) "Irreversible sulphation in photovoltaic batteries," *Journal of Power Sources*, **116**(1-2), pp. 248 – 256.

[41] HUND, T., "Capacity Loss in PV Batteries and Recovery Procedures," Photovoltaic System Applications Department, Sandia National Laboratories.

[42] APATEANU, L., A. HOLLENKAMP, and M. KOOP (1993) "Electrolyte stratification in lead/acid batteries: Effect of grid antimony and relationship to capacity loss," *Journal of Power Sources*, **46**(2-3), pp. 239 – 250.

[43] PETKOVA, G., P. NIKOLOV, and D. PAVLOV (2006) "Influence of polymer additive on the performance of lead-acid battery negative plates," *Journal of Power Sources*, **158**(2), pp. 841 – 845.

[44] PAVLOV, D. (2011) *Lead-Acid Batteries: Science and Technology*, Elsevier Science.

[45] PAVLOV, D., P. NIKOLOV, and T. ROGACHEV (2010) "Influence of expander components on the processes at the negative plates of lead-acid cells on high-rate partial-state-of-charge cycling. Part I: Effect of lignosulfonates and BaSO4 on the processes of charge and discharge of negative plates," *Journal of Power Sources*, **195**(14), pp. 4435 – 4443.

[46] ——— (2010) "Influence of expander components on the processes at the negative plates of lead-acid cells on high-rate partial-state-of-charge cycling. Part II. Effect of carbon additives on the processes of charge and discharge of negative plates," *Journal of Power Sources*, **195**(14), pp. 4444 – 4457.

[47] BUIEL, E., E. DICKINSON, A. STOERMER, and S. SCHAECK (2012), "Dynamic Charge Acceptance of Lead Acid Batteries in Micro Hybrid Board Net," 12th European Lead Battery Conference.

[48] YANG, Z., J. ZHANG, M. C. W. KINTNER-MEYER, X. LU, D. CHOI, J. P. LEMMON, and J. LIU (2011) "Electrochemical Energy Storage for Green Grid," *Chemical Reviews*, **111**(5), pp. 3577–3613.

[49] LAM, L., N. HAIGH, C. PHYLAND, and T. HUYNH (2005) "Novel technique to ensure battery reliability in 42-V PowerNets for new-generation automobiles," *Journal of Power Sources*, **144**(2), pp. 552 – 559.

[50] NELSON, R., E. SEXTON, J. OLSON, M. KEYSER, and A. PESARAN (2000) "Search for an optimized cyclic charging algorithm for valve-regulated leadacid batteries," *Journal of Power Sources*, **88**(1), pp. 44 – 52.

[51] LAM, L., H. OZGUN, O. LIM, J. HAMILTON, L. VU, D. VELLA, and D. RAND (1995) "Pulsed-current charging of lead/acid batteries - a possible means for overcoming premature capacity loss?" *Journal of Power Sources*, **53**, pp. 215 – 228.

[52] KEYSER, M., A. PESARAN, M. MIHALIC, and B. NELSON (2000), "Charging Algorithms for Increasing Lead Acid Battery Cycle Life for Electric Vehicles," the 17th Electric Vehicle Symposium.

[53] TIEDEMANN, W. and J. NEWMAN (1979) "Mathematical Modeling of the Lead-Acid Cell," in *The Electrochemical Society Softbound Proceedings Series*, Pennington, NJ, p. 23.

[54] GU, H., T. V. NGUYEN, and R. WHITE (1987) "A Mathematical Model of a Lead-Acid Cell," *Journal of Power Sources*, **134**.

[55] CATHERINO, H., J. BURGEL, A. RUSEK, and F. FERES (1999) "Modelling and simulation of lead-acid battery charging," *Journal of Power Sources*, **80**.

[56] TENNO, A., R. TENNO, and T. SUNTIO (2001) "Charge/discharge behavior of VRLA batteries: model calibration and application for state estimation and failure detection," *Journal of Power Sources*, **103**(1), pp. 42 – 53.

[57] NEWMAN, J. and W. TIEDEMANN (1997) "Simulation of Recombinant Lead-Acid Batteries," *Journal of The Electrochemical Society*, **144**(9), pp. 3081–3091.

[58] BOSE, C. and N. HAMPSON (1987) "A review of oxygen recombination in the sealed lead-acid cell," *Journal of Power Sources*, **19**(1), pp. 261–267.

[59] DIMITROV, M. (1990) "Oxygen evolution on lead dioxide in sulphuric acid solutions," *Journal of Power Sources*, **31**(1-4), pp. 121 – 124.

[60] BERNARDI, D. M. and M. K. CARPENTER (1995) "A Mathematical Model of the Oxygen-Recombination Lead-Acid Cell," *Journal of The Electrochemical Society*, **142**(8), pp. 2631–2642.

[61] KIRCHEV, A., D. PAVLOV, and B. MONAHOV (2003) "Gas-diffusion approach to the kinetics of oxygen recombination in lead-acid batteries," *Journal of Power Sources*, **113**(2), pp. 245 – 254.

[62] BERNDT, D. (1997) *Maintenance-free Batteries:Lead-Acid, Nickel/Cadmium, Nickel/Metal Hydride*, Research Studies Press.

[63] TENNO, A., R. TENNO, and T. SUNTIO (2002) "Evaluation of VRLA battery under overcharging: model for battery testing," *Journal of Power Sources*, **111**(1), pp. 65 – 82.

[64] SRINIVASAN, V., G. WANG, and C. WANG (2003) "Mathematical Modeling of Current-Interrupt and Pulse Operation of Valve-Regulated Lead Acid Cells," *Journal of the Electochemical Society*, **150**(3).

[65] KARDEN, E., S. BULLER, and R. W. D. DONCKER (2002) "A frequency-domain approach to dynamical modeling of electrochemical power sources," *Electrochimica Acta*, **47**(13 - 14), pp. 2347 – 2356.

[66] HUET, F. (1998) "A review of impedance measurements for determination of the state-of-charge or state-of-health of secondary batteries," *Journal of Power Sources*, **70**(1), pp. 59 – 69.

[67] HAMMOUCHE, A., M. THELE, and D. U. SAUER (2006) "Analysis of gassing processes in a VRLA/spiral wound battery," *Journal of Power Sources*, **158**(2), pp. 987 – 990.

[68] CERAOLO, M. (2000) "New dynamical models of lead-acid batteries," *Power Systems, IEEE Transactions on*, **15**(4), pp. 1184 –1190.

[69] SAUER, D. U. (1997) "Modelling of local conditions in flooded lead/acid batteries in photovoltaic systems," *Journal of Power Sources*, **64**(1 - 2), pp. 181 – 187.

[70] FERNNDEZ, M. and F. TRINIDAD (1997) "Charging strategies for valve-regulated lead/acid batteries in electric-vehicle applications," *Journal of Power Sources*, **67**(1C2), pp. 125 – 133.

[71] NELSON, R. (1998) "Valve-regulated lead/acid battery designs and charging strategies łare they linked?" *Journal of Power Sources*, **73**(1), pp. 104 – 109.

[72] IKEYA, T., N. SAWADA, S. TAKAGI, J. ICHI MURAKAMI, K. KOBAYASHI, T. SAKABE, E. KOUSAKA, H. YOSHIOKA, S. KATO, M. YAMASHITA, H. NARISOKO, Y. MITA, K. NISHIYAMA, K. ADACHI, and K. ISHIHARA (1998) "Multi-step constant-current charging method for electric vehicle, valve-regulated, lead/acid batteries during night time for load-levelling," *Journal of Power Sources*, **75**(1), pp. 101 – 107.

[73] ——— (2000) "Charging operation with high energy efficiency for electric vehicle valve-regulated leadCacid battery system," *Journal of Power Sources*, **91**(2), pp. 130 – 136.

[74] SABERI, H. and F. SALMASI (2007) "Genetic optimization of charging current for lead-acid batteries in hybrid electric vehicles," in *Electrical Machines and Systems, 2007. ICEMS. International Conference on*, pp. 2028–2032.

[75] WILKINSON, J. and G. COVIC (1998) "A New Pulse Charging Methodology for Lead Acid Batteries," *Transactions of the Institution of Professional Engineers New Zealand: Electrical/Mechanical/Chemical Engineering Section*, **25**(1), pp. 1 – 11.

[76] MARCOS, J., J. DIOS, A. M. CAO, J. DOVAL, C. M. PENALVER, A. NOGUEIRAS, A. LAGO, and F. POZA (2006) "Fast lead-acid battery charge strategy," in *Applied Power Electronics Conference and Exposition, 2006. APEC '06. Twenty-First Annual IEEE*, pp. 4 pp.–.

[77] YANG, H., H. WANG, G. CHEN, and G. WU (2006) "Influence of the charge regulator strategy on state of charge and lifetime of {VRLA} battery in household photovoltaic systems," *Solar Energy*, **80**(3), pp. 281 – 287.

[78] SHI, Y., C. A. FERONE, and C. D. RAHN (2013) "Identification and remediation of sulfation in lead-acid batteries using cell voltage and pressure sensing," *Journal of Power Sources*, **221**(0), pp. 177 – 185.

[79] ARPACI, V. S. (1966) *Conduction Heat Transfer*, Addison-Wesley Publishing Co., Reading, MA.

[80] HILL, J. M. and J. N. DEWYNNE (1987) *Heat Conduction*, Blackwell Scientific Publications, Oxford.

[81] GEBHART, B. (1993) *Heat Conduction and Mass Diffusion*, McGraw-Hill, New York, NY.

[82] JACOBSEN, T. and K. WEST (1995) "Diffusion Impedance in Planar, Cylindrical, and Spherical Symmetry," *Electrochimica Acta*, **40**(2), pp. 255 – 262.

[83] SUBRAMANIAN, V. R., J. A. RITTER, and R. E. WHITE (2001) "Approximate Solutions for Galvanostatic Discharge of Spherical Particles," *Journal of the Electrochemical Society*, **148**(11), pp. E444–E449.

[84] SUBRAMANIAN, V. R., D. TAPRIYAL, and R. E. WHITE (2004) "A Boundary Condition for Porous Electrodes," *Electrochemical and Solid-State Letters*, **7**(9), pp. A259–A263.

[85] SANTHANAGOPALAN, S., Q. GUO, P. RAMADASS, and R. E. WHITE (2006) "Review of models for predicting the cycling performance of lithium ion batteries," *Journal of Power Sources*, **156**(2), pp. 620 – 628.

[86] G. A. BAKER AND P. GRAVES-MORRIS (1996) *Padé Approximants*, vol. 59 of *Encyclopedia of Mathematics and Its Applications*, 2 ed., Cambridge University Press, Cambridge.

[87] C. BREZINSKI AND M. REDIVO ZAGLIA (1991) *Extrapolation Methods. Theory and Practice*, North Holland.

[88] G. H. GOLUB AND C. F. VAN LOAN (1989) *Matrix Computations*, Johns Hopkins University Press, Baltimore.

[89] FORMAN, J. C., S. BASHASH, J. STEIN, and H. FATHY (2010) "Reduction of an Electrochemistry-Based Li-Ion Battery Health Degradation Model Via Constraint Linearization and Padé Approximation," in *DSCC2010-4084*, Boston, MA, pp. 173–183.

[90] REDDY, J. N. and D. K. GARTLING (2000) *The finite element method in heat transfer and fluid dynamics*, CRC Press, Ltd., Boca Raton, FL.

[91] YENER, Y. and S. KAKAC (2008) *Heat Conduction*, Taylor and Francis, New York, NY.

[92] CHANG, B.-Y. and S.-M. PARK (2010) "Electrochemical Impedance Spectroscopy," *Annual Review of Analytical Chemistry*, **3**(1), pp. 207–229.

[93] BERNDT, D. (1993) *Maintenance-free Batteries:Lead-Acid, Nickel Cadmium, Nickel Metal Hydride*, Research Studies Press.

[94] LEVERICH, C. G. (1992) "Switch Mode Battery Charging System," *US Patent*, **5166595**.

[95] CAMPAGNUOLO, C., L. P. JARVIS, A. PELLEGRINO, J. DICARLO, and W. KEANE (1997) "Lead-acid Battery Desulfator/Rejuvenator," *US Patent*, **5677612**.

[96] INSKEEP, M. (2010) "Multi-purpose Battery Jump Starter and Reconditioner," *US Patent*, **2010/0301800 A1**.

[97] ABD MALEK, N., H. HASINI, A. RAHMAN, and M. NASHARUDDIN MOHD JAAFAR (2010) "An improved solar PV system for Malaysian rural electrification part I: Design and testing of solar PV with tracker and reflectors," in *Research and Development (SCOReD), 2010 IEEE Student Conference on*, pp. 452 –457.

[98] GU, W., G. WANG, and C. WANG (2002) "Modeling the Overcharge Process of VRLA Batteries," *Journal of Power Sources*, **108**, pp. 174–184.

[99] SHI, Y., C. FERONE, C. RAO, and C. RAHN (2012) "Nondestructive Forensic Pathology of Lead-Acid Batteries," in *American Control Conference (ACC), 2012*.

Vita

Ying Shi

Ying Shi was born in Shanghai, China. She received the B.S. degree in mechanical engineering from Shanghai Jiao Tong University (SJTU) in July, 2008. In fall 2007, she attended Purdue University as a visiting student. After graduating from SJTU, Ying Shi started her graduate studies at The Pennsylvania State University in August 2008. She received the M.S, degree in electrical engineering from Penn State in May 2012. Then, in May 2013, she received the M.S. degree in mechanical engineering from Penn State. Currently, she is pursuing the Ph.D. degree in mechanical engineering.

Ying Shi joined the Mechatronics Research lab lead by Dr. Christopher D. Rahn in January 2009. She has been worked on testing and control of lead-acid battery pack for hybrid electrical locomotives. Her current research interests include battery real-time aging prognosis and diagnosis, battery charge trajectory optimization, smart cell balancing based on SOH, and advanced battery system hardware-in-the-loop testbed for control algorithm design and validation. She has co-authored five journal and conference publications. Ying Shi has been a student member of the American Society of Mechanical Engineers (ASME). Also, she has served as a reviewer for the American Control Conferences (ACC).

Ying Shi joined National Renewable Energy Laboratory (NREL) in March, 2013. She currently is a research engineer in the Energy Storage group, working on Li-ion battery life testing and modeling.